Electronic Transport in Metallic and Semimetallic Nanostructures

Alfonso Sanchez-Soares
MSc

Thesis submitted for the degree of Doctor of Philosophy

NATIONAL UNIVERSITY OF IRELAND, CORK

TYNDALL NATIONAL INSTITUTE

January 2017

Supervisor: Prof James C Greer

Contents

List of Figures iii
List of Tables viii
List of publications xi

1 Introduction 1

2 Effect of strain, thickness, and local surface environment on electron transport properties of oxygen-terminated copper thin films 15
2.1 Abstract 15
2.2 Introduction 16
2.3 Method 17
2.3.1 Thin film structures 17
2.3.2 Computational details 19
2.4 Results and Discussion 22
2.4.1 DFT vs. DFTB: charge transport properties 22
2.4.2 Transmission pathways 24
2.4.3 Surface scattering model 27
2.5 Conclusions 31
2.6 Acknowledgments 32

3 Electron transport properties of sub-3-nm diameter copper nanowires 38
3.1 Abstract 38
3.2 Introduction 39
3.3 Method 40
3.4 Results and Discussion 45
3.4.1 Nanowire structures 45
3.4.2 Electron transmission 47
3.4.3 Local transmission paths 49
3.4.4 Transmission model 54
3.5 Conclusion 58
3.6 Acknowledgments 59

4 Electronic structure tuning via surface modification in semimetallic nanowires 63
4.1 Abstract 63
4.2 Introduction 64
4.3 Method 65
4.4 Results and Discussion 68
4.4.1 Nanowire structure 68
4.4.2 Electronic structure 70
4.4.3 Charge and potential 76
4.5 Conclusion 80
4.6 Acknowledgments 81

5 A semimetal nanowire rectifier: balancing quantum confinement and surface electronegativity **87**
5.1 Abstract 87
5.2 Acknowledgements 101

6 Conclusions **105**

A Bulk properties of studied materials **112**
A.1 Copper 112
A.2 Tin (α) 114

B Electronic structure and electronic transport methods: a brief overview **119**
B.1 Electronic structure methods 119
B.1.1 Density functional theory 119
B.1.2 Quasiparticles and the GW approximation 123
B.1.3 Density functional tight binding 126
B.2 Electronic transport methods: the non-equilibrium Green's function formalism 130
B.2.1 Transmission pathways 133

C Hollow optimization procedure **142**

List of Figures

1.1 Schematic structure of a CMOS integrated circuit commercialised in the early 2000s. The process starts with a silicon wafer (bottom) and ends with the packaging layers at the top. Adapted from [8]. 3
1.2 Various field-effect transitor designs: (a) single gate transistor, (b) double gate planar transistor, (c) double gate non-planar FinFET, (d) tri-gate FET, (e) quadruple-gate (or gate-all-around FET), and (f) gate-all-around nanowire FET. Reproduced from [24]. 6

2.1 Side and top view of optimized O-terminated Cu thin films. (a) Cu(100)-$(2\sqrt{2} \times \sqrt{2})R45^{\circ}$-O, and (b) Cu(110)-$p(2 \times 1)$-O. Copper atoms away from surfaces are shown in silver, while copper and oxygen atoms at the surface are shown in orange and red, respectively. 19
2.2 DFT-computed transmission for film thickness of 2.0, 2.7, 3.4, 4.5 and 5.6 nm with varying values of the lattice parameter c for inequivalent transport directions (a) A and (b) B as indicated in Fig. 2.1(a). Zero of energy is taken to be at the Fermi level. . . 23
2.3 DFT calculated ratios between the transmission per unit area of structures shown in Fig. 2.1(a) and bulk Cu. The lengths labeling each curve in the legend indicate the lattice constant (biaxial strain). 25
2.4 Histograms showing the error in transmission coefficients obtained using DFTB with respect to DFT transmission at E_F obtained with (a) matsci, and (b) custom parameter sets. Values for structure set shown in Fig. 2.1(a) with varying thickness and strain have been compared. 26
2.5 Evolution of calculated transmission per unit area with film thickness for both structure sets shown in Fig. 2.1 along the [100] and [110] transport directions. DFTB with the custom parameter set has been employed. 27
2.6 Transmission per unit area at the Fermi level as a function of distance from the thin film's surface oxide. Transmission is strongly suppressed near films' surfaces, below the surface transmission per unit area initially increases rapidly and plateaus for depths greater than ≈0.35-0.5 nm, dependent on surface environment. 28

2.7 Projections of transmission pathways at the Fermi level at a plane perpendicular to the transport direction and located halfway between atomic planes. Both the size of the bubbles and their color represent the magnitude of each pathway. Cu atoms are represented by + signs, while O atoms at the surface are shown as **x**. Transport along direction A of the structure shown on Fig. 2.1(a) is shown on the left; while the plot on the right corresponds to transport along [110] in the structure shown in Fig. 2.1(b). . . 29

3.1 Structures of the geometry optimized 1 nm NWs. (a), (b) and (c) show the unterminated [100], [110] and [111] NWs, (d), (e) and (f) show the respective O-terminated NWs. Cu is shown in orange and O in red. 41
3.2 Structures of the geometry optimized O-terminated 3 nm NWs. (a), (b) and (c) show the [100], [110] and [111] NWs, respectively. Cu is shown in orange and O in red. 42
3.3 Transmission for (a) 1 nm and (b) 3 nm Cu NWs. Unterminated NWs (dashed lines) have a larger transmission than oxidized NWs (full lines) irrespective of diameter or crystal orientation. Transmission is strongly influenced by crystal orientation, with [110] NWs exhibiting larger transmission than [100] and [111] NWs. The zero of energy is taken to be at the Fermi level. . . . 48
3.4 Transmission pathways at the Fermi energy for unterminated 1 nm [111] Cu NW. The arrows show the direction of transmission paths. The arrow thickness represents the magnitude of the transmission while the color represents the orientation of the path with respect to the NW axis. Forward transmission is shown in blue, radial transmission in green, and backscattering in red. Pathways with transmission below 10% of the maximum value are omitted for clarity. The dashed black lines mark the positions of the planes shown Fig. 3.5(e). 50
3.5 Cross-section view of the transmission pathways at the Fermi energy. (a) Unterminated [100], (b) O-terminated [100], (c) Unterminated [110], (d) O-terminated [110], (e) Unterminated [111] and (f) O-terminated [111]. Atomic positions are shown as "+" (Cu) or "x" (O). The 'dot' size represents the absolute magnitude of the transmission pathway crossing the plane, while the 'dot' color indicates the magnitude and direction of the transmission pathway. Blue 'dots' correspond to forward transmission and red 'dots' to backscattering. Note the difference in the color scales ranges. 51
3.6 Average local density of states for an atom at the surface (dashed) and at the center (solid) of unterminated 1 nm NWs. The zero of energy is taken to be at the Fermi level. 53

3.7 Schematic representing the copper NW model, with surface, sub surface and bulk regions indicated. R is the radius of the NW, r is the radius of the bulk region, d is the width of the subsurface region, i.e., the depth to which τ is affected by the surface, and δ is the width of the surface. 55
3.8 Schematic representing the evolution of transmission per unit area with increasing nanowire diameter for the case of unterminated (dashed, blue) and oxidized (green, solid) copper NWs. *Cases* discussed in the text corresponding to different size regimes are indicated along the curves. 58

4.1 Atomistic illustrations of α-SnNW cross-sectional and side views of optimized NW structures of 1.5 nm (top row) and 3 nm (bottom row) diameters. (a),(b) $[100]$ $\mathrm{SnCH_3}$, (c),(d) $[110]$ SnOH, and (e),(f) $[111]$ SnF. Sn is shown in purple, H in pink, O in red, C in brown, and F in blue. 66
4.2 Electron affinity and band gap values for 1.5 nm and 3 nm α-Sn NWs passivated and oriented along (a),(b) $[100]$, (c),(d) $[110]$, and (e),(f) $[111]$ crystallographic orientations. All reported energies are in eV. Zero of energy is set to the vacuum level. 71
4.3 Band structures of 1.5 nm and 3 nm α-Sn NWs oriented along different orientations and passivated with varying chemical species. (a),(b) $[110]$ SnH, (c),(d) $[100]$ SnOH, and (e),(f) $[111]$ SnF. Zero of energy is set to the Fermi level. 72
4.4 Band structures of 1.5 nm $[110]$ α-Sn NWs passivated with varying chemical species and three-dimensionsl (3D) charge densities associated with valence band maxima (bottom) and conduction band minima (top). All charge densities taken at the same isosurface level. Zero of energy is set to the Fermi level. . 73
4.5 Band structures of semiconducting 1.5 nm $[110]$ α-Sn NWs in which a passivating group has been removed from the surface (bands shown in black). Bands corresponding to completely passivated structures are shown in red for reference. At the bottom of the figure, atomistic illustrations of the NW structures in which the position of the undercoordinated Sn surface atom is indicated with a red circle are shown along with the charge densities associated with the bands crossing the Fermi level. All charge densities taken at the same isosurface level. Zero of energy is set to the Fermi level. 74
4.6 Hartree difference potential profile across (a) 1.5 nm and (b) 3 nm NW cross sections. The depth of the induced well-like profile is found to increase with passivant electronegativity. Zero of energy has been fixed to potential values in regions far from the structures. 77

4.7 Electron difference density averaged along NW axis for 1.5 nm and 3 nm structures oriented along $[110]$ and passivated with (a)-(b) methyl groups, (c)-(d) hydrogen atoms, (e)-(f) hydroxyl groups, and (g)-(h) fluorine atoms. 78

5.1 Evolution of band gap energies in $[110]$ α-Sn nanowires with diameter from simulations based on DFT with (a) standard GGA functionals and (b) corrected using a scheme involving meta-GGA functionals and many-body perturbation theory. The crossing of each curve with the horizontal dashed line indicates the minimum diameter at which semimetallic behavior is expected. Vertical dashed lines indicate diameters at which band offsets between hydrogen- and fluorine-terminated structures (GGA) and hydrogen- and hydroxyl-terminated structures (corrected) match. 90

5.2 Computed work function (Φ_m), electron affinity (χ_s), and band gap (ε_G) for 1.5 nm diameter $[110]$ α-Sn NWs passivated with fluorine and hydrogen within DFT-GGA. The larger electronegativity of fluorine is found to counteract the quantum-confinement induced bandgap observed for hydrogen terminated NWs. . . . 92

5.3 A semimetal-semiconductor junction is realized by abruptly switching surface terminations from fluorine (left) to hydrogen (right) along the length of a $[110]$ α-Sn NW of 1.5 nm diameter. The plot shows the calculated local density of states (LDoS) across the junction, in which the work function of the semimetallic region (Φ_m) and electron affinity of the semiconducting region (χ_s) are indicated as predicted by DFT-GGA. 94

5.4 Local density of states (LDoS) and energy-resolved current for (a) Forward bias of +0.75 V. Note the quantization of states in the conduction band as a result of a triangular potential well-like profile near the junction; and (b) Reverse bias of -0.75 V. Red segments on each side of the LDoS plots indicate the quasi-Fermi level alignments in the semimetallic and semiconducting electrodes, ε_F^L and ε_F^R, respectively. Note the differences in vertical scales, particularly between the energy-resolved currents in (a) and (b). 97

5.5 (a) Current-voltage characteristics of the junction at a temperature of 300K, (b) Difference between current-voltage characteristics at 300K and 0, and (c) semi-log plot of current density under forward bias (green) and reverse bias (red). 99

A.1 Atomistic Illustrations of the crystal structure of fcc copper: (a) a conventional unit cell and (b) views from the $[100]$, $[110]$, and $[111]$ crystallographic directions of its corresponding primitive cell. 113

A.2 (a) Electronic band structure and (b) Fermi surface of crystalline copper. The Fermi surface is represented inside the Brillouin zone, and the red dots indicate high symmetry points along which the electronic band structure is plotted. The zero of energy in (a) has been taken to be the Fermi level $\mathrm{E_F}$. Fermi surface illustration reproduced from [3]. 114
A.3 Atomistic Illustrations of the crystal structure of α-tin: (a) a conventional unit cell and (b) views from the $[100]$, $[110]$, and $[111]$ crystallographic directions of its corresponding primitive cell. . 115
A.4 (a) Electronic band structure and (b) first Brillouin zone of crystalline α-tin. The high-symmetry points along which the band structure is plotted are indicated in the Brillouin zone. The zero of energy in (a) has been taken to be the Fermi level $\mathrm{E_F}$. 116

C.1 Hollow optimization scheme for the [110]-O NW. The center of the NW (core) is removed and the blue colored atoms are frozen to their bulk position. The geometry of the surface is optimized and the core is added back in to obtain a surface-optimized structure which may be used in subsequent calculations to compute properties such as electron transmission. 142
C.2 (a) and (b) show the similarity in the band structures for the hollow optimized and fully optimized oxidized [110] NWs, respectively. In (c) the hollow optimized structure (pink and red atoms) is superimposed on the fully optimized structure (green atoms). There is a remarkable similarity in the surfaces of the NWs. 143
C.3 The total DOS for the fully optimized and hollow optimized [110] oxidized NW are shown in (a). The changes in LDOS from the surface (Surface) to the center (Surface-6) of the fully optimized (full line) and hollow optimized (dashed line) are given in (b). The DOS and LDOs are comparable for our purposes between the two structures. 144
C.4 The transmission coefficients computed with DFTB for the hollow optimized and fully optimized oxidized [110] NWs close to the Fermi energy (0 eV) deviate by less than typical differences between DFT and DFTB values. 145

List of Tables

2.1 DFT calculated transmission per unit area at E_F for structures shown in Fig. 2.1(a) with varying thickness and biaxial tensile strain. 24
2.2 Computed values for local transmission per unit area with respect to bulk Cu for both structure sets using the custom DFTB parameter set. Values have been obtained by performing a linear fit of obtained data to Eq. 2.5; correlation coefficients greater than 0.99 were obtained in all cases. Values shown in parenthesis have been obtained with DFT. 29

3.1 Optimized cell parameter in Å along the NWs' periodic direction. Unterminated NWs have cell parameter comparable to the calculated bulk value, while terminated NWs have a longer cell parameter. 46
3.2 Calculated transmission per unit area for unterminated and oxidized 1 nm and 3 nm NWs. The area of each NW is the area of a circle, ellipse, or octagon with dimensions equal to the sum of the maximum cross-sectional inter-nuclear distances and twice the Cu atomic radius. 47

4.1 Optimized cell parameter in Å along each NW's periodic direction, and characteristic cross sectional dimensions of Sn cores ϕ_{Sn} in nm. ϕ_{Sn} represent the diameters of perfectly cylindrical structures with areas matching that of each NW structure. Bulk column indicates cell parameter along corresponding crystallographic directions in bulk α-Sn. 68
4.2 Band gap values for 1.5 nm α-Sn NW structures as computed with DFT using pseudo-atomic orbitals (PAOs), plane waves (PWs), and PW calculations including first-order perturbative GW quasi-particle corrections. 75

I, Alfonso Sanchez-Soares, certify that this thesis is my own work and has not been submitted for another degree at University College Cork or elsewhere.

_____

Alfonso Sanchez-Soares

To my family

List of publications

Peer-reviewed journal articles

- **S. L. T. Jones, A. Sanchez-Soares, J.J. Plombon, A.P. Kaushik, R.E. Nagle, J.S. Clarke, and J.C. Greer**
  Electron transport properties of sub-3-nm diameter copper nanowires
  Phys. Rev. B 92, 115413 (2015)
- **A. Sanchez-Soares, S. L. T. Jones, J.J. Plombon, A.P. Kaushik, R.E. Nagle, J.S. Clarke, and J.C. Greer**
  Effect of strain, thickness, and local surface environment on electron transport properties of oxygen-terminated copper thin films
  Phys. Rev. B 94, 155404 (2016)
- **A. Sanchez-Soares, C. O'Donnell, and J.C. Greer**
  Electronic structure tuning via surface modification in semimetallic nanowires
  Phys. Rev. B 94, 235442 (2016)
- **A. Sanchez-Soares and J.C. Greer**
  A semimetal nanowire rectifier: balancing quantum confinement and surface electronegativity
  Nano Lett. 16 (12):7639-7644 (2016)

Patent

- **A. Sanchez-Soares and J.C. Greer**
  Rectifying junction
  UK Patent 1605814.1
  PCT Patent Application No. PCT/EP2016/071408

Conference oral presentations

- **A. Sanchez-Soares and J.C. Greer**
  Bandgap engineering in ultra-thin Sn nanowires
  Intel Ireland Research Conference 2014, 18th November 2014, Dublin, Ireland

- **A. Sanchez-Soares, S. L. T. Jones, and J.C. Greer**
  Electron transport in copper thin films
  Intel Ireland Research Conference 2015, 20th October 2015, Dublin, Ireland

- **A. Sanchez-Soares and J.C. Greer**
  Surface chemical modification of semimetal nanowires for schottky barrier diodes
  2016 NVM Psi-k Workshop: New Horizons for Memory Storage: Advancing Non-volatile Memory with Atomistic Simulations, June 29th - July 1st 2016, Dublin, Ireland

Conference posters

- **A. Sanchez-Soares, S. L. T. Jones, and J.C. Greer**
  Electronic structure of ultra-thin copper nanowires
  Intel Ireland Research Conference 2013, 21st - 22nd November 2013, Dublin, Ireland

- **S. L. T. Jones, A. Sanchez-Soares, and J.C. Greer**
  Electron transport properties of sub-5-nm copper nanowires
  Intel Ireland Research Conference 2014, 18th November 2014, Dublin, Ireland

- **A. Sanchez-Soares and J.C. Greer**
  Bandgap engineering in ultra-thin Sn nanowires
  Materials Research Society Spring Meeting 2015, 6th - 10th April 2015, San Francisco, CA, USA

- **A. Sanchez-Soares and J.C. Greer**
  Electronic structure modification of ultra-thin Sn nanowires through surface chemistry
  58th Electronics Materials Conference, 22nd - 24th June 2016, Newark, DE, USA

- **A. Sanchez-Soares, S. L. T. Jones, and J.C. Greer**
  Effect of strain, thickness, and local surface environment on electron transport properties of oxygen terminated copper thin films
  2016 NVM Psi-k Workshop: New Horizons for Memory Storage: Advancing Non-volatile Memory with Atomistic Simulations, June 29th - July 1st 2016, Dublin, Ireland

Chapter 1

Introduction

Advances made in the field of electronics during the last century have revolutionized most aspects of life in the industrialised world. Over the years, integrated circuits (ICs) have come to play an increasingly important role in global economy up to the point where most financial, communications, and healthcare services depend heavily on them. ICs have been made possible by using semiconductor devices to perform logic operations through the implementation of digital circuits employing logic gates designed with transistors as their key active components. Since its first realization nearly 70 years ago, the transistor is on the list of IEEE milestones in electronics and has been the key to harnessing computing and amplifying power from electric current [1].

The realization of mathematical operations through digital circuits is made possible by transistors, which serve as switches allowing the implementation of Boolean logic gates and can be arranged to perform basic mathematical operations. Modern ICs incorporate up to billions of transistors in designs that allow vast quantities of mathematical operations to be performed in less than a second. This unprecedented computing power has penetrated nearly all aspects of human life making fundamental research in this field of critical importance. Currently there are a minimum estimated of 15 billion interconnected electronic devices in the world, a number that is only expected to increase in the coming years as more and more aspects of our lives are intertwined with the world of electronic communications and the Internet [2].

Projected scaling of the amount of active electronic devices in the world requires a dramatic increase in power efficiency in order to cater to the needs of a society increasingly dependant on electronic devices/technologies. Research in

the field throughout the 20th century aimed primarily at increasing the computing power of integrated circuits by increasing the amount of transistors packed in a single chip. Since the early days of vacuum tubes being used for performing switching operations, the removal of fundamental circuit size limitations with the discovery that semiconductor devices could perform similar functions comprised a major breakthrough in this direction earning William Bradford Shockley, John Bardeen and Walter Brattain the Nobel Prize in Physics in 1956 for first implementing it [3]. The possibility of miniaturising the basic active circuit component -the transistor- set the track for large scale integration enabling packing of thousands -and eventually billions- of them into small areas. As of 2016, commercially available microprocessors include up to 25 million transistors per mm^2 [4].

This remarkable decrease in transistor sizes and the concomitant increase in computing power have been made possible by over half a century of continuous research in the field. The size of transistors in commercially available microprocessors has been steadily decreasing from $\approx 10\ \mu\mathrm{m}$ in the 1970s up to the present ≈ 14 nm technology [4]. The approximately steady rate at which electronic components in a chip have decreased in size over the past decades was predicted in a famous paper by Gordon Moore in 1965 in what became widely known within electronics as *Moore's law* [5]. In that paper, Moore predicted the then relatively new field of integrated circuits to penetrate all aspects of life eventually becoming an omnipresent reality in *the future*. By observation of developments in the field and employing engineering and economic arguments, he predicted that the number of components in an integrated circuit would double every year for the following 10 years. In 1975, he analysed the state of the field and predicted the rate of increase in the amount of components per chip to reduce by half [6]. With the basic design of transistors used in integrated electronics remaining approximately constant over the coming decades, the revised *Moore's law* predicting a doubling of components per chip every two years morphed into a driving force for the semiconductor industry –rather than an observation– which held up until around 2012. In 2015, in an interview commemorating 50 years since the original paper was published, Gordon Moore stated his law is likely to come to an end in the next decade as fundamental physical limits to continuing *scaling as usual* are reached [7].

Figure 1.1 illustrates the basic structure of a planar CMOS IC design as commercialised around 2005. Starting from the bottom, the first portion is known as the *front-end-of-the-line* (FEOL) and is where active devices are patterned; the

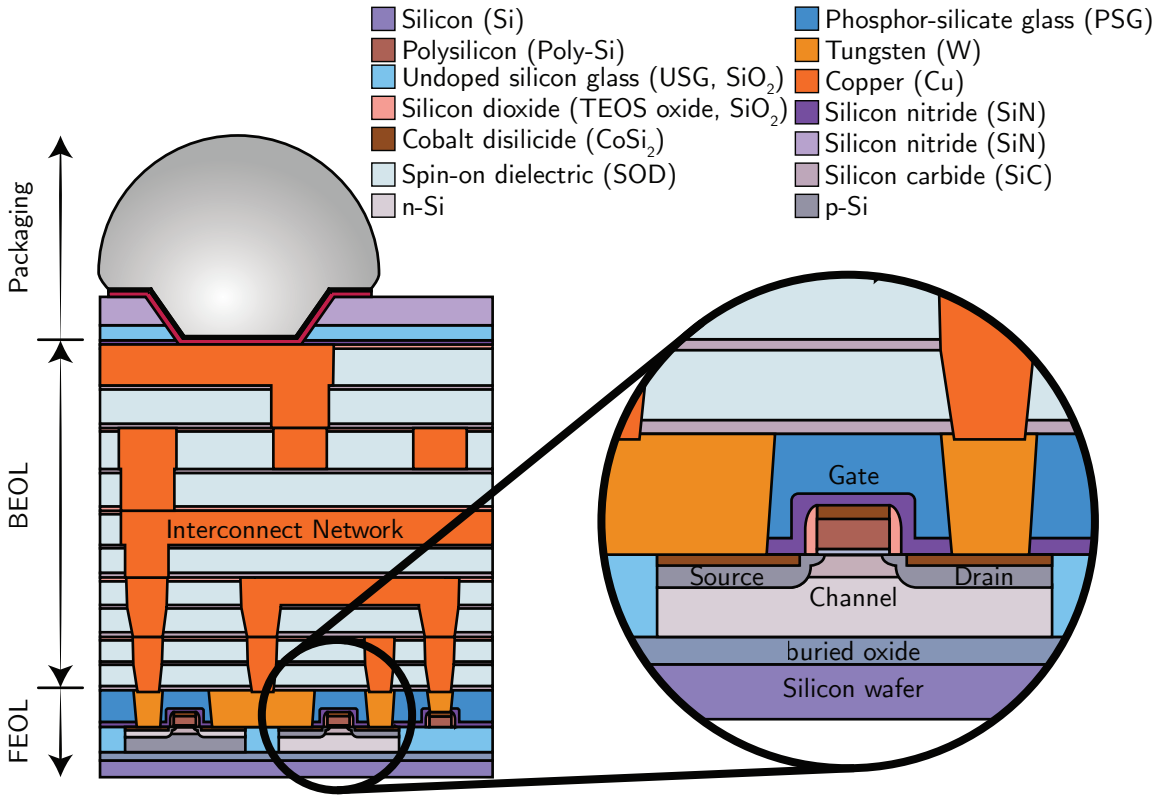

Figure 1.1: Schematic structure of a CMOS integrated circuit commercialised in the early 2000s. The process starts with a silicon wafer (bottom) and ends with the packaging layers at the top. Adapted from [8].

second portion is known as the *back-end-of-the-line* (BEOL) and consists mainly of an interconnect network which provides necessary electrical connections between FEOL components. Finally, the *packaging* portion at the top encapsulates the IC and provides protection against physical damage and corrosion. Mathematical operations are performed at the FEOL by vast numbers of logic gates consisting of nanoscale transistors in which current flow between the source and drain through the channel region is controlled by applying a potential to the gate electrode. Given that the basic architecture of planar field-effect transistors (FETs) illustrated on the right hand side of fig. 1.1 and employed in CMOS technology commercialised by the semiconductor industry has not changed dramatically in decades, the downscaling of such components has mainly consisted of miniaturisation of essentially the same design. This effort in downscaling standard CMOS design to continue Moore's law is known as *More Moore* [9].

In an effort to flank limitations associated with extending CMOS scaling, several strategies have been implemented within the last decade to improve de-

vice performance through the use of different or strained materials and slightly modified device structures. However, the reduction of transistor sizes down to merely thousands of atoms means the atomistic nature of materials can no longer be ignored. Issues intrinsically related to the size of these systems such as high variabilities arising from the use of dopants, or difficulties springing from the integration of heterogeneous systems (e.g. Fermi level pinning) call for fundamental changes in the design of logic switches. This set of technologies employing fundamentally different designs –which are expected to scale differently– are collectively known as *beyond CMOS* technologies [9].

World-class experts in semiconductor technology have been publishing a set of documents known as the International Roadmap for Semiconductors (ITRS) roughly every two years for the past couple of decades in which the state of all aspects of semiconductor technology is assessed, challenges associated with continuing scaling identified, and strategies on ways to overcome them are proposed [9]. In particular, its *Emerging Research Devices* (ERD) [10] section analyses the state, integrability and challenges of emerging *beyond CMOS* technologies for applications in memory and logic devices. Among the numerous challenges involved in continuing to scale ICs beyond CMOS, in this work we shall focus on two key aspects: new device concepts for memory and logic applications, and the scaling of interconnect networks.

An unavoidable consequence of continuing miniaturisation of active circuits elements is a reduction in the cross section of the interconnect lines that link them together. The ITRS' *Interconnects* section defines the function of an interconnect or wiring system as "to distribute clock and other signals and to provide power/ground, to and among, the various circuit/system functions on a chip" [11]. Scaling of active elements must be accompanied by a concomitant reduction in size of the interconnect network. A significant increase in the resistivity of interconnect networks is observed as the characteristic cross-sectional dimensions of lines approach the intrinsic electron mean free path in the metal and hence the probability of electron scattering against a line's sidewalls as it travels through the network increases [12]. Copper (mean free path ≈ 40 nm at room temperature) has been the interconnect metal of choice of the semiconductor industry for almost two decades. As interconnect line dimensions have reduced in recent years, a significant increase in resistivity has been observed with the ITRS employing size-dependent values for Cu resistivity in their reports and projections since 2004. With next-generation interconnects' characteristic dimensions approaching 10 nm, mitigation of size-effects in order to maintain

acceptable resistivity values is listed as one of the five most critical challenges for future technologies as device performance is increasingly affected by larger voltage drops across interconnect lines, as well as the RC delay they contribute to the circuit, which is already becoming a performance bottleneck and is expected to increase by an order of magnitude in five years [9].

Electronic transport in metallic structures has been extensively studied over the past decades with theoretical models for most sources of electron scattering (*i.e.*, sources of electrical resistance) proposed and their dependence on structural details assessed [13–21]. Unfortunately, most of the available theory assumes continuum models and fails to account for the unavoidably atomistic structure of nanoscale materials. Additionally, interpretation of experimental results is complicated due to difficulties in experimental control over structural properties of studied samples as they can be sensitive to processing conditions and sample dimensions [see sections 2.2 and 3.2]. This, combined with fundamental difficulties in decoupling contributions arising from various scattering mechanisms, makes experimental characterisation of the impact and scaling of different scattering sources a challenge, making insight obtained from computational simulations of great value in optimising the conductivity of sub-10-nm interconnect lines.

For logic and memory applications, a number of emerging technologies are being broadly investigated as alternatives to silicon-based CMOS with varying degrees of integrability with present technologies: from other charge-based concepts such as carbon-based electronics or tunnel FETs, to devices using different state-variables such as spin-logic devices or resistive RAM. In this search for the successor of silicon technology there is no definite answer yet, as different proposals address different issues and bring difficulties of their own into the picture. In a survey conducted at the Emerging Logic Device Assessment Workshop in 2014, nanowire-based transistors were voted one of the most promising candidates for substituting present transistor designs [10, 22].

One of the key issues with scaling down transistor which nanowire FETs designs address is the performance and efficiency reductions associated with the so called short-channel-effects (SCEs). Reducing channel lengths (*i.e.,* distance between source and drain) translates in an increasing dependence of the electric field in the channel with the source-drain bias, reducing electrostatic control coming from the gate electrode and ultimately hindering device performance [23]. A way of mitigating these effects is to increase the gate control

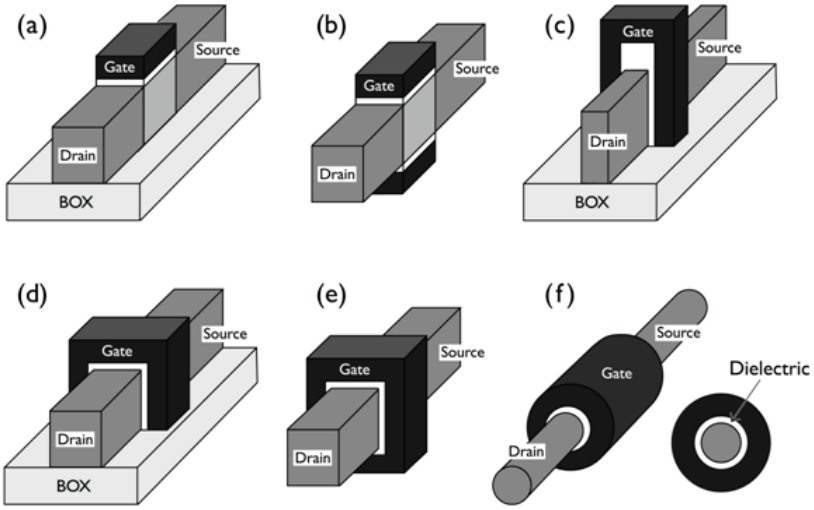

Figure 1.2: Various field-effect transitor designs: (a) single gate transistor, (b) double gate planar transistor, (c) double gate non-planar FinFET, (d) tri-gate FET, (e) quadruple-gate (or gate-all-around FET), and (f) gate-all-around nanowire FET. Reproduced from [24].

over the channel by increasing the area around the channel in *contact* with the gate. Figure 1.2 shows transistor designs with increasing electrostatic control over the channel achieved by increasingly wrapping the gate around the channel. From the simpler top-gate design shown in fig. 1.2(a) to tri-gate designs currently being commercialised (fig. 1.2(d)), gate-all-around gate designs in nanowire structures provide the greatest electrostatic control of the channel and hence enable smaller designs with greater power efficiency [25].

Nanowire field-effect transistors (NW FETs) offer a promising alternative to traditional planar devices as their quasi-1D structure has been shown to exhibit superior performance at sizes required by upcoming technology nodes: Effective electrostatic control of quasi-1D channels with efficient gate structures such as gate-all-around (GAA) have been shown to improve tolerance to short channel effects and thus allow for device designs with shorter channel lengths, the possibility of 3D integration allows higher packing densities, and the potential to explore alternative device concepts not available with planar technology [26, 27]. Ultra-thin NW FETs with diameters down to below 5 nm have already been demonstrated [28], with recent studies successfully realizing 3D integration [29–32] and showing superior electrostatic control of the channel with novel gate structures, resulting in improved device performance when compared to planar and tri-gate technologies currently in production [27, 33, 34].

At the same time considerable effort is being put into investigating the difficulties associated with fabricating NW devices such as reliability concerns due to heat dissipation, particularly in 3D-integrated structures [35, 36]; or reducing structural defect densities in fabricated NW structures [37]. However, the broad range of properties that can be obtained from NW devices through the design of interfaces, and with remarkable tunability achieved through the use of chemical and structural modifications has so far allowed elucidation of numerous applications of such as sensors [38, 39], transparent electronics [40], and tunnel FETs [41, 42]; making them one of the most promising candidates for near-future technologies.

In particular, a recent study theoretically demonstrated the possibility of exploiting size effects to realise a dopant-free Schottky-barrier FET (NW-SB-FET) by varying the cross section along the length of a single-crystalline semimetallic NW [43]. The large surface-to-volume ratio of nanostructures allows novel properties to be obtainable from well-known materials which can be exploited for designing metal-semiconductor interfaces within a single material. Analogous to observed blue shifts in electronic band gaps observed for porous silicon and other semiconductor nanostructures, quantum confinement effects are capable of modifying the properties of bulk semimetals so that they transition to semiconducting behaviour and exhibit a band gap when nanopatterned, thus allowing the design of Schottky barriers in nanowires made of semimetals by modulating NW diameter along their length and hence creating an interface between regions with thicker (semimetallic) and thinner (semiconducting) cross-sections above and below a threshold dimension, respectively. Arranging Schottky barriers allows for the design of electronic components such as diodes and transistors, and all higher-level devices which can be built from combining these. The use of designs in which there are no interfaces between different materials has the advantage of potentially cleaner interfaces; while avoiding the use of dopants mitigates variability issues and could ease manufacturing constraints.

The following chapters consist on a collection of peer-reviewed articles in which we employ state-of-the-art *ab-initio* atomistic computational methods to explore the electronic structure and electron transport properties of metallic and semimetallic nanostructures in order to assess their suitability for next-generation *beyond CMOS* devices as interconnects and in the design of NW field-effect-transistors, respectively [44–47]. For interconnect networks we shall focus the present study on Cu nanostructures as it has been the semiconductor in-

dustry's metal of choice for the past couple of decades; whilst our study on nanoscale semimetals will be based on α-Sn nanostructures, which we use as an exemplar due to its simple structural and chemical properties. The bulk properties of these two materials are briefly presented in appendix A. We compute electronic structure properties by explicitly treating the fully atomistic structure of nanowires and thin films through simulations based on *ab-initio* density functional theory [48, 49] (DFT) and semiempirical density functional tight binding [50, 51] (DFTB) methods; the system's electronic transport properties are then calculated by combining the computed electronic structure with non-equilibrium Green's functions (NEGF) methods within the Landauer formalism for coherent elastic scattering [52–54]. A brief overview of the electronic structure and electronic transport methods employed throughout this thesis is given in appendix B.

In chapters 2 and 3 we study the impact of surface and size effects on the structural, electronic, and electrical properties of copper nanowires and thin films and identify the most relevant parameters for maximising the conductivity of copper nanostructures with characteristic dimensions below 10 nm. Given the computational effort required for *ab-initio* density functional theory simulations of structures with characteristic dimensions above 3 nm, we assess the accuracy of semi-empirical density functional tight binding (DFTB) methods in chapter 2 as the associated reduction in computational effort with DFTB enables exploration of larger atomistic structures up to dimensions closer to sizes currently being experimentally investigated.

In chapters 4 and 5, we build on previously published results for nanostructured semimetals. We explore the range of material properties which can be obtained from semimetal nanowires in chapter 4 by introducing surface chemistry variations and studying their impact on electronic properties, and how they can be exploited for the design of next-generation logic switches. Given the large impact of surface phenomena on the properties of nanostructures, we take a particular interest in the dependence of reported size-induced semimetal-to-semiconductor transition with varying surface passivants. As a class of materials with potential applications in nanoelectronics, prediction of achievable band gap magnitudes in confined semimetals is of key importance. To this end, we improve upon our DFT description of the electronic structure by means of first order many-body perturbation theory; we correct calculated band gap magnitudes by computing self-energy corrections within the GW approximation, which predicts band gaps much closer to experimental results than DFT with standard

exchange-correlation functionals.

Finally, we propose a novel way of forming semimetal-semiconductor Schottky-like junctions in nanostructures based on semimetals *without* the need to vary cross sectional dimensions along the length of the device; the electrical properties of a novel diode design which exploits surface chemistry effects for the formation of a semimetal-semiconductor rectifying junction are explored in chapter 5. This method can be employed for the design of interfaces for device applications which in combination with other methods –such as variations in cross-sectional dimensions or variations in alloy composition– allows for highly customisable interface design. Arrays of such interfaces enable a new set of nanoelectronic device designs with potential applications in logic and memory which overcome several of the fundamental challenges and limitations of present technologies.

References

[1] Milestones: Invention of the first transistor at Bell Telephone Laboratories, Inc., 1947. *http://ieeemilestones.ethw.org/ (accessed December 2016)*.

[2] Popular internet of things forecast of 50 billion devices by 2020 is outdated. *http://spectrum.ieee.org/ (accessed December 2016)*.

[3] The Nobel prize in physics 1956. *http://www.nobelprize.org/ (accessed December 2016)*.

[4] Transistor count. *https://en.wikipedia.org/wiki/Transistor_count (accessed December 2016)*.

[5] Gordon Moore. Cramming more components onto integrated circuits. *Electronics*, 8, 1965.

[6] Gordon Moore. Progress in digital integrated electronics. *IEEE Int. Electron Devices Meet.*, pages 11–13, 1975.

[7] Gordon Moore. Gordon Moore: The man whose name means progress. The visionary engineer reflects on 50 years of Moore's law. *IEEE Spectrum: Special Report: 50 Years of Moore's Law (Interview)*, 2015.

[8] Schematic structure of a CMOS chip as commercialised in the early 2000s. *https://commons.wikimedia.org/ (accessed December 2016)*.

[9] International technology roadmap for semiconductors. *http://www.itrs2.net/itrs-reports.html (accessed August 2016)*.

[10] ITRS reports 2015 edition: Emerging research devices. *http://www.itrs2.net/itrs-reports.html (Accessed December 2016)*.

[11] ITRS reports 2013 edition: Interconnects. *http://www.itrs2.net/itrs-reports.html (Accessed December 2016)*.

[12] Daniel Josell, Sywert H. Brongersma, and Zsolt Tokei. Size-dependent resistivity in nanoscale interconnects. *Annu. Rev. Mater. Res.*, 39:231–254, 2009.

[13] Thomson JJ. On the theory of electric conduction through thin metallic films. *Proc. Camb. Philos. Soc.*, 11:120, 1901.

[14] A. C. B. Lovell. The electrical conductivity of thin metallic films. I. rubidium on Pyrex glass surfaces. *Proc. R. Soc. A*, 157(891):311–330, 1936.

[15] K. Fuchs. The conductivity of thin metallic films according to the electron theory of metals. *Math. Proc. Cambridge Philos. Soc.*, 34:100–108, 1938.

[16] E. H. Sondheimer. Influence of a magnetic field on the conductivity of thin metallic films. *Nature*, 164(4178):920–921, 1949.

[17] R. G. Chambers. The conductivity of thin wires in a magnetic field. *Proc. R. Soc. A*, 202(1070):378–394, 1950.

[18] R. B. Dingle. The electrical conductivity of thin wires. *Proc. R. Soc. A*, 201(1067):545–560, 1950.

[19] E.H. Sondheimer. The mean free path of electrons in metals. *Adv. Phys.*, 1(1):1–42, 1952.

[20] A. F. Mayadas, M. Shatzkes, and J. F. Janak. Electrical resistivity model for polycrystalline films: The case of specular reflection at external surfaces. *Appl. Phys. Lett.*, 14(11):345–347, 1969.

[21] A. F. Mayadas and M. Shatzkes. Electrical-resistivity model for polycrystalline films: The case of arbitrary reflection at external surfaces. *Phys. Rev. B*, 1:1382–1389, 1970.

[22] ITRS 2015 edition: Beyond CMOS. *http://www.semiconductors.org (Accessed December 2016)*.

[23] Qian Xie, Chia-Jung Lee, Jun Xu, Clement Wann, Jack Y.-C. Sun, and Yuan Taur. Comprehensive analysis of short-channel effects in ultrathin SOI MOSFETs. *IEEE Trans. Electron Devices*, 60(6):1814–1819, 2013.

[24] Yong-Bin Kim. Challenges for nanoscale MOSFETs and emerging nanoelectronics. *Trans. Electr. Electron. Mater.*, 11(3):93–105, 2010.

[25] Jean-Pierre Colinge and James C. Greer. *Nanowire Transistors: Physics of devices and materials in one dimension*. Cambridge University Press, Cambridge CB2 8BS, United Kingdom, 2016.

[26] J. Appenzeller, J. Knoch, M. T. Bjork, H. Riel, H. Schmid, and W. Riess. Toward nanowire electronics. *IEEE Trans. Electron Devices*, 55(11):2827–2845, 2008.

[27] Peng Zheng, D. Connelly, Fei Ding, and Tsu-Jae King Liu. FinFET evolution toward stacked-nanowire FET for CMOS technology scaling. *IEEE Trans. Electron Devices*, 62(12):3945–3950, 2015.

[28] N. Singh, A. Agarwal, L. K. Bera, T. Y. Liow, R. Yang, S. C. Rustagi, C. H. Tung, R. Kumar, G. Q. Lo, N. Balasubramanian, and D. L. Kwong. High-performance fully depleted silicon nanowire (diameter $<$ 5 nm) gate-all-around CMOS devices. *IEEE Electron Device Lett.*, 27(5):383–386, 2006.

[29] T. Bryllert, L. E. Wernersson, L. E. Froberg, and L. Samuelson. Vertical high-mobility wrap-gated InAs nanowire transistor. *IEEE Electron Device Lett.*, 27(5):323–325, 2006.

[30] D. Yakimets, G. Eneman, P. Schuddinck, T. H. Bao, M. G. Bardon, P. Raghavan, A. Veloso, N. Collaert, A. Mercha, D. Verkest, A. V. Y. Thean, and K. De Meyer. Vertical GAAFETs for the ultimate CMOS scaling. *IEEE Trans. Electron Devices*, 62(5):1433–1439, 2015.

[31] Byung-Hyun Lee, Min-Ho Kang, Dae-Chul Ahn, Jun-Young Park, Tewook Bang, Seung-Bae Jeon, Jae Hur, Dongil Lee, and Yang-Kyu Choi. Vertically integrated multiple nanowire field effect transistor. *Nano Lett.*, 15(12):8056–8061, 2015.

[32] C. Thelander, L. E. Froberg, C. Rehnstedt, L. Samuelson, and L. E. Wernersson. Vertical enhancement-mode InAs nanowire field-effect transistor with 50-nm wrap gate. *IEEE Electron Device Lett.*, 29(3):206–208, 2008.

[33] Chenyun Pan, P. Raghavan, D. Yakimets, P. Debacker, F. Catthoor, N. Collaert, Z. Tokei, D. Verkest, A. V. Y. Thean, and A. Naeemi. Technology/system codesign and benchmarking for lateral and vertical GAA nanowire FETs at 5-nm technology node. *IEEE Trans. Electron Devices*, 62(10):3125–3132, 2015.

[34] Christian Schulte-Braucks, Simon Richter, Lars Knoll, Luca Selmi, Qing-Tai Zhao, and Siegfried Mantl. Experimental demonstration of improved ana-

log device performance of nanowire-TFETs. *Solid-State Electron.*, 113:179 – 183, 2015.

[35] S. Shin, M. A. Wahab, M. Masuduzzaman, K. Maize, J. Gu, M. Si, A. Shakouri, P. D. Ye, and M. A. Alam. Direct observation of self-heating in III-V gate-all-around nanowire MOSFETs. *IEEE Trans. Electron Devices*, 62(11):3516–3523, 2015.

[36] A. Laurent, X. Garros, S. Barraud, G. Reimbold, D. Roy, E. Vincent, and G. Ghibaudo. Extensive study of bias temperature instability in nanowire transistors. *Microelectron. Eng.*, 147:10 – 14, 2015.

[37] Marios Constantinou, Vlad Stolojan, Kiron Prabha Rajeev, Steven Hinder, Brett Fisher, Timothy D. Bogart, Brian A. Korgel, and Maxim Shkunov. Interface passivation and trap reduction via a solution-based method for near-zero hysteresis nanowire field-effect transistors. *ACS Appl. Mater. Interfaces*, 7(40):22115–22120, 2015.

[38] L Liao, Z Zhang, B Yan, Z Zheng, Q L Bao, T Wu, C M Li, Z X Shen, J X Zhang, H Gong, J C Li, and T Yu. Multifunctional CuO nanowire devices: p-type field effect transistors and co gas sensors. *Nanotechnology*, 20(8):085203, 2009.

[39] DaeIl Kim, Yong-Kwan Kim, Sung Chan Park, Jeong Sook Ha, Junghwan Huh, Junhong Na, and Gyu-Tae Kim. Photoconductance of aligned $\mathrm{SnO_2}$ nanowire field effect transistors. *Appl. Phys. Lett.*, 95(4), 2009.

[40] Eric N. Dattoli, Qing Wan, Wei Guo, Yanbin Chen, Xiaoqing Pan, and Wei Lu. Fully transparent thin-film transistor devices based on $\mathrm{SnO_2}$ nanowires. *Nano Lett.*, 7(8):2463–2469, 2007.

[41] Q. T. Zhao, S. Richter, C. Schulte-Braucks, L. Knoll, S. Blaeser, G. V. Luong, S. Trellenkamp, A. Schäfer, A. Tiedemann, J. M. Hartmann, K. Bourdelle, and S. Mantl. Strained Si and SiGe nanowire tunnel FETs for logic and analog applications. *IEEE J. Electron Devices Soc.*, 3(3):103–114, 2015.

[42] F. Conzatti, M. G. Pala, D. Esseni, E. Bano, and L. Selmi. Strain-induced performance improvements in InAs nanowire tunnel FETs. *IEEE Trans. Electron Devices*, 59(8):2085–2092, 2012.

[43] Lida Ansari, Giorgos Fagas, Jean-Pierre Colinge, and James C. Greer. A proposed confinement modulated gap nanowire transistor based on a metal (tin). *Nano Lett.*, 12(5):2222–2227, 2012.

[44] Sarah L. T. Jones, Alfonso Sanchez-Soares, John J. Plombon, Ananth P. Kaushik, Roger E. Nagle, James S. Clarke, and James C. Greer. Electron transport properties of sub-3-nm diameter copper nanowires. *Phys. Rev. B*, 92:115413, 2015.

[45] Alfonso Sanchez-Soares, Sarah L. T. Jones, John J. Plombon, Ananth P. Kaushik, Roger E. Nagle, James S. Clarke, and James C. Greer. Effect of strain, thickness, and local surface environment on electron transport properties of oxygen-terminated copper thin films. *Phys. Rev. B*, 94:155404, 2016.

[46] Alfonso Sanchez-Soares, Conor O'Donnell, and James C. Greer. Electronic structure tuning via surface modification in semimetallic nanowires. *Phys. Rev. B*, 94:235442, 2016.

[47] Alfonso Sanchez-Soares and James C. Greer. A semimetal nanowire rectifier: Balancing quantum confinement and surface electronegativity. *Nano Lett.*, 16(12):7639–7644, 2016.

[48] Reiner M. Dreizler and Eberhard K.U. Gross. *Density functional theory: An approach to the quantum many-body problem*. Springer, Berlin, Germany, 1990.

[49] Richard M. Martin. *Electronic structure*. Cambridge University Press, Cambridge CB2 8BS, United Kingdom, 2008.

[50] M. Elstner, D. Porezag, G. Jungnickel, J. Elsner, M. Haugk, Th. Frauenheim, S. Suhai, and G. Seifert. Self-consistent-charge density-functional tight-binding method for simulations of complex materials properties. *Phys. Rev. B*, 58(11):7260–7268, 1998.

[51] Pekka Koskinen and Ville Mäkinen. Density-functional tight-binding for beginners. *Comput. Mater. Sci.*, 47(1):237–253, 2009.

[52] R. Landauer. Spatial variation of currents and fields due to localized scatterers in metallic conduction. *IBM J. Res. Dev.*, 1(3):223–231, 1957.

[53] Supriyo Datta. *Electronic transport in mesoscopic systems*. Cambridge University Press, Cambridge CB2 8BS, United Kingdom, 1995.

[54] Mads Brandbyge, José-Luis Mozos, Pablo Ordejón, Jeremy Taylor, and Kurt Stokbro. Density-functional method for nonequilibrium electron transport. *Phys. Rev. B*, 65:165401, 2002.

Chapter 2

Effect of strain, thickness, and local surface environment on electron transport properties of oxygen-terminated copper thin films

2.1 Abstract

Electron transport is studied in surface oxidized single-crystal copper thin films with a thickness of up to 5.6 nm by applying density functional theory and density functional tight binding methods to determine electron transport properties within the ballistic regime. The variation of the electron transmission as a function of film thickness as well as the different contributions to the overall electron transmission as a function of depth into the the films is examined. Transmission at the oxidized copper film surfaces is found to be universally low. Films with thickness greater than 2.7 nm exhibit a similar behavior in local transmission per unit area with depth from the film surface; transmission per unit area initially increases rapidly and then plateaus at a depth of approximately 0.35-0.5 nm away from the surface, dependent on surface facet. Unstrained films tend to exhibit a higher transmission per unit area than corresponding films under tensile strain.

2.2 Introduction

Understanding the effects of scaling to extreme nanoscale limits of a few nanometers on material properties is required for the design of improved nanoelectronic interconnects and devices. Copper has been chosen as the dominant interconnect material in micro- and nanoelectronics since the decision to replace aluminum for integrated circuit applications that occurred approximately two decades ago. As the size of metallic nanostructures becomes less than the electron mean free path (≈ 40 nm in Cu), significantly more electron collisions with surfaces occur as electrons travel through the sample, which results in a dramatic increase in resistivity. This undesirable increase in line resistance in the nanoscale regime compared to bulk is well established for copper nanostructures [1, 2]. Whether copper can function effectively as an interconnect material in future nanoscale devices remains a subject for debate. The role different structural scattering sources such as defects, surfaces, and grain boundaries [3–5] play in determining the overall resistance for specific geometries needs to be understood in order to minimize the line resistance of copper and other proposed materials for nanoelectronics interconnects.

The conductivity of metal thin films is extremely sensitive to processing conditions. In the case of gold thin films, Henriquez *et al.* [6, 7] report that electron scattering is governed to a large extent by the grain sizes of the film. When the grain size is much smaller than the electron mean free path grain boundary scattering becomes critical to resistivity, conversely surface scattering dominates when the grain size is much larger than the electron mean free path. Grain boundary scattering is reported as the most important contributor to scattering in copper thin films with thickness as low as 27 nm [8, 9]. The surface environment itself is also known to significantly affect the conductivity of copper thin films. Electron scattering at the copper-vacuum surface is partially specular, however variations in the surface environment can induce dramatic changes to the conductivity of copper thin films. Scattering at the thin film surface is reported to become diffuse after deposition of Ta [10, 11] or surface oxidation [12]. *Ab initio* simulations suggest that scattering at a copper-metal interface is intimately related to the electronic properties of the metals [13]. Resistivity decreases compared to a bare copper surface when the density of states (DOS) of the coating or barrier layer matches that of copper surface atoms (Al and Pd). The converse is also the case with increased resistivity observed for coating metals whose DOS doesn't match copper surface atoms (such as for Ta, Ti, and Ru).

However, this resistivity increase on deposition is reported to be reversed by exposure to air, i.e., oxidation of the coating metal for the case of Ta [14]. Zinc coated copper thin films also show reduced surface scattering compared to bare copper surfaces exposed to air [15].

In the following, a theoretical study of electron transport properties in oxidized single-crystal copper thin films using *ab initio* and semiempirical computational techniques is presented. Although copper interconnect lines in integrated circuits are typically surrounded by diffusion barriers a few nanometers thick and composed of materials such as tantalum or tantalum nitride, we focus our study on copper thin films with known planar copper oxide structures on their surfaces. This allows the study of crystalline structures with passivated surfaces whilst minimizing the computational effort employed in simulating regions outside the conductor of interest. We explore the effects of different oxidized surface environments, film thickness, and crystallographic orientation along which electronic transport occurs. Consistent with expectations, the transmission at the film surfaces is found to be strongly modulated by the presence of oxygen, and a linear relationship between cross section and transmission for copper films as thin as 2.7 nm is found.

2.3 Method

2.3.1 Thin film structures

The thin films in this study are based on bulk fcc Cu with two different exposed facets on the surface. The first set of structures have exposed (100) facets at their surfaces in which there is a monolayer of oxidized copper with an oxygen coverage of 0.5 ML, and present a local surface environment with a $(2\sqrt{2} \times \sqrt{2})R45^\circ$ missing row reconstruction [see Fig. 2.1(a)], a structure which has previously been theoretically and experimentally identified [16–22] . The immediate surface of the simulated cell consists of 3 Cu atoms and 2 O atoms; each O atom bonds to 4 Cu atoms, three at the surface and one in the Cu layer below the surface, while each surface Cu atom bonds to 2 O atoms. A two dimensional oxide forms with a missing row of Cu atoms at the surface [as indicated in Fig. 2.1] with the O atoms inserting into Cu-Cu bonds adjacent to the missing row. This structural rearrangement enables the O-Cu-O angle to be close to 180° as occurs in bulk copper oxides such as CuO and Cu_2O.

Films with thicknesses ranging from 1.9 to 5.6 nm are considered; and in addition the effect of tensile strain on conductance is investigated by studying structures generated with an increased lattice parameter c from 3.63 Å –the equilibrium lattice parameter within our approximation– to 3.80 Å and 3.90 Å (biaxial tensile strains of 4.7% and 7.4%, respectively). Interconnect copper structures are expected to present regions with localized strain near interfaces with diffusion barrier layers, which tend to have greater lattice spacings than copper. As dimensions reduce and due to the malleability of metals, the portion of a copper line impacted by strain becomes increasingly important. In the case of ultrathin Cu nanowires, previous work reports a lattice parameter tendency to increase due to the presence of surface oxidation with Cu-Cu spacings increasing as much as 11% [23] [see chapter 3]. We therefore include the case of tensile strained films in order to assess its impact on the conductivity of copper nanostructures.

Transport along [110] and two perpendicular nonequivalent [100] directions are considered for this set of structures: along axes A and B [see Fig. 2.1(a)]. Whilst away from the surface both directions are equivalent to [100] in fcc bulk Cu, the surface environment introduces anisotropy: the missing row of Cu atoms is perpendicular to axis A and parallel to axis B.

In order to further explore the effect of different surface environments, a second set of structures with (110) exposed facets, an oxygen coverage of 0.5 ML, and thicknesses ranging from 2.3 to 5.1 nm is studied. In these structures, the surface environment corresponds to the missing row $p(2 \times 1)$ reconstruction which has been extensively studied [21, 24–27], and has been the focus of recent atomic force microscopy studies due to its chemical fingerprinting properties [28–30]. Similar to the previously discussed surface environment, each surface Cu atom bonds to 2 O atoms, while each O atom bonds to 4 Cu atoms: two at the surface and two in the next Cu layer into the film. In these structures, electron transport properties are studied along nonequivalent perpendicular directions which deep into the film correspond to transport along the [100] and [110] crystallographic directions of bulk Cu, respectively [see Fig. 2.1(b)].

The definition of film thickness is somewhat ambiguous due to the atomistic structure of the films; a convention of choosing the thickness of the slab to be the internuclear separation between atoms in the top and bottom surfaces of the thin film plus twice the atomic radius of Cu (128 pm) is followed [31].

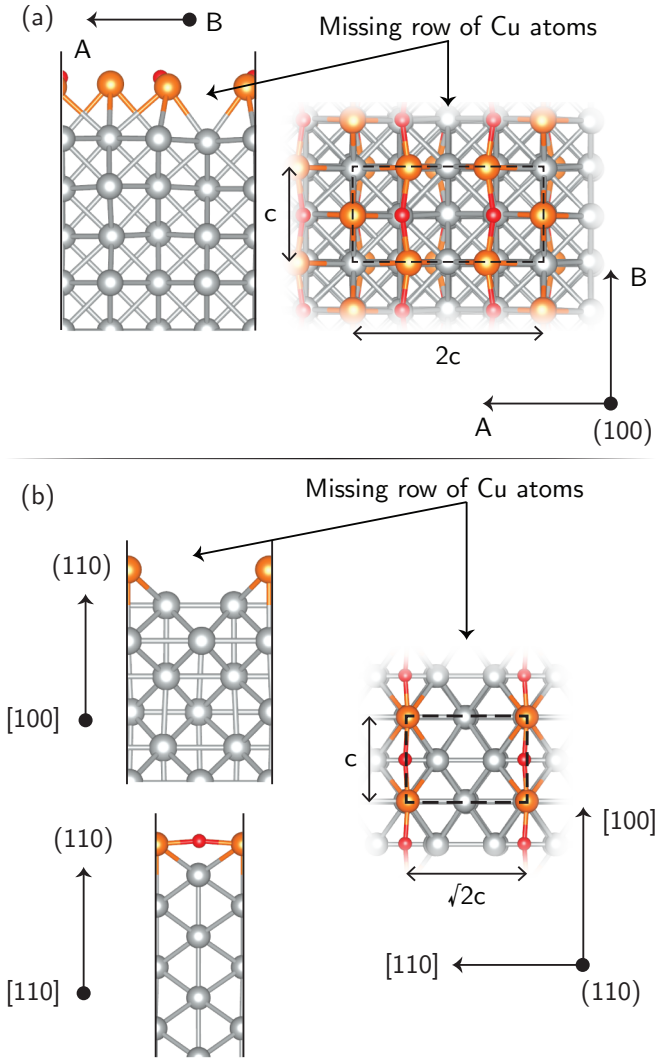

Figure 2.1: Side and top view of optimized O-terminated Cu thin films. (a) Cu(100)-$(2\sqrt{2} \times \sqrt{2})R45°$-O, and (b) Cu(110)-$p(2 \times 1)$-O. Copper atoms away from surfaces are shown in silver, while copper and oxygen atoms at the surface are shown in orange and red, respectively.

2.3.2 Computational details

The electronic properties of Cu thin films are studied using density functional theory (DFT) as implemented by the software package OpenMX [32] and density functional tight binding (DFTB) as implemented by QuantumWise [33–35]. The PBE [36] formulation of the generalized gradient approximation (GGA) exchange-correlation functional is used throughout. Norm-conserving pseudopotentials [37] and a strictly localized pseudoatomic orbital (PAO) basis [38, 39] are used. The basis sets used are 6.0H-s4p2d2 and 7.0-s2p2 for Cu and O, respectively. The first part of the basis set notation gives the PAO cutoff

radius in Bohr, while the second part indicates the orbitals used for the valence electrons, e.g., O 7.0-s2p2 corresponds to a cutoff radius of 7.0 Bohr and 8 basis functions (2 s functions and 6 p functions). Structural parameters derived from this Cu basis set agree well with experiment, giving an optimal fcc lattice parameter of 3.63 Å and a bulk modulus of 135 GPa compared to experimental values of 3.615 Å and 137 GPa, respectively. A supercell approach is taken whereby the thin films are modeled with periodic boundary conditions in the plane of the film and a minimum of 1 nm of vacuum is introduced in the direction normal to the thin films' surface to prevent interaction of periodic images. The Brillouin zones of the two sets of structures are sampled using a $11 \times 5 \times 1$ and $7 \times 9 \times 1$ k-point grid generated according to the Monkhorst-Pack method [40], respectively; and a grid corresponding to an energy cutoff of 200 Ry is used for numeric integration of real-space quantities.

The upper and lower surfaces of the thin films are optimized separately with a frozen bulk Cu back plane as shown in Fig. 2.1 until forces acting on individual atoms remain below 3×10^{-4} Hartree/Bohr. After optimization of the local surface environment containing the oxide, separate upper and lower surfaces approximately 0.8 nm thick are joined together and the thickness of the resulting film is increased by the addition of bulklike fcc Cu, with suitable lattice parameter, at the center as required to achieve the desired thickness.

The electronic transport properties of the resulting structures are studied in the ballistic transport regime using an approach based on Green's functions [34] within the context of the Landauer-Büttiker formalism [41, 42].

The maximum current that can flow through a finite central region connected to two semi-infinite leads is related to the probability of an electron being transmitted through it via the relation

$$I(V) = \frac{e}{h} \sum_{\sigma} \int T_{\sigma}(E, V) \left[f\left(E, \mu_R, \ T_R\right) - f\left(E, \mu_L, T_L\right) \right] dE \,, \tag{2.1}$$

where e is the electron charge, h Planck's constant, $T_{\sigma}(E, V)$ is the transmission coefficient per spin channel σ at energy E and applied bias V, f is the Fermi-Dirac distribution, T_L (T_R) and μ_L (μ_R) are the temperature and chemical potential of the left (right) electrode, and the applied bias is given by

$$V = \frac{\mu_R - \mu_L}{e}. \tag{2.2}$$

For small applied biases we can approximate the conductance by its linear-response zero-temperature limit in the non-spin polarized case as

$$G = \frac{2e^2}{h} T(E_F, V = 0), \tag{2.3}$$

where we consider the transmission spectrum and electronic structure to remain unperturbed by the application of a small voltage across an infinitely long system. At finite temperatures, the largest contributions to the integral in Eq. 2.1 will come from the transport of electrons with energies closer to the Fermi level; in particular, assuming slow variations of the transmission coefficients with energy, the previous result can be extended beyond the zero-temperature limit [42].

Throughout this paper, we have computed the transmission coefficients over a 100 meV energy range centered about the Fermi level $T(E_F \pm 50\ meV, V = 0)$ as a measure of the films' maximum conductance within the linear-response approximation. This allows an assessment of the variation of transmission coefficients around the Fermi level – and hence the validity of Eq. 2.3 – and a more robust benchmark of different methods for computing transport properties.

Integration of quantities in electronic transport calculations is performed by sampling with 301 k points along the periodic cell direction perpendicular to the transmission direction and a single k point along the nonperiodic direction. The computational demand involved in the calculation of transmission coefficients using first principles DFT becomes prohibitively large as the thickness of the films increase. Therefore we assess the suitability of semiempirical DFTB for calculating electron transmission probabilities in copper nanostructures with oxidized surfaces and under tensile strain. Two sets of DFTB parameters are employed and compared against first principles DFT calculations. The first set of parameters is the matsci set (version 0-3) [43, 44] and a second parameter set labeled 'custom', which has been optimized specifically to have a physical band gap for bulk Cu_2O, which is not reproduced from the matsci parameters.

In the DFTB method [45, 46], two center interactions are computed by using Slater-Koster integral tables which describe the Hamiltonian and overlap matrix elements between atoms on a equidistant grid [47]. The 'custom' DFTB parameter set was generated by starting from all-electron DFT wave functions and optimizing interactions between pairs of atoms such that when put into a bulk crystal structure, the experimental band structure of the crystal was re-

covered. These differ from the matsci parameter set in that specific orbitals and wavefunctions were targeted to be optimized in order to fit experimental band structures. The procedure followed in their generation is similar to that described by Wahiduzzaman *et al.* [48].

These DFTB calculations also serve as the basis for the determination of transmission pathways [49] within the thin films, which provide a spatially resolved projection of total electron transmission into local coefficients defined between pairs of atoms: For any plane perpendicular to the transmission direction which divides the system in two regions A and B, it holds that

$$T(E) = \sum_{i \in A, j \in B} T_{ij}(E), \tag{2.4}$$

where i and j denote atoms located on each side of said plane. In the case of perfectly periodic systems such as those studied here, the use of a Green's function approach is not necessary in order to obtain the total transmission coefficients at zero applied bias $T(E, V = 0)$, but it is required for computing their projection into spatially localized transmission coefficients [see appendix B.2.1].

2.4 Results and Discussion

2.4.1 DFT vs. DFTB: charge transport properties

The DFT calculated total transmission as a function of film thickness and cell parameter c for directions A and B is shown in Fig. 2.2. Inspection of the transmission per unit area at the Fermi level reveals a decrease in the maximum current density that can flow through the films with increasing tensile strain [see Table 2.1]: As the metal atoms in the structure become further apart and the overlap between their orbitals becomes smaller, the number of conducting paths decreases as it becomes more difficult for electrons to propagate between atoms.

Table 2.1 also shows an increase of transmission per unit area at the Fermi level $\tau(E_F)$ with increasing thickness: The addition of new conducting paths further away from the surface, and hence with a lower associated probability to scatter off it, results in a net increase of the total current density that flows through the

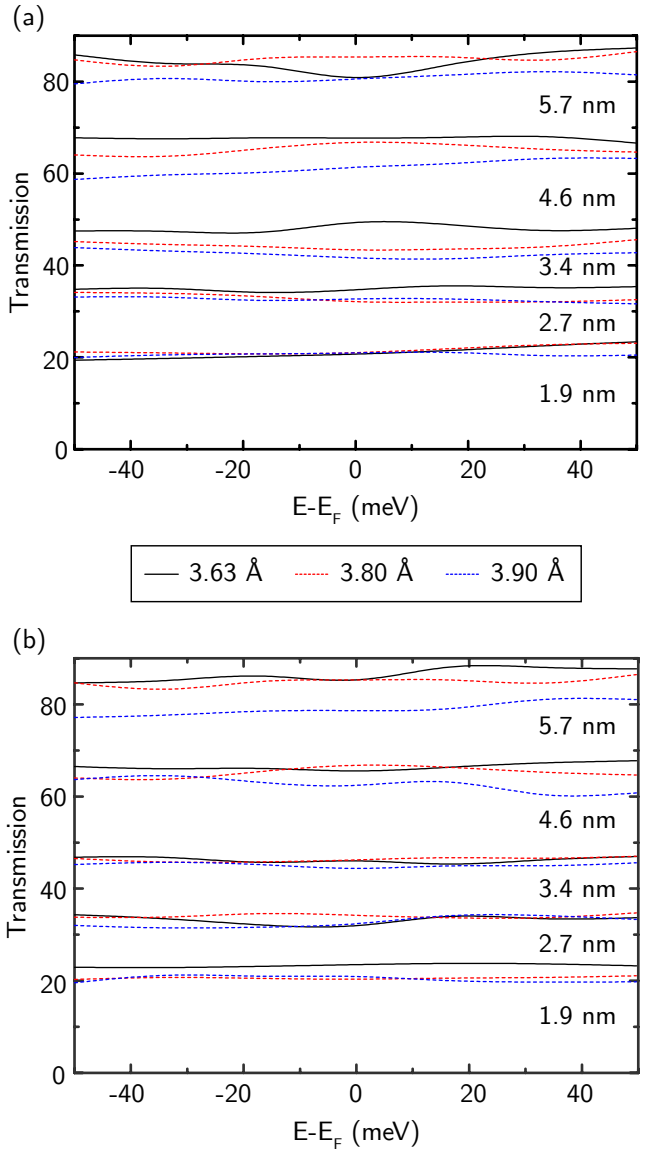

Figure 2.2: DFT-computed transmission for film thickness of 2.0, 2.7, 3.4, 4.5 and 5.6 nm with varying values of the lattice parameter c for inequivalent transport directions (a) A and (b) B as indicated in Fig. 2.1(a). Zero of energy is taken to be at the Fermi level.

thicker films. Figure 2.3 illustrates these findings by plotting the ratio between the transmission per unit area of the films and that of bulk copper versus film thickness for all considered strains, which is equivalent to the ratio between their conductances.

Similar behavior is observed in DFTB calculations using both parameter sets. Transmission coefficients for all cases shown in Fig. 2.2 have been computed using both parameter sets. Histograms showing deviations from DFT transmission values at the Fermi level are shown in Fig. 2.4. The custom parameter

Table 2.1: DFT calculated transmission per unit area at E_F for structures shown in Fig. 2.1(a) with varying thickness and biaxial tensile strain.

	$\tau(E_F)$ (nm^{-2})		
Strain $\rightarrow$	0 %	4.7 %	7.4%
(100)-[100] A			
1.9 nm	7.34	7.08	7.00
2.7 nm	8.99	8.15	8.35
3.4 nm	10.04	8.22	7.67
4.5 nm	10.43	9.52	8.46
5.6 nm	10.02	9.76	8.88
(100)-[100] B			
1.9 nm	8.32	6.81	6.95
2.7 nm	8.26	8.27	7.67
3.4 nm	9.35	8.75	8.17
4.5 nm	10.09	9.52	8.60
5.6 nm	10.57	9.76	8.67

set is found to provide a description of the films' electron transport properties closer to that of DFT, with a maximum error of 10% and a standard deviation of 4.4 versus values found for the matsci parameter set of 13% and 6.3, respectively. DFTB hence provides a reasonable approximation for transmission in Cu/O systems at a fraction of the computational cost of DFT and is able to describe thin films under tensile strain with similar accuracy. Figure 2.5 illustrates the evolution of film conductance with thickness depending on transport direction and local surface environment by showing the transmission per unit area of both structure sets and transport directions with respect to that of bulk copper for increasing film thickness, as computed with DFTB using the custom parameter set.

2.4.2 Transmission pathways

The total transmission coefficients provide information about the total number of electron transmission channels through the films as a whole, while the use of transmission pathways allows for a spatially resolved analysis of charge transport. Transmission pathways have been calculated at the Fermi level E_F using DFTB with the custom parameter set for transport along $[100]$ and $[110]$ orientations of both structure sets. These localized pathways between individual atom pairs within the thin films enable an extraction of local electron transmission

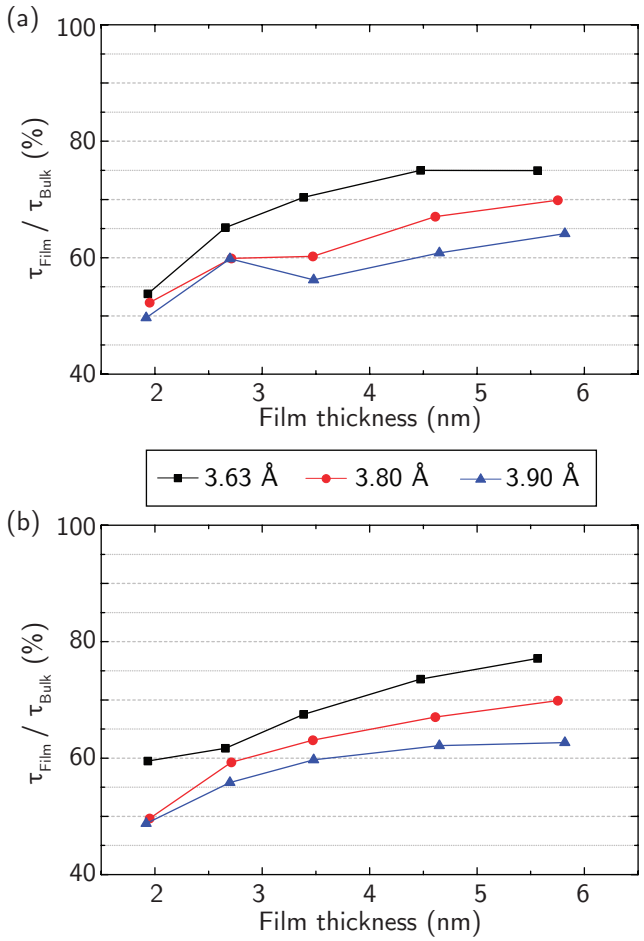

Figure 2.3: DFT calculated ratios between the transmission per unit area of structures shown in Fig. 2.1(a) and bulk Cu. The lengths labeling each curve in the legend indicate the lattice constant (biaxial strain).

coefficients as a function of depth into the copper films, as shown in Fig. 2.6. The calculated transmission per unit area near the oxidized surfaces is much lower than at the center of the films, which reveals that the reduction of propagating states caused by the presence of the oxide and its modification of the local electronic structure extends into the film and is not limited to the surface layers. Below the surface oxide layer, transmission per unit area initially increases rapidly with depth and plateaus for distances greater than ≈0.5 nm away from the surface in structures with (100) surface facets [Fig. 2.1(a)]; while plateau values are observed for depths greater than ≈0.35 nm in structures with (110) surface facets [Fig. 2.1(b)]. This variation in depth up to which the presence of the surface oxide suppresses electron transport is attributed to differences in the local surface environment with varying crystallographic orientations. Values of the transmission per unit area for the thinnest film studied in each

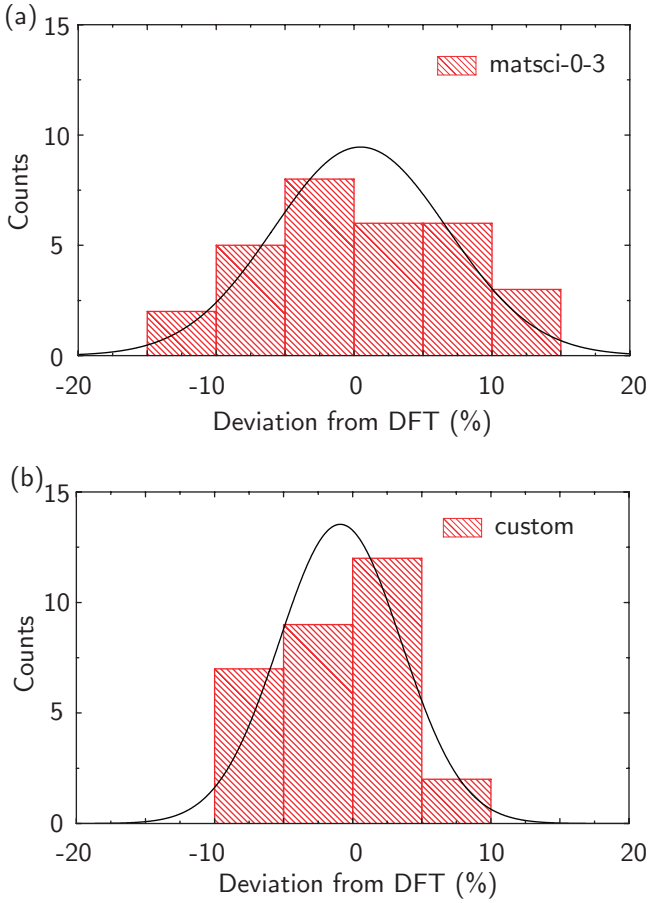

Figure 2.4: Histograms showing the error in transmission coefficients obtained using DFTB with respect to DFT transmission at E_F obtained with (a) matsci, and (b) custom parameter sets. Values for structure set shown in Fig. 2.1(a) with varying thickness and strain have been compared.

structure set (1.9-2.0 nm thick) remain below the maxima seen for the thicker films. With the exception of said films, the depth dependence of the transmission per unit area is remarkably uniform for a given structure set and transport direction. A maximum value of transmission per unit area of 50-80% that of bulk copper is reached for depths greater than 0.35-0.5 nm, depending on surface environment and transport direction, in all studied structures thicker than 2 nm, remaining approximately constant all the way through to the center [see Fig. 2.6]. However, these plateau values remain below the full transmission per unit area of bulk copper despite their apparent convergence at the center of the films, an effect brought on by the presence of surface scattering and its limiting of the number of conduction paths for electrons to propagate along the film.

While the center of the films exhibit an atomic structure similar to that of bulk Cu, and hence one may expect the local number of conducting paths to be the

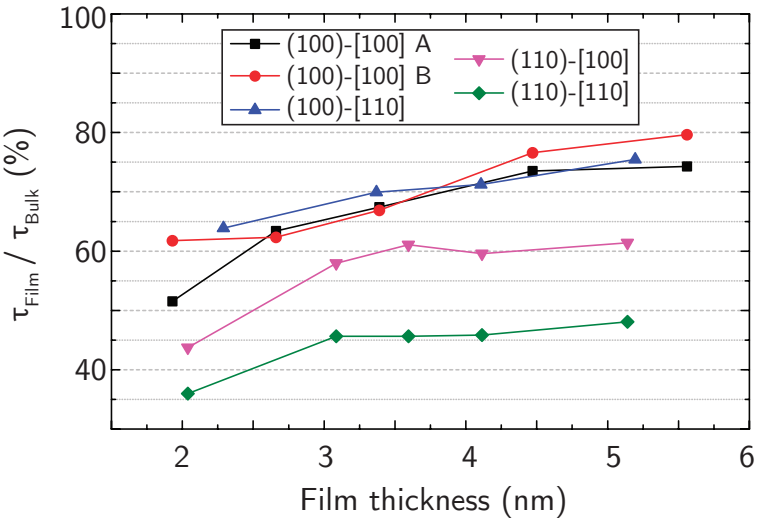

Figure 2.5: Evolution of calculated transmission per unit area with film thickness for both structure sets shown in Fig. 2.1 along the [100] and [110] transport directions. DFTB with the custom parameter set has been employed.

same, the close proximity of surfaces imposes restrictions over the number of independent paths in the films, even at the center. The reason behind these differences might be found in the electronic structure of bulk copper: although it exhibits an isotropic conductivity, inspection of the state distribution across its Brillouin zone (BZ) reveals that not all directions are equivalent in terms of states which propagate at the Fermi level: While states can be found along Σ and Δ paths –associated with $[110]$ and $[100]$ directions, respectively– there are no states along the Λ path –associated with direction $[111]$–, a feature made evident by the shape of the Fermi surface and its vanishing DOS along directions perpendicular to the hexagonal faces of the BZ [50]. It is worth noting that the depth of influence of the surface on electronic transport properties found in this study may be modified when introducing the effects of inelastic sources of scattering and decoherence effects into the model.

2.4.3 Surface scattering model

The previous analysis of the transmission pathways results suggests that the total transmission in all but the thinnest films of each structure set can be decomposed as a sum of two contributions: a *surface* contribution describing transmission for depths less than 0.35-0.5 nm into the films and a *plateau* contribution describing transport for greater depths. In terms of transmissions per unit area (τ), we may write:

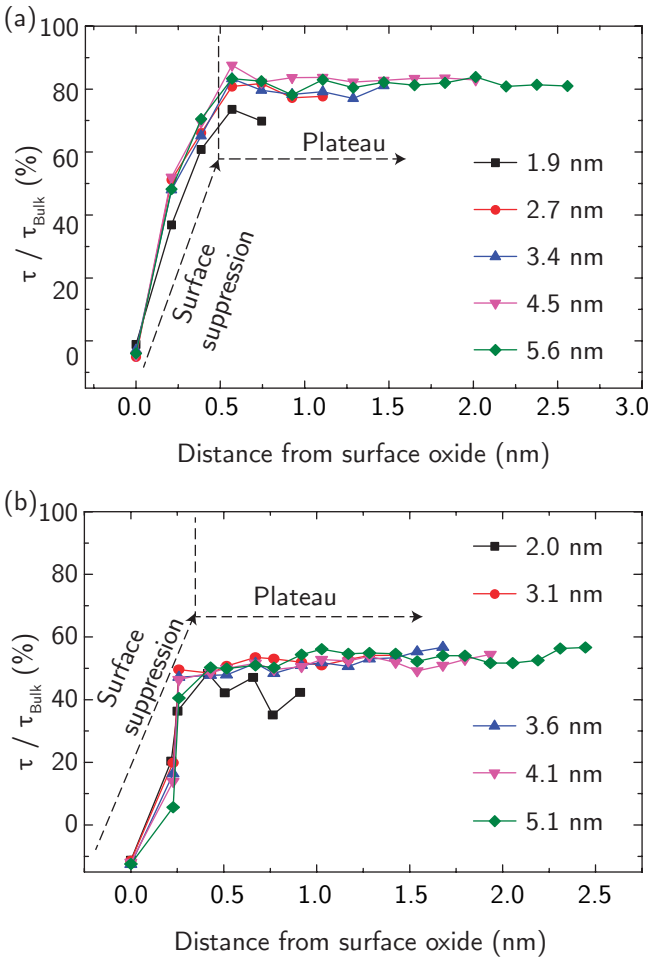

Figure 2.6: Transmission per unit area at the Fermi level as a function of distance from the thin film's surface oxide. Transmission is strongly suppressed near films' surfaces, below the surface transmission per unit area initially increases rapidly and plateaus for depths greater than ≈0.35-0.5 nm, dependent on surface environment.

$$T = A^{Surf}\tau_{Surf} + A^{Plat}\tau_{Plat}, \tag{2.5}$$

where we have split the cross-sectional area of the film into the area of the surface and plateau regions, and each term on the right hand side is proportional to the maximum current that can flow through the corresponding section of the film. Since the depth up to which transmission is strongly suppressed by the surface does not vary with thickness, we shall consider A^{Surf} to be constant for all structures – except the thinnest films – within each set. We then proceed to fit Eq. 2.5 in order to obtain values for τ_{Surf} and τ_{Plat} at the Fermi level.

Table 2.2 shows the obtained values for transmission per unit area on each region for both structure sets and transport directions, scaled by values obtained

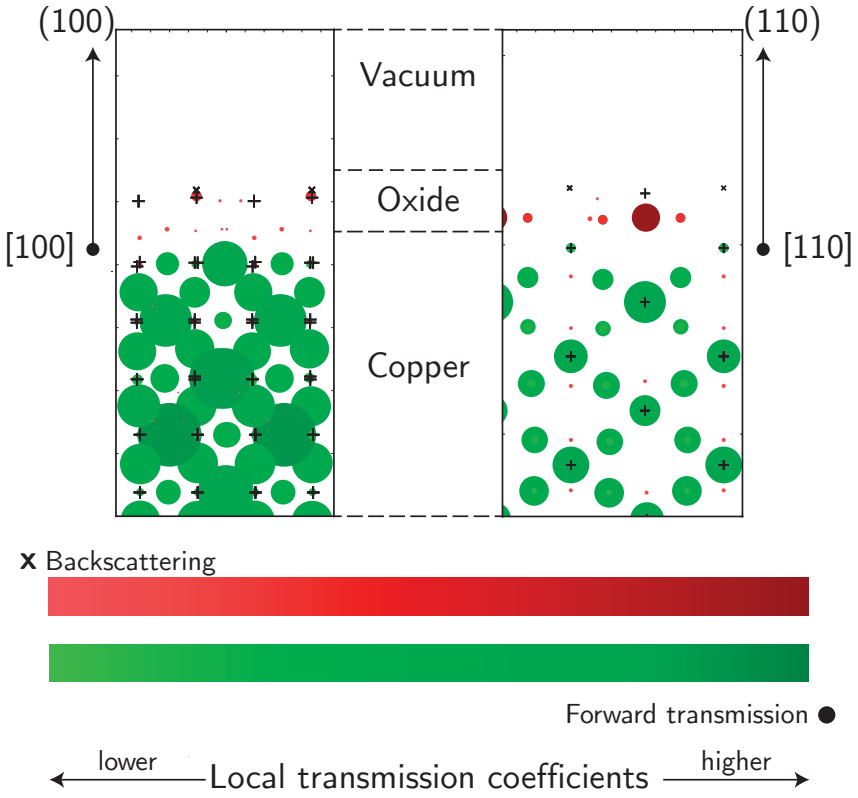

Figure 2.7: Projections of transmission pathways at the Fermi level at a plane perpendicular to the transport direction and located halfway between atomic planes. Both the size of the bubbles and their color represent the magnitude of each pathway. Cu atoms are represented by + signs, while O atoms at the surface are shown as **x**. Transport along direction A of the structure shown on Fig. 2.1(a) is shown on the left; while the plot on the right corresponds to transport along [110] in the structure shown in Fig. 2.1(b).

Table 2.2: Computed values for local transmission per unit area with respect to bulk Cu for both structure sets using the custom DFTB parameter set. Values have been obtained by performing a linear fit of obtained data to Eq. 2.5; correlation coefficients greater than 0.99 were obtained in all cases. Values shown in parenthesis have been obtained with DFT.

	$\tau_{Surf}/\tau_{Bulk}(\%)$	$\tau_{Plat}/\tau_{Bulk}(\%)$
(100)-[100] A	38 (54)	85 (77)
(100)-[100] B	19 (23)	97 (88)
(100)-[110]	39	86
(110)-[100]	44	65
(110)-[110]	36	52

for bulk Cu. For the first set of structures, A and B transport directions correspond to bulk [100] deep into the film as asymmetry is only introduced near the surface. It is seen that while the surface environment for electrons propagating along the B axis – in which the missing rows of Cu atoms are parallel to the transport direction – is more resistive, it has less of an impact on the resistance of the plateau region than for electrons traveling along the A axis. This correlates to the fact that total film transmission per unit area increases at a higher rate for transport along the B axis as thickness increases, as can be seen in Fig. 2.5. In the case of these two transport directions, we have included results obtained with DFT as an assessment of the error introduced by the use of DFTB on the values of fitted parameters: While differences on τ_{Surf} can be as high as 40%, qualitative trends hold and errors on τ_{Plat} remain within the expected 10%.

Results for transport along the [100] crystallographic direction for the second set of structures show its corresponding surface environment's resistance to be similar to that of transport along (100)-[100] A, although it results in a higher resistance at the plateau region, a feature evident in the fact that its transmission per unit area increases less than for structures in the first set in the 3-5 nm thickness range [see Fig. 2.5]. Finally, results for transport along the [110] direction show both surface environments to be similarly resistive, with structures with (110) surface facets exhibiting lower transmission per unit area in the plateau region. Overall, the set of structures with (110) surfaces exhibit stronger anisotropy, as shown by the vertical separation between curves corresponding to both of its transport directions in Fig. 2.5.

Figure 2.7 shows a visual representation of transmission pathways crossing a plane perpendicular to the transport direction, and located halfway between two atomic planes. Two cases are illustrated: (100)-[100] A and (110)-[110]. Transmission along [100] is shown to always take place at an angle with respect to the transport direction, while transport along [110] is shown to have a sizeable parallel component. This is shown by the fact that the largest transmission pathways (bubbles) along [100] are found halfway between Cu atoms (+), whilst the largest bubbles are found to lay directly on top of Cu atoms for transport occurring along [110]. Forward transmission is found to be severely suppressed when approaching both surfaces, with an associated increase in backscattering coefficients.

2.5 Conclusions

It is found that the DFTB calculations of electron transmission performed provide a reasonable approximation to DFT for Cu/O systems, with the custom parameter set performing closer to DFT (error $< 10\%$) when compared to the matsci set (error $< 13\%$). This enables the calculation of transport properties of structures with a larger number of atoms and hence more realistic models of nanoscale interconnects. It is found that oxidation of the surface of copper thin films results in a dramatic reduction of electron transmission directly at the interface, an effect which severely degrades local electron transmission coefficients for distances of up to approximately 0.35-0.5 nm into the films, depending on the crystallographic orientation of exposed surface facets – a result which highlights the importance and provides a scale length for interface effects in nanoscale copper systems – although introducing the effects of inelastic scattering and other decoherence effects might modify surface effects' depth of influence discussed in this paper. Maximizing conductance in nanoscale copper interconnects requires careful interface design between conductor and barrier layer as the chemical environment at the surface and orientation along which transport occurs can have critical impact for Cu systems with feature lengths below 10 nm. Tensile strain tends to be detrimental to film conductance as the transmission per unit area is found to be reduced for films under biaxial tensile strain studied in this paper. For film thicknesses of $\approx$3 nm and greater, a core region for which transmission is somewhat independent of depth is formed, although bulklike transmission has not been observed even at the center of films as thick as 5.6 nm. The use of a localized transmission model shows the resistance of the studied films to dramatically increase near the surface; whereas the increase in resistance at the core region is found to strongly depend on the surface environment and transport direction.

2.6 Acknowledgments

This work was performed as part of the Intel-Tyndall research collaboration sponsored by Intel Components Research. A.S.S. was funded under an Irish Research Council postgraduate scholarship. Partial funding was provided by the Science Foundation Ireland Investigator program, Grant No. 13/IA/1956. We are grateful to QuantumWise A/S for support and access to the QuantumWise simulation software. Atomistic visualizations were rendered using VESTA [51].

References

[1] Werner Steinhögl, Günther Schindler, Gernot Steinlesberger, and Manfred Engelhardt. Size-dependent resistivity of metallic wires in the mesoscopic range. *Phys. Rev. B*, 66:075414, 2002.

[2] W. Zhang, S. H. Brongersma, Z. Li, D. Li, O. Richard, and K. Maex. Analysis of the size effect in electroplated fine copper wires and a realistic assessment to model copper resistivity. *J. Appl. Phys.*, 101(6):063703, 2007.

[3] K. Fuchs. The conductivity of thin metallic films according to the electron theory of metals. *Math. Proc. Cambridge Philos. Soc.*, 34:100–108, 1938.

[4] A. F. Mayadas and M. Shatzkes. Electrical-resistivity model for polycrystalline films: The case of arbitrary reflection at external surfaces. *Phys. Rev. B*, 1:1382–1389, 1970.

[5] Daniel Josell, Sywert H. Brongersma, and Zsolt Tokei. Size-dependent resistivity in nanoscale interconnects. *Annu. Rev. Mater. Res.*, 39:231–254, 2009.

[6] Ricardo Henriquez, Simon Cancino, Andres Espinosa, Marcos Flores, Thomas Hoffmann, German Kremer, Judit G. Lisoni, Luis Moraga, Roberto Morales, Simon Oyarzun, Marco Antonio Suarez, Alejandro Zúñiga, and Raul C. Munoz. Electron grain boundary scattering and the resistivity of nanometric metallic structures. *Phys. Rev. B*, 82:113409, 2010.

[7] Ricardo Henriquez, Marcos Flores, Luis Moraga, German Kremer, Claudio González-Fuentes, and Raul C. Munoz. Electron scattering at surfaces and grain boundaries in thin Au films. *Appl. Surf. Sci.*, 273(0):315 – 323, 2013.

[8] Tik Sun, Bo Yao, Andrew P. Warren, Katayun Barmak, Michael F. Toney, Robert E. Peale, and Kevin R. Coffey. Dominant role of grain boundary scattering in the resistivity of nanometric Cu films. *Phys. Rev. B*, 79:041402, 2009.

[9] Tik Sun, Bo Yao, Andrew P. Warren, Katayun Barmak, Michael F. Toney, Robert E. Peale, and Kevin R. Coffey. Surface and grain-boundary scattering in nanometric Cu films. *Phys. Rev. B*, 81:155454, 2010.

[10] J. S. Chawla and D. Gall. Specular electron scattering at single-crystal Cu(001) surfaces. *Appl. Phys. Lett.*, 94(25):252101, 2009.

[11] J. S. Chawla, F. Gstrein, K. P. O'Brien, J. S. Clarke, and D. Gall. Electron scattering at surfaces and grain boundaries in Cu thin films and wires. *Phys. Rev. B*, 84:235423, 2011.

[12] J. S. Chawla, F. Zahid, H. Guo, and D. Gall. Effect of O_2 adsorption on electron scattering at Cu(001) surfaces. *Appl. Phys. Lett.*, 97(13):132106, 2010.

[13] Ferdows Zahid, Youqi Ke, Daniel Gall, and Hong Guo. Resistivity of thin Cu films coated with Ta, Ti, Ru, Al, and Pd barrier layers from first principles. *Phys. Rev. B*, 81:045406, 2010.

[14] S. M. Rossnagel and T. S. Kuan. Alteration of Cu conductivity in the size effect regime. *J. Vac. Sci. Technol. B*, 22(1):240–247, 2004.

[15] P. Y. Zheng, R. P. Deng, and D. Gall. Ni doping on Cu surfaces: Reduced copper resistivity. *Appl. Phys. Lett.*, 105(13):131603, 2014.

[16] H.C. Zeng, R.A. McFarlane, and K.A.R. Mitchell. A LEED crystallographic investigation of some missing row models for the Cu(100)-($2\sqrt{2}$ $\times$ $\sqrt{2}$)R45°-O surface structure. *Surf. Sci.*, 208(1):L7 – L14, 1989.

[17] A Atrei, U Bardi, G Rovida, E Zanazzi, and G Casalone. Test of structural models for Cu(001)-($\sqrt{2}$ $\times$ $2\sqrt{2}$) R45°-O by LEED intensity analysis. *Vacuum*, 41(1):333 – 336, 1990.

[18] M. Kittel, M. Polcik, R. Terborg, J.-T. Hoeft, P. Baumgärtel, A.M. Bradshaw, R.L. Toomes, J.-H. Kang, D.P. Woodruff, M. Pascal, C.L.A. Lamont, and E. Rotenberg. The structure of oxygen on Cu(100) at low and high coverages. *Surf. Sci.*, 470(3):311 – 324, 2001.

[19] N. Bonini, A. Kokalj, A. Dal Corso, S. de Gironcoli, and S. Baroni. Structure and dynamics of the missing-row reconstruction on O/Cu(001) and O/Ag(001) . *Surf. Sci.*, 600(23):5074 – 5079, 2006.

[20] M. J. Harrison, D. P. Woodruff, J. Robinson, D. Sander, W. Pan, and J. Kirschner. Adsorbate-induced surface reconstruction and surface-stress

changes in Cu(100)/O: Experiment and theory. *Phys. Rev. B*, 74:165402, 2006.

[21] X. Duan, O. Warschkow, A. Soon, B. Delley, and C. Stampfl. Density functional study of oxygen on Cu(100) and Cu(110) surfaces. *Phys. Rev. B*, 81:075430, 2010.

[22] Mehmet Z. Baykara, Milica Todorović, Harry Mönig, Todd C. Schwendemann, Özhan Ünverdi, Lucia Rodrigo, Eric I. Altman, Rubén Pérez, and Udo D. Schwarz. Atom-specific forces and defect identification on surface-oxidized Cu(100) with combined 3D-AFM and STM measurements. *Phys. Rev. B*, 87:155414, 2013.

[23] Sarah L. T. Jones, Alfonso Sanchez-Soares, John J. Plombon, Ananth P. Kaushik, Roger E. Nagle, James S. Clarke, and James C. Greer. Electron transport properties of sub-3-nm diameter copper nanowires. *Phys. Rev. B*, 92:115413, 2015.

[24] Flemming Besenbacher and Jens K. Nørskov. Oxygen chemisorption on metal surfaces: General trends for Cu, Ni and Ag. *Progress in Surf. Sci.*, 44(1):5 – 66, 1993.

[25] Y. Uehara, T. Matsumoto, and S. Ushioda. Identification of O atoms on a Cu(110) surface by scanning tunneling microscope light emission spectra. *Phys. Rev. B*, 66:075413, 2002.

[26] Shohei Kishimoto, Masami Kageshima, Yoshitaka Naitoh, Yan Jun Li, and Yasuhiro Sugawara. Study of oxidized Cu(110) surface using noncontact atomic force microscopy. *Surf. Sci.*, 602(13):2175 – 2182, 2008.

[27] Yan Jun Li, Seung Hwan Lee, Yukinori Kinoshita, Zong Min Ma, Huanfei Wen, Hikaru Nomura, Yoshitaka Naitoh, and Yasuhiro Sugawara. Growth models of coexisting p(2 $\times$ 1) and c(6 $\times$ 2) phases on an oxygen-terminated Cu(110) surface studied by noncontact atomic force microscopy at 78 K. *Nanotechnology*, 27(20):205702, 2016.

[28] J. Bamidele, Y. Kinoshita, R. Turanský, S. H. Lee, Y. Naitoh, Y. J. Li, Y. Sugawara, I. Štich, and L. Kantorovich. Chemical tip fingerprinting in scanning probe microscopy of an oxidized Cu(110) surface. *Phys. Rev. B*, 86:155422, 2012.

[29] J. Bamidele, S.H. Lee, Y. Kinoshita, R. Turanský, Y. Naitoh, Y.J. Li, Y. Sugawara, I. Štich, and L. Kantorovich. Vertical atomic manipulation with

dynamic atomic-force microscopy without tip change via a multi-step mechanism. *Nat. Commun.*, 5, 2014.

[30] J. Bamidele, Y. Kinoshita, R. Turanský, S. H. Lee, Y. Naitoh, Y. J. Li, Y. Sugawara, I. Štich, and L. Kantorovich. Image formation and contrast inversion in noncontact atomic force microscopy imaging of oxidized Cu(110) surfaces. *Phys. Rev. B*, 90:035410, 2014.

[31] N. N. Greenwood and A. Earnshaw. *Chemistry of the elements*. Butterworth-Heinemann, Oxford OX2 6DP, United Kingdom, 1997.

[32] OPENMX software package. *www.openmx-square.org (accessed August 2016)*.

[33] Atomistix ToolKit version 2015-1 QuantumWise A/S. *www.quantumwise.com (accessed August 2016)*.

[34] Mads Brandbyge, José-Luis Mozos, Pablo Ordejón, Jeremy Taylor, and Kurt Stokbro. Density-functional method for nonequilibrium electron transport. *Phys. Rev. B*, 65:165401, 2002.

[35] José M Soler, Emilio Artacho, Julian D Gale, Alberto Garcia, Javier Junquera, Pablo Ordejon, and Daniel Sanchez-Portal. The SIESTA method for ab initio order-N materials simulation. *J. Phys.: Condens. Matter*, 14(11):2745, 2002.

[36] J.P. Perdew, K. Burke, and M. Ernzerhof. Generalized gradient approximation made simple. *Phys. Rev. Lett.*, 77:3865–3868, 1996.

[37] I. Morrison, D.M. Bylander, and L. Kleinman. Non-local Hermitian norm-conserving Vanderbilt pseudopotenial. *Phys. Rev. B*, 47:6728–6731, 1993.

[38] T. Ozaki. Variationally optimized atomic orbitals for large-scale electronic structures. *Phys. Rev. B*, 67:155108, 2003.

[39] T. Ozaki and H. Kino. Numerical atomic basis orbitals from H to Kr. *Phys. Rev. B*, 69:195113, 2004.

[40] Hendrik J. Monkhorst and James D. Pack. Special points for Brillouin-zone integrations. *Phys. Rev. B*, 13:5188–5192, 1976.

[41] R. Landauer. Spatial variation of currents and fields due to localized scatterers in metallic conduction. *IBM J. Res. Dev.*, 1(3):223–231, 1957.

[42] Supriyo Datta. *Electronic transport in mesoscopic systems*. Cambridge University Press, Cambridge CB2 8BS, United Kingdom, 1995.

[43] dftb.org. *http://www.dftb.org (accessed August 2016)*.

[44] N. Jardillier. PhD thesis, Universite Montpellier II, Montpellier, 2006.

[45] G. Seifert, D. Porezag, and Th. Frauenheim. Calculations of molecules, clusters, and solids with a simplified LCAO-DFT-LDA scheme. *Int. J. Quantum Chem.*, 58(2):185–192, 1996.

[46] Gotthard Seifert and Jan-Ole Joswig. Density-functional tight binding—an approximate density-functional theory method. *Wiley Interdiscip. Rev.: Comput. Mol. Sci.*, 2(3):456–465, 2012.

[47] J. C. Slater and G. F. Koster. Simplified LCAO method for the periodic potential problem. *Phys. Rev.*, 94:1498–1524, 1954.

[48] Mohammad Wahiduzzaman, Augusto F. Oliveira, Pier Philipsen, Lyuben Zhechkov, Erik van Lenthe, Henryk A. Witek, and Thomas Heine. DFTB parameters for the periodic table: Part 1, electronic structure. *J. Chem. Theory Comput.*, 9(9):4006–4017, 2013.

[49] G.C. Solomon, C. Herrmann, T. Hansen, V. Mujica, and M.A. Ratner. Exploring local currents in molecular junctions. *Nat. Chem.*, 2:223, 2010.

[50] Benjamin Segall. Fermi surface and energy bands of copper. *Phys. Rev.*, 125:109–122, 1962.

[51] Koichi Momma and Fujio Izumi. *VESTA3* for three-dimensional visualization of crystal, volumetric and morphology data. *J. Appl. Crystallogr.*, 44(6):1272–1276, 2011.

Chapter 3

Electron transport properties of sub-3-nm diameter copper nanowires

3.1 Abstract

Density functional theory and density functional tight-binding are applied to model electron transport in copper nanowires of approximately 1 nm and 3 nm diameters with varying crystal orientation and surface termination. The copper nanowires studied are found to be metallic irrespective of diameter, crystal orientation and/or surface termination. Electron transmission is highly dependent on crystal orientation and surface termination. Nanowires oriented along the [110] crystallographic axis consistently exhibit the highest electron transmission while surface oxidized nanowires show significantly reduced electron transmission compared to unterminated nanowires. Transmission per unit area is calculated in each case; for a given crystal orientation we find that this value decreases with diameter for unterminated nanowires but is largely unaffected by diameter in surface oxidized nanowires for the size regime considered. Transmission pathways show that transmission is larger at the surface of unterminated nanowires than inside the nanowire, and that transmission at the nanowire surface is significantly reduced by surface oxidation. Finally, we present a simple model which explains the transport per unit area dependence on diameter based on transmission pathways results.

3.2 Introduction

Due to continued nanoelectronics scaling, metal interconnects as well as transistors in integrated circuits are becoming ever smaller and are approaching atomic scale dimensions [1]. As a consequence, understanding the effects of size-dependent phenomena on material properties is becoming ever more critical to enable efficient device performance. Present day transistor technologies use copper as an interconnect material, however it is unknown if at the small cross-sections required for future technologies copper will be able to fulfill this function effectively due to increased resistances; measured line resistivity increases dramatically for Cu nanowires (NWs) compared to bulk materials [2, 3]. It is required that the electrical conductivity of small cross section copper nanostructures be understood to maintain acceptable power consumption in future nanoelectronics generations. In particular the contribution of the individual scattering sources, such as surfaces [4], grain boundaries [5], electron-phonon interactions [6] and impurities, to overall resistivity needs to be assessed to aid development of interconnects which minimize line resistance. A succinct overview of these issues can be found in the review of Josell, Brongersma and Tőkei. [7]

In general the dominant scattering mechanism in metal nanostructures is dependent on processing conditions and the geometry of the resulting nanostructures. For example Henriquez *et al.* [8, 9] have reported electron scattering to vary with grain size in the case of gold thin films. Grain boundary scattering is found to dominate for grain sizes much smaller than the electron mean free path, while for much larger grain sizes it is the surface that is critical to resistivity. For grain sizes comparable to the mean free path, both mechanisms are responsible for the increases resistances relative to bulk gold. Meanwhile, in the case of copper thin films Sun *et al.* [10, 11] have reported that it is grain boundary scattering which dominates. Zhang *et al.* [3] report that the temperature dependence of resistivity in Cu NWs is consistent with surface scattering as the dominant scattering source. This report is corroborated by Graham *et al.* [12], who find that diffuse surface scattering and line edge roughness is consistent with the temperature dependence of resistivity for Cu NWs down to 25 nm diameter and that the role of grain boundary scattering is minimal. Similarly, Wang *et al.* [13] report that resistivity is dominated by diffuse surface scattering for 20 - 100 nm Cu NWs. Thus though the situation for metal nanostructures can vary by material and process conditions, the literature to date as pertains to

Cu NWs seems quite emphatic; the surface is the dominant scattering source.

In low dimension Cu films the surface environment has been reported to drastically influence conductivity. In a series of studies, Chawla and co-workers have investigated the scattering at the surfaces of Cu thin films [14–16]. They report that scattering at a Cu-vacuum surface is partially specular, whereas after tantalum deposition the surface scattering becomes diffuse . [14, 16] The effect of oxygen has also been reported, with diffuse scattering again reported after oxidation. [15] The effect of a variety of coating metals on Cu thin films has also been reported from first principles simulations. [17] Metals with a density of states (DOS) comparable to the DOS of surface Cu atoms (Al and Pd) lower resistivity, while those which do not (Ta, Ti and Ru) increase resistivity.

Against this backdrop, it is probable that surface scattering is of particular importance for small diameter Cu NWs and thus we study unterminated (i.e., in vacuum) and oxidized 1 and 3 nm Cu NWs using *ab initio* and semi-empirical computational techniques. A high degree of anisotropy of Cu NW conductivity with crystal orientation has previously been reported using tight-binding computational methods, [18] thus we also consider the effects of crystal orientation. We calculate transmission spectra and transmission pathways [19] in each case for geometry optimized structures. We find a strong dependence of transmission on crystal orientation and termination. [110] NWs consistently show a larger transmission than [100] and [111] NWs. Surface oxidation reduces transmission substantially compared to unterminated NWs. Additionally we find that transmission even for 1 nm unterminated NWs is larger at the NW surface than the core due to the existence of surface states. We provide a simple analysis of transmission in nanoscale Cu wires, which accounts for the trends found in transmission.

3.3 Method

The NW structures studied in this work are based on the bulk fcc Cu structure, with [100]-, [110]- and [111]-oriented NWs chosen with approximately 1 and 3 nm diameters. Due to the small diameter of the NWs studied in this work, atoms at the NW surface will have an especially large contribution to the NW properties e.g., 57%, 59% and 49% of the atoms are at the surface for the [100], [110] and [111] 1 nm NWs, respectively. Hence in these nanostructures, elec-

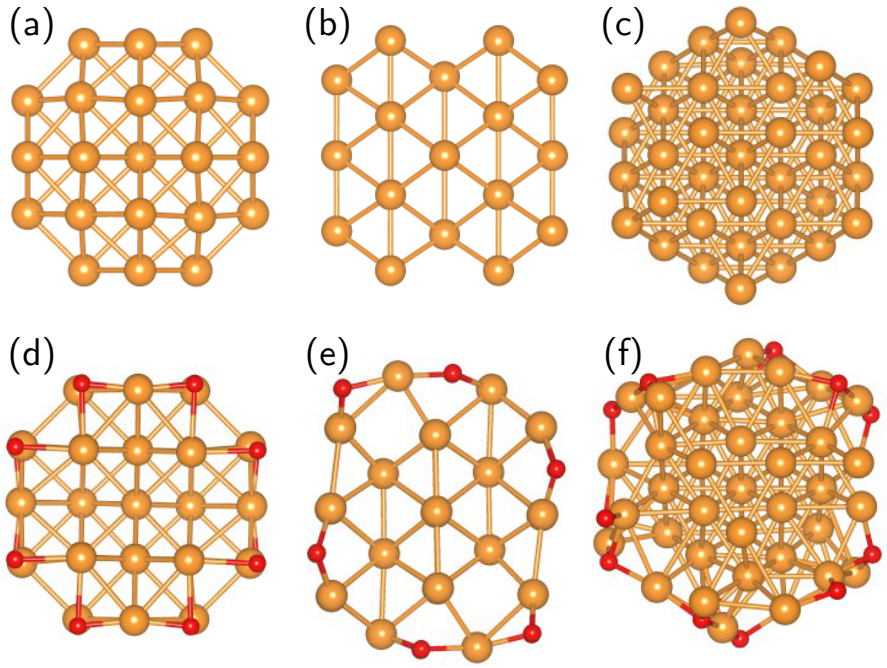

Figure 3.1: Structures of the geometry optimized 1 nm NWs. (a), (b) and (c) show the unterminated [100], [110] and [111] NWs, (d), (e) and (f) show the respective O-terminated NWs. Cu is shown in orange and O in red.

trical resistivity can be expected to be dominated by surface scattering. While standard complimentary metal oxide semiconductor (CMOS) technologies employ Ta based materials as barrier layers to prevent Cu diffusion, deposited Ta has been shown to cause diffusive scattering at the surface of thin Cu films. [16] As scaling continues, the relative contribution of surface scattering to total scattering increases dramatically and along with the barrier thickness means that Ta-based barrier layers may well become unsuitable for efficient interconnect design. To isolate barrier effects we have chosen to restrict this work to consideration of unterminated (i.e., in vacuum) and oxygen terminated (i.e., surface oxidized) NWs. The relaxed (i.e., zero strain) structures of the NWs studied are shown in Fig. 3.1 and Fig. 3.2.

Density functional theory (DFT) as implemented in the OpenMX software package [20] is used to study the electronic properties of the 1 nm diameter Cu NWs. The PBE [21] formulation of the generalized gradient approximation (GGA) exchange and correlation functional is used in conjunction with norm-conserving pseudopotentials [22] and a strictly localized pseudo-atomic orbital (PAO) basis, [23, 24] which enables us to perform the decomposition of the

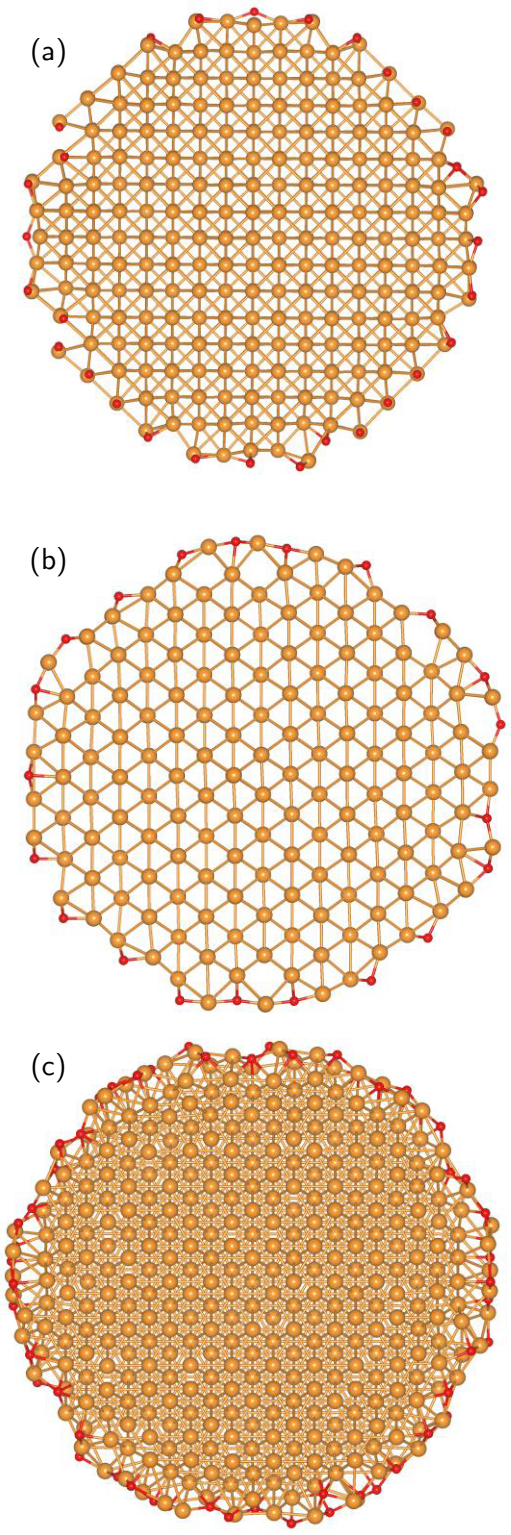

Figure 3.2: Structures of the geometry optimized O-terminated 3 nm NWs. (a), (b) and (c) show the [100], [110] and [111] NWs, respectively. Cu is shown in orange and O in red.

transmission into localized pathways. The basis sets used are 6.0H-s4p2d2 and 7.0-s2p2 for Cu and O respectively. The first part of the basis set notation gives the PAO cutoff radius in Bohr, while the second part indicates the orbitals used for the valence electrons, e.g., O 7.0-s2p2 indicates a cut-off radius of 7.0 Bohr and 8 basis functions (2 s functions and 6 p functions). This Cu basis set agrees reasonably with experiment, yielding an optimal fcc lattice parameter of 3.63 Å and a bulk modulus of 135 GPa compared to experimental values of 3.615 Å and 137 GPa, respectively. The supercell approach is used and because the NWs are periodic only along their axis, a cell size incorporating a minimum of 1 nm of vacuum in the transverse directions is used such that the interaction between periodic images is minimized. The first Brillouin zone is sampled using 11 k-points generated according to the Monkhorst-Pack method [25] and an energy cutoff of 200 Ry is used to generate the grid by which real space quantities are discretized. The atomic positions in the NWs are relaxed until all forces are less than 3x10^{-4} Hartree/Bohr; total energy is also minimized with respect to the lattice cell parameter along the NW axis for each NW orientation. Optimized lattice parameters along the NW axis are given in Table 3.1.

The 3 nm O-terminated NWs are also relaxed using the OpenMX software package using the same parameters. [100] and [110] NW structures are fully optimized whereas we take a hollow-core approach (described in appendix C) for the [111] NW due to the larger number of atoms in the unit cell. Due to its reduced computational demand, Density Functional Tight Binding (DFTB) as implemented by the QuantumWise software package [26–28] is used to calculate the electronic transport properties of the 3 nm NWs, using a density mesh cutoff of 15 Hartree and an 11 k-point Monkhorst-Pack grid. DFTB results were compared to DFT in a carefully chosen set of cases in order to explicitly assess their validity in NW structures.

The electrical properties of these NWs are modeled in the context of the Landauer-Büttiker formalism, [29, 30] which includes the concepts of wide *reflectionless* contacts and electrodes. This formalism relates the electric current through a NW attached to two electron reservoirs (contacts) with the probability that an electron can be transmitted via the relation

$$I = \frac{e}{h} \sum_{\sigma} \int T_{\sigma}(E, V) \left[f\left(E, \mu_R, \ T_R\right) - f\left(E, \mu_L, T_L\right) \right] dE \,, \tag{3.1}$$

where e is the electron charge, h Planck's constant, $T_{\sigma}(E, V)$ is the transmission coefficient per spin channel σ at energy E and applied bias V, f is the

Fermi-Dirac distribution, T_L (T_R) and μ_L (μ_R) are the temperature and chemical potential of the left (right) electrode, and the applied bias is given by

$$V = \frac{\mu_R - \mu_L}{e}. \tag{3.2}$$

In the case of a NW directly attached to identical electron reservoirs (i.e., same chemical potential and temperature) we may write the linear response conductance in the zero-temperature limit as

$$G = \frac{I}{V} = \frac{e^2}{h} \sum_{\sigma} T_{\sigma}(E_F, V = 0). \tag{3.3}$$

Given that the NW is modeled as a perfectly periodic structure, all Bloch waves propagate with unit probability. This leads to the expression for the NW's intrinsic resistance as limited by its electronic structure (referred to as *contact resistance* in the literature [30])

$$G_C^{-1}(E_F) = \left[\frac{e^2}{h} \sum_i T_i M_i \right]^{-1}_{T_i=1;E=E_F} = \left[\frac{e^2}{h} M(E_F) \right]^{-1}, \tag{3.4}$$

where the NW acts as a ballistic waveguide for the total number of modes at the Fermi level $M(E_F)$, which includes all Bloch waves $\psi_{k\sigma}(E_F)$. This quantity provides information on the electrical resistivity intrinsic to the NW's electronic structure. Throughout this work the reported transmission then corresponds to a sum over the total number of modes $M(E)$ for each structure as a measure of their maximum potential conductivity as affected by their reduced scale and in the absence of scattering sources such as structural defects, grain boundaries, and phonons. Even though surface scattering is expected to be the most important contribution to resistance at these dimensions at zero temperature, the contribution of electron-phonon scattering at finite temperatures cannot be neglected. Plombon *et al.* report a decomposition of the resistance of copper lines with widths ranging from 75 to 500 nm with electron-phonon scattering estimated to account for 60% of the resistivity at 300K [6]. The effects of electron-phonon interactions on resistivity in sub 5 nm copper NWs are currently unknown and have been excluded from this study.

It is worth noting that for interconnect applications these NWs' function would be to provide electrical contact between devices (e.g., transistors) across a short length and with small voltage drops - ideally zero. Hence the use of the linear

response conductance applies and its validity can be extended to arbitrarily high temperatures as long as the transmission coefficient remains approximately constant over the energy range in which the transport takes place.

With the aim of providing some insight into the influence of the local chemical environment on electronic transport, a decomposition of transmission into spatially resolved pathways is computed according to the formalism described by Solomon *et al.* [19], as implemented in the QuantumWise software package, in which the transmission through a plane perpendicular to the transport direction that divides the system in two regions A and B is decomposed as

$$T(E) = \sum_{i \in A, j \in B} T_{ij}(E), \tag{3.5}$$

where i and j are atoms on each side of said plane. We note that the use of a Green's function implementation to the Landauer approach is required for decomposing the transmission into local contributions between pairs of atoms and hence this approach is taken for computing all electronic transport properties.

3.4 Results and Discussion

3.4.1 Nanowire structures

The optimized cell parameters along the periodic direction of the NWs for a single repeat unit are given in Table 3.1. In the case of the unterminated NWs, the optimized cell parameter is very similar to the calculated bulk cell parameter; this agreement is reflected in the NW structures wherein the atoms move only slightly from their bulk positions after geometry optimization [see Fig. 3.1]. When oxygen atoms are placed on the NW surface the situation changes dramatically with significant surface reconstruction seen for both the 1 nm and 3 nm NWs. There is a strong tendency for O to pull surface Cu atoms away from the NW bulk-like core until the bonded Cu and O atoms lie in a single plane. In bulk Cu(I) and Cu(II) oxide, each Cu bonds to 2 or 4 O atoms for Cu_2O and CuO respectively, conversely each O atom bonds to 4 or 2 Cu atoms for Cu_2O and CuO, respectively. The surface reconstruction seen in this work emulates the kinds of structural motifs seen in these oxides. The ratio of copper to oxygen (Cu:O) at the NW surface is 1.5, 1.7, and 1.9 for the 1 nm oxidized

Table 3.1: Optimized cell parameter in Å along the NWs' periodic direction. Unterminated NWs have cell parameter comparable to the calculated bulk value, while terminated NWs have a longer cell parameter.

		Unterminated		O-terminated	
	Bulk	1 nm	3 nm	1nm	3nm
[100]	3.63	3.60	3.63	3.75	3.64
[110]	2.57	2.56	2.59	2.86	2.73
[111]	6.29	6.26	-	6.46	-

[100], [110], and [111] NWs respectively, i.e., it lies between bulk CuO and bulk Cu_2O. In all cases, each O atom at the surface bonds to 3 Cu, thus the oxidation is intermediate to the situation seen for the bulk oxides. The surface oxide in the NWs consists of a very thin curved layer which locally is essentially two dimensional. Thus the NW surfaces are well oxidized as the Cu:O ratio is comparable to bulk copper oxide. For the [100] and [110] NWs, each Cu at the surface bonds to 2 oxygen atoms. Thus while the Cu:O ratio at the surfaces are different, in the case of [100] and [110] NWs, each O bonds to the same number of Cu atoms and each Cu bonds to the same number of O atoms. In spite of the similarity in the surface environment the surface geometries differ. For [100] the O-Cu-O motif is linear at Cu, while for [110] most O-Cu-O are V-shaped, a minority are linear. The [111] NW surface has 13 Cu atoms bonded each to 2 O atoms and 8 Cu atoms bonded each to 1 O atom, thus in line with the higher Cu:O ratio, this surface appears to be less oxidized than the [100] and [110] surfaces. The Cu atoms at the [111] surface which bond to two O have a mix of linear and V-shaped O-Cu-O structural arrangements.

The surface reconstruction does not strongly affect the positions of Cu atoms below the surface layers, this is clearly evident in the 3 nm NW structures shown in Fig. 3.2, beyond the first two Cu surface layers the Cu atoms occupy approximately equivalent configurations with respect to their bulk positions. The reconstruction at the surface is associated with a lengthening of the optimized cell parameter relative to the bulk and unterminated NWs, which is more severe for the 1 nm NWs than 3 nm NWs. This suggests that there is competition between the surface of the NW and core over the relaxed cell parameter along the axis. The oxidized surface favors an increase in length along this axis, presumably to better incorporate the surface O atoms in a layer. Conversely the core of the NW consists only of Cu atoms with their geometry similar to bulk fcc Cu and therefore favors a bulk-like cell parameter. Thus while unterminа-

Table 3.2: Calculated transmission per unit area for unterminated and oxidized 1 nm and 3 nm NWs. The area of each NW is the area of a circle, ellipse, or octagon with dimensions equal to the sum of the maximum cross-sectional inter-nuclear distances and twice the Cu atomic radius.

		Unterminated		O-terminated	
	Bulk	1 nm	3 nm	1nm	3nm
[100]	28.0	22.8	19.4	7.3	8.8
[110]	29.7	26.7	24.3	15.3	15.1
[111]	27.9	15.3	11.8	3.7	4.0

ted NW cell lengths are similar for 1 and 3 nm NWs, the oxidized 3 nm NWs have a smaller (i.e., closer to the bulk value) cell parameter than the oxidized 1 nm NWs. A concomitant increase in NW diameter is not observed, therefore this change in cell parameter occurs exclusively along the NW axis. The surface structural rearrangement seen here for the O-terminated [100] NW, shown in Fig. 3.1(d) and Fig. 3.2(b), is very similar to that seen in experiment for surface oxidized Cu(100) slabs [31] suggesting the structural rearrangement we see for the NWs in our simulations is representative of experimental structures with highly prepared surface treatments.

3.4.2 Electron transmission

The transmission spectra calculated for the terminated and oxidized 1 nm and 3 nm Cu NWs are shown in Fig. 3.3 for a narrow energy range of $\pm$50 meV centered about the Fermi energy. In each case, we find that the oxidized NW has a substantially lower electron transmission than the corresponding unterminated NW. This result is consistent with the increase in resistance after chemical oxidation previously been reported by Chawla *et al.* for Cu thin films and arises from the reduction of the DOS at the surface upon oxidation. [15] Additionally, we find a strong dependence of transmission on NW orientation. In all cases we find that the [110] NW has a larger transmission than [100], which in turn has a larger transmission than [111], irrespective of termination. As expected the transmission of the NWs increases going from 1 nm to 3 nm diameter due to the increasing cross-sectional area. The cross-sectional areas of the NWs are not identical as diameters deviate from exactly 1 nm and 3 nm due to the different atomic arrangements of the crystal orientations. Thus, we also calculate the transmission per unit area τ, presented in Table 3.2, to ensure that this variation in transmission with orientation is not due to deviations in cross sectional area.

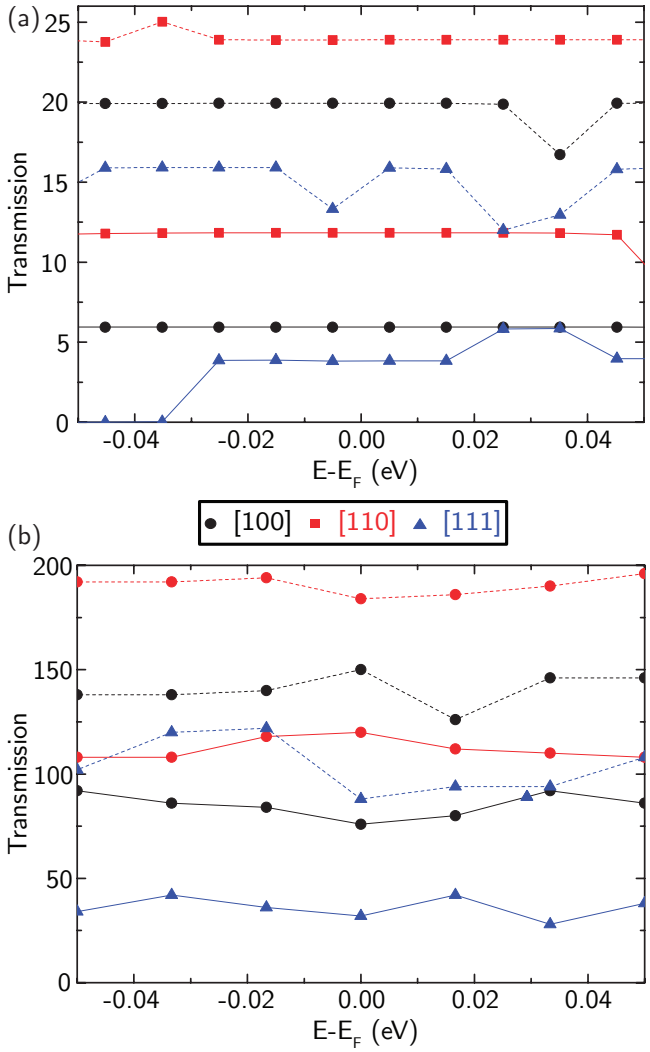

Figure 3.3: Transmission for (a) 1 nm and (b) 3 nm Cu NWs. Unterminated NWs (dashed lines) have a larger transmission than oxidized NWs (full lines) irrespective of diameter or crystal orientation. Transmission is strongly influenced by crystal orientation, with [110] NWs exhibiting larger transmission than [100] and [111] NWs. The zero of energy is taken to be at the Fermi level.

There is ambiguity in how to define the cross sectional area of the NWs due to atomic structure. The atoms in the NW have volume which extends beyond the nuclear positions and the smaller the NW the greater this contribution will be to the NW cross section. For simplicity we have taken the cross-section to be circular, elliptical, or octagonal as appropriate, with dimensions equal to the maximum inter-nuclear width of the NW plus twice the Cu atomic radius (1.28 Å). We find that the transmission per area τ follows the same trend as the total transmission plotted in Fig. 3.3; [110] has the largest τ and [111] the smallest, regardless of diameter or termination. This result is consistent with the anisotropy in Cu conductivity with crystal orientation reported recently by

Hegde *et al.* [18]. In fact, this orientation dependence is of such significance that for the 3 nm NWs the *oxidized* [110] NW has a transmission comparable to the *unterminated* [111] NW at the Fermi energy; a remarkable result consistent with the shape of the Fermi surface of bulk fcc copper, in which the Fermi surface exhibits a vanishing DOS along the $\langle 111 \rangle$ directions. The extent of the orientation dependence on transmission is also clearly evident in Table 3.2. In the case of unterminated NWs, the transmission for a given cross sectional area for [110] is approximately twice that of [111] NWs, after oxidation this margin further increases with the [110] transmission per unit area approximately 3.5 times larger than for the [111] NW. It may be anticipated that a more oxidized NW would show greater suppression in transmission, however the 1 nm [111] NW is in fact less oxidized than the [110] NW; each surface Cu in the [110] NW bonds to 2 oxygen atoms while surface [111] atoms bond to either 1 or 2 oxygen atoms. Meanwhile, unterminated [100] and [110] NWs show similar transmission per unit area; [100] is about 4 units smaller than [110] for both 1 nm and 3 nm NWs. After oxidation, the transmission per unit area for [100] NWs is approximately 60% of [110] NWs, i.e., transmission suppression on oxidation is relatively larger for [100] than [110]. Thus both the surface chemical environment and the NW orientation play a critical role in determining the overall transmission of the copper NW.

3.4.3 Local transmission paths

The transmission results show that orientation and surface environment drastically impact on Cu NW electron transport. These effects are not easy to decouple, however, a greater understanding of the relationship between them can be established by examining transmission through the NW at an atomic scale. We have calculated transmission pathways in the NWs [19] at the Fermi level, which are shown in Fig. 3.4 for the unterminated [111] NW, to particularly elucidate the effects of NW crystal orientation and surface oxidation on transmission. Transmission pathways provide a visual representation of transmission through the NW with the arrow width representing the magnitude of the transmission between an atom pair. As described in the caption of Fig. 3.4, the arrows are colored according to their angle with respect to the NW axis; blue arrows correspond to forward transmission, green arrows to radial transmission (i.e., atoms within the same transverse plane), and red arrows backscattering or reflection. As expressed in Eq. (3.5), the transmission pathways crossing

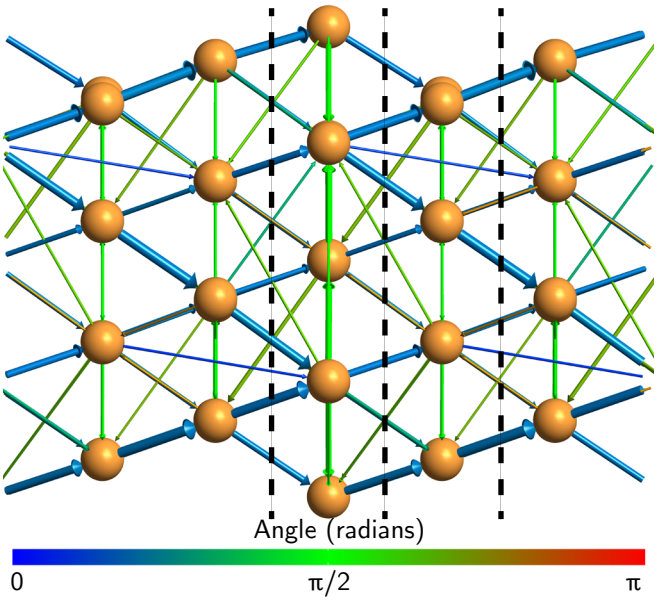

Figure 3.4: Transmission pathways at the Fermi energy for unterminated 1 nm [111] Cu NW. The arrows show the direction of transmission paths. The arrow thickness represents the magnitude of the transmission while the color represents the orientation of the path with respect to the NW axis. Forward transmission is shown in blue, radial transmission in green, and backscattering in red. Pathways with transmission below 10% of the maximum value are omitted for clarity. The dashed black lines mark the positions of the planes shown Fig. 3.5(e).

a given plane perpendicular to the transport direction always sum to give the total transmission coefficient.

A more convenient visual representation is portrayed in Fig. 3.5 in which the intersections of transmission pathways with planes located halfway between non-equivalent atomic planes give a clear image of the decomposition of the total transmission into pathways per cross-sectional area per NW. Such planes are indicated by dashed black lines in Fig. 3.4 for the case of the unterminated [111] NW. These projections provide a heuristic representation of localized transmission and allow quick identification of where the most important contributions lie within the NW cross-section.

Fig. 3.5(a) shows transmission pathways for the unterminated [100] NW. There are transmission pathways both parallel ('dots' centered at atomic positions) and angled to the NW axis (centered between atomic positions). Angled pathways are larger in magnitude than parallel pathways as represented by their larger 'dot' diameter and their color. This difference in magnitude can be attributed to the distance between the Cu atoms being larger if a direct route

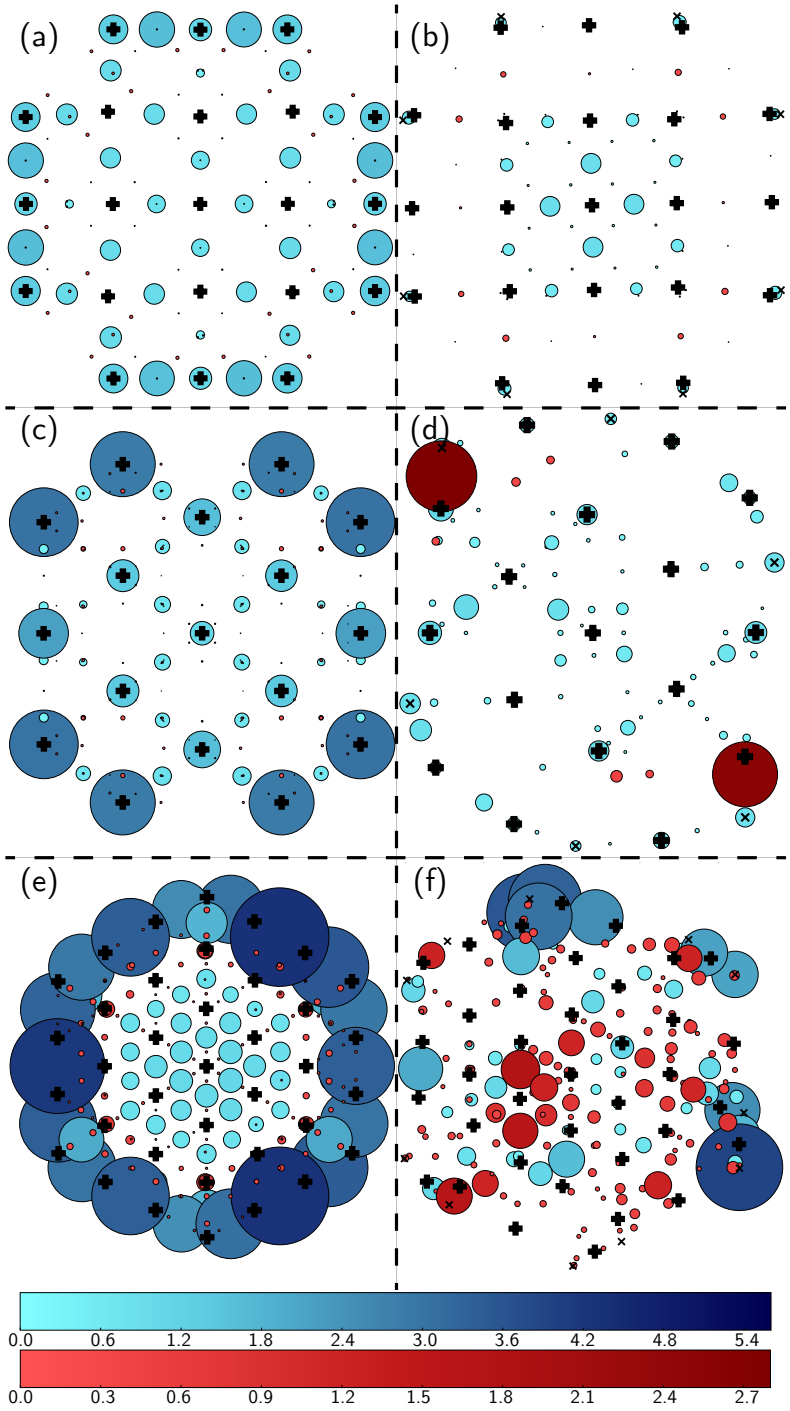

Figure 3.5: Cross-section view of the transmission pathways at the Fermi energy. (a) Unterminated [100], (b) O-terminated [100], (c) Unterminated [110], (d) O-terminated [110], (e) Unterminated [111] and (f) O-terminated [111]. Atomic positions are shown as "+" (Cu) or "x" (O). The 'dot' size represents the absolute magnitude of the transmission pathway crossing the plane, while the 'dot' color indicates the magnitude and direction of the transmission pathway. Blue 'dots' correspond to forward transmission and red 'dots' to backscattering. Note the difference in the color scales ranges.

parallel to the axis is taken (3.60 Å versus 2.53 Å). It is is readily seen that pathways along the surface dominate electron transmission for this NW as the 'dots' in the surface are larger and darker than below the surface, where the parallel pathways are smaller and obscured by the symbols indicating the atomic positions.

The unterminated [110] NW transmission pathways are shown in Fig. 3.5(c). Transmission involving only surface atoms occurs along the NW axis and is large (indicated by the darker blue 'dots' centered about atomic positions) while pathways at an angle to the axis exhibit much lower transmission. Below the surface the situation is similar, transmission along the axis is larger than off-axis. In this orientation the Cu atom separation is similar for both parallel and off axis transmission and thus the more direct parallel route is favored. As for the unterminated [100] NW, transmission is larger at the NW surface than below the surface with the largest 'dots' corresponding to pathways located at the surface and parallel to the NW axis. The transmission pathways for the unterminated [111] NW, shown in Fig. 3.5(e). In this case, there is no significant transmission directly parallel to the NW axis, this is presumably because the Cu interatomic distance along the NW axis is simply too large compared to the off axis distances (6.26 Å versus $\sim$2.5 Å reflecting that no nearest neighbors align along the NW axis). As previously mentioned, this result is consistent with the vanishing density of states found along the $\langle 111 \rangle$ directions in the Fermi surface of fcc Cu; there are no transmission paths parallel to the [111] direction as shown by the absence of arrows parallel to the NW axis in Fig. 3.4 and of 'dots' centered about atomic positions in Fig. 3.5(e). As shown in Fig. 3.4 transmission pathways tend to flow along the NW surface until they reach a Cu atom with a low coordination number (such as the one at the top center of the figure), at which point the electrons are scattered into the NW core where they continue to propagate along angled paths until they reach another surface where this process repeats. The lack of transmission pathways parallel to the [111] NW axis makes the surface critical as all paths inevitably lead to the surface. While there are some transmission pathways inside the core of the NW, transmission *through* the NW occurs primarily at the NW surface; and much like the unterminated [100] and [110] NWs, transmission is larger at the surface. However, in this case as well as 'dots' representing forward transmission, the 'dots' representing negative values (i.e., electron backscattering or reflection paths) are much larger than for the unterminated [100] and [110] NWs.

The transmission pathways of the unterminated NWs consistently show that

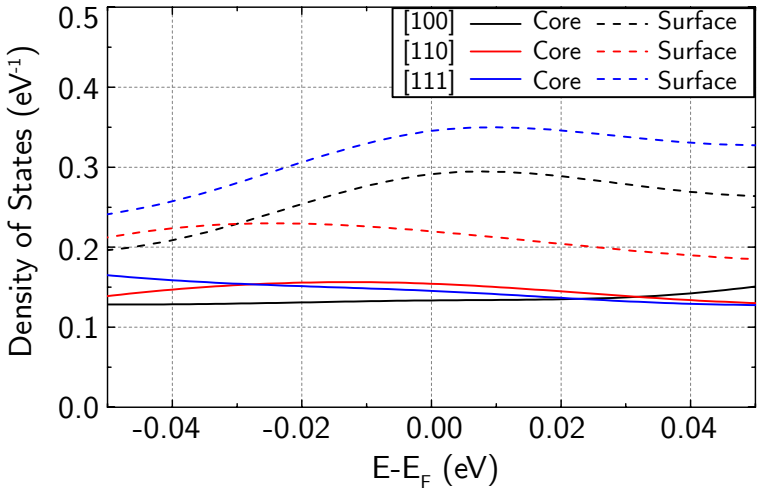

Figure 3.6: Average local density of states for an atom at the surface (dashed) and at the center (solid) of unterminated 1 nm NWs. The zero of energy is taken to be at the Fermi level.

transmission is larger at the NW surface than in the core and also that backscattering for these NWs is relatively small, particularly for the [100] and [110] NWs in which the total magnitude of all reflecting paths is 14% and 13% of that of forward paths, whereas for [111] NWs this value increases to 25%. This surface-dominated transmission can be explained in terms of the increased local density of states (LDOS) of surface atoms at the Fermi level as a result of their low coordination. This allows electrons otherwise localized at bonds to become available for transmission at the surface atoms. Fig. 3.6 shows the average local density of states (LDOS) of an atom situated at the surface and of an atom close to the center of the NWs' cross section; the atoms at the surface show a larger density of states in the range around the Fermi level studied in this work. Unterminated [111] NWs exhibit the largest boost with the average LDOS value of a surface atom being 2.55 times that of an atom near the center of the NW at the Fermi level; similarly, atoms at the surface of [100] NWs have an average surface-to-center LDOS ratio of 2.41 and a considerably lower ratio of 1.39 is found for [110] NWs.

As might be expected from the transmission spectra shown in Fig. 3.3 and the previous analysis, oxidation of the NWs changes the behavior at the NW surfaces considerably. In the [100] NW, transmission at and just below the NW surface is reduced upon oxidation, in fact Fig. 3.5(b) shows that near the surface forward transmission is largely suppressed and backscattering pathways are enhanced. In the core of the NW the transmission is similar to the unterminated NW as shown by similarly arranged, sized and colored 'dots'. Thus in the

case of the [100] NW, oxidation appears to affect the surface and immediate subsurface almost exclusively. In the case of the [110] NW, more significant back scattering is seen upon surface oxidation with the appearance of the large red 'dots' indicating a relatively large magnitude in Fig. 3.5(d). Unlike the [100] NW, transmission is also reduced in the core of the [110] NW upon surface oxidation. A suppression of the pathways parallel to the NW axis can be clearly seen all the way to the center when comparing to the unterminated NW (Fig. 3.5(c)). Thus it appears that the effect of surface oxidation is felt deeper in the NW for the [110] orientation compared to [100]. However, transmission per unit area for the oxidized [100] NW actually drops more relative to the unterminated NW compared to the [110] orientation, as reported in Table 3.2. This is likely caused by a reduction of transmission at the surface and immediate subsurface in the [100] oxidized NW, in which the surface has a larger contribution relative to the core in the unterminated case as shown in Fig. 3.6 and discussed above. The surface of the oxidized [111] NW is more disordered than the oxidized [100] and [110] NWs studied in this work. This disorder along with the indirect transmission associated with transport along this crystal orientation leads to complicated, disordered transmission pathways (Fig. 3.5(f)) consistent with the low transmission calculated for this structure. In contrast to the [100] and [110] oxidized NWs, there is large forward transmission at the surface for the oxidized [111] NW, which can be seen clearly in the mapping of the transmission pathways onto a cross sectional area of the [111] NW shown in Fig. 3.5(f). However, the large backscattering paths in the core of the NW result in a lower overall transmission; all paths in the core lead either to the surface (where oxidation has largely suppressed forward transmission) or are backscattered.

3.4.4 Transmission model

To understand the behavior of the total transmission per NW given in the previous sections, we provide an analysis for a simple model describing the electron transmission behavior of round NWs which partitions the NWs into regions of similar behavior based on the magnitudes of the transmission pathways within the them. The generalization of the model to other geometries is straightforward. The model provides insight into the observation that transmission per unit area decreases as area increases for the unterminated NWs and that the transmission per unit area is relatively constant for oxidized NWs for a given

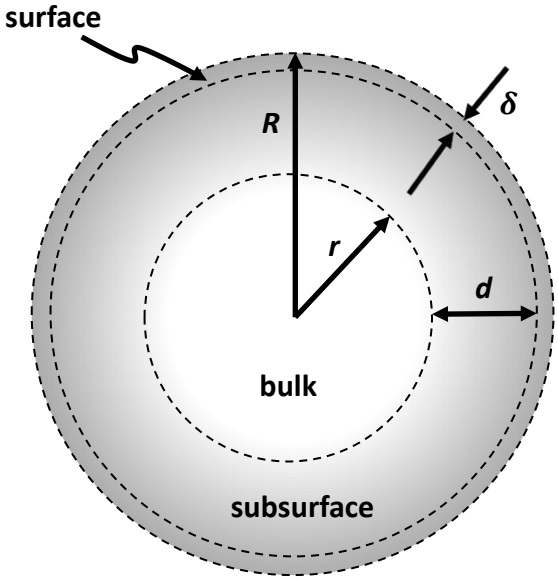

Figure 3.7: Schematic representing the copper NW model, with surface, sub surface and bulk regions indicated. R is the radius of the NW, r is the radius of the bulk region, d is the width of the subsurface region, i.e., the depth to which τ is affected by the surface, and δ is the width of the surface.

orientation.

The total transmission T of a round NW of radius R is divided into contributions from three distinct regions of the NW; the surface, the subsurface and the bulk regions; as shown in Fig. 3.7 for a cross section of the NW. The surface region is described by a thickness δ, the subsurface region by a thickness d and the bulk-like core is described by a radius r; therefore

$$R = r + d + \delta. \tag{3.6}$$

To each region is assigned a transmission per unit area τ. The surface transmission per unit area τ_{surf} is assumed constant, whereas the subsurface transmission per unit area τ_{sub} can vary with depth into the NW as signified by the grading in Fig. 3.7. However, it is assumed that an effective transmission per unit area can be assigned to the subsurface region. The bulk region is defined as the core atoms for which the transmission per unit area approaches the bulk behavior τ_{bulk}.

The area of the surface region can be expressed as

$$A^{surf} = \pi[R^2 - (R-\delta)^2] = (2\pi R)\delta - \pi\delta^2, \tag{3.7}$$

which for $R \gg \delta$ can be approximated as

$$A^{surf} \approx (2\pi R)\delta. \tag{3.8}$$

Similarly the area for the subsurface region can be expressed as

$$A^{sub} = \pi[(R-\delta)^2 - r^2] = 2\pi(R-\delta)d - \pi d^2, \tag{3.9}$$

which for $R \gg d + \delta$ is given as

$$A^{sub} \approx (2\pi R)d. \tag{3.10}$$

The core region displaying bulk-like behavior has an area given by

$$A^{bulk} = \pi r^2 = \pi(R - d - \delta)^2 \tag{3.11}$$

which for $R \gg d + \delta$ becomes

$$A^{bulk} \approx \pi R^2. \tag{3.12}$$

The fact that A^{surf} and A^{sub} scale linearly with R whereas A^{bulk} scales as R^2 for large values of R simply describes the fact that the surface and subsurface play decreasing roles as the NW's radius is increased. An effective transmission per unit area τ is then defined for each region and the total transmission is expressed as

$$T = A^{surf}\tau_{surf} + A^{sub}\tau_{sub} + A^{bulk}\tau_{bulk}. \tag{3.13}$$

To explore the role of the surface and subsurface transmission per unit area in small cross section NWs we consider four cases.

Case I: $R \approx \delta$. In this limit, the surface dominates and transport is given purely by the surface and represents, for example, the case of an atomic chain.

Case II: $R \approx d + \delta$. This condition describes when the cross sectional area of the NW is of a scale that a subsurface region is present but the NW diameter is not large enough for the core of the NW to display bulk behavior for transmission (it should be noted that the subsurface region is not sharply defined as represented by the grading of the gray region used to define it in Fig. 3.7). In the transmission plots of Fig. 3.5 for the unterminated Cu NWs, it can be seen that the subsurface region has a lower transmission per unit area compared to the NW surface regions. Hence by decreasing the NW diameter from 3 nm to 1 nm, a larger transmission per unit area is obtained consistent with the results listed in Table 3.2.

Case III: $r \approx d + \delta$. As the NW radius increases, eventually a core region is formed whereby local transmission pathways approach the values obtained in bulk copper. When this core region is of a comparable dimension to the surface and subsurface layer, the transmission per unit area will reflect the contributions from the different regions. As the subsurface region in unterminated Cu NWs has a lower transmission per unit area than the bulk, the overall transmission per unit area will increase relative to Case II as the region forms.

Case IV: $R \approx r$. As the NW's radius is further increased, the core region's contribution will quickly dominate due to the area increasing as R^2 as opposed to the linear dependence on NW radius for the surface and subsurface regions. Hence the transmission per unit area for the NW will increase with increasing R until asymptotically approaching the bulk value.

The following picture emerges in the case of unterminated NWs. For extremely small diameter NWs with diameters of approximately 1 nm, surface and subsurface transmissions combine to provide a transmission per unit area that is comparable to bulk copper for [100] and [110] and less than bulk copper for [111]. As the NW diameter increased, for example up to 3 nm, the lower subsurface transmission with respect to surface transmission results in a net lowering of overall transmission per unit area compared to smaller diameter NWs. As the NW diameter is increased further, the core region begins to behave like a bulk conductor and the transmission rises and asymptotically approaches the bulk transmission per unit area.

The picture needs to be slightly modified for the case of NWs with surface oxidation. As seen in Fig. 3.5, the surface transmission is reduced significantly due to surface oxidation. From Table 3.2, it is seen that the transmission per unit area for the 1 nm and 3 nm diameter NWs are comparable. Once oxidi-

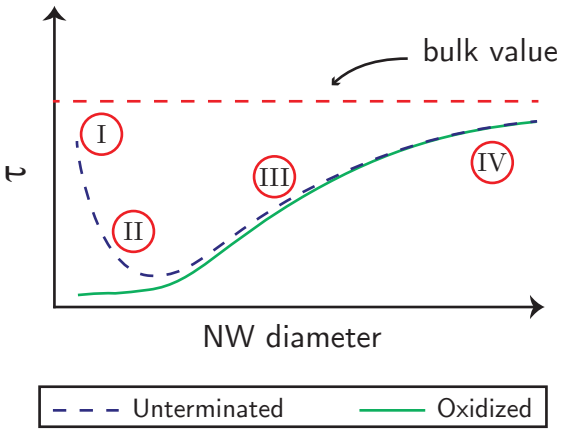

Figure 3.8: Schematic representing the evolution of transmission per unit area with increasing nanowire diameter for the case of unterminated (dashed, blue) and oxidized (green, solid) copper NWs. *Cases* discussed in the text corresponding to different size regimes are indicated along the curves.

zed, the transmission at the surface is suppressed and the transmission of the subsurface region dominates. We anticipate that the transmission per unit area of the subsurface region for a given orientation is similar for 1 nm and 3 nm NWs and this combined with the low surface transmission [see Fig. 3.5] leads to the transmission per unit area for each orientation being approximately constant going from 1 nm to 3 nm diameter, as reported in Table 3.2. However, the transmissions of both 1 nm and 3 nm oxidized NWs are much lower than found for the bulk, and hence larger cross section NWs are required before significant bulk-like behavior from the core contributes to the net transmission per unit area. A schematic representation of the evolution of total transmission per unit area values with NW diameter for both unterminated and oxidized structures is shown in fig. 3.8.

3.5 Conclusion

The electron transport properties of 1 nm and 3 nm diameter copper NWs have been calculated in each case for unterminated and surface oxidized NWs of [100], [110] and [111] crystal orientations. We find even 1 nm diameter copper NWs to be metallic, however electron transmission is strongly dependent on both surface termination and crystal orientation. Surface oxidation suppresses electron transmission compared to unterminated copper NWs, consistent with previous reports for copper thin films. The [110] oriented NWs consistently

show a higher electron transmission than [100] oriented NWs which in turn have a higher electron transmission than [111] NWs. Transmission in unterminated copper NWs is larger at the NW surface than below the surface, irrespective of crystal orientation. A different picture emerges for surface oxidized NWs wherein transmission is lower at the NW surface than in the subsurface for [100] and [110] oriented NWs. However while the oxidized [111] NW surface transmission is reduced compared to the unterminated NW, it nonetheless continues to show larger surface transmission than subsurface transmission. Transmission per unit area decreases with increasing diameter for unterminated NWs but remains approximately constant for the surface oxidized NWs studied. A simple model of transmission in round NWs which divides the NW into regions based on local transmission pathways explains the differing behaviors of unterminated and oxidized NWs. Briefly, transmission per unit area is lower in the subsurface region than at the surface for the unterminated NWs studied, thus when the diameter is increased from 1 nm to 3 nm the transmission per unit area of the NW decreases as the subsurface region becomes relatively more important. In oxidized NWs, the overall transmission per unit area is comparable for 1 nm and 3 nm NWs. The suppression of the surface transmission in this case increases the contribution of the subsurface to overall transmission and a similar subsurface transmission per unit area may be expected for 1 nm and 3 nm oxidized NWs for the same crystal orientation resulting in similar overall transmission per unit area. Overall, our results suggest that conductivity in sub 3 nm copper NWs is highly sensitive to crystal orientation and surface termination, and that careful material preparation and processing will be essential in order to maximize conductivity.

3.6 Acknowledgments

This work was performed as part of the Intel-Tyndall research collaboration sponsored by Intel Components Research. ASS was funded under an Irish Research Council postgraduate scholarship. We are grateful to QuantumWise A/S for providing access to the QuantumWise simulation software.

References

[1] International technology roadmap for semiconductors. *http://www.itrs2.net/itrs-reports.html (accessed August 2016)*.

[2] Werner Steinhögl, Günther Schindler, Gernot Steinlesberger, and Manfred Engelhardt. Size-dependent resistivity of metallic wires in the mesoscopic range. *Phys. Rev. B*, 66:075414, 2002.

[3] W. Zhang, S. H. Brongersma, Z. Li, D. Li, O. Richard, and K. Maex. Analysis of the size effect in electroplated fine copper wires and a realistic assessment to model copper resistivity. *J. Appl. Phys.*, 101(6):063703, 2007.

[4] K. Fuchs. The conductivity of thin metallic films according to the electron theory of metals. *Math. Proc. Cambridge Philos. Soc.*, 34:100–108, 1938.

[5] A. F. Mayadas and M. Shatzkes. Electrical-resistivity model for polycrystalline films: The case of arbitrary reflection at external surfaces. *Phys. Rev. B*, 1:1382–1389, 1970.

[6] J. J. Plombon, Ebrahim Andideh, Valery M. Dubin, and Jose Maiz. Influence of phonon, geometry, impurity, and grain size on copper line resistivity. *Appl. Phys. Lett.*, 89(11):113124, 2006.

[7] Daniel Josell, Sywert H. Brongersma, and Zsolt Tokei. Size-dependent resistivity in nanoscale interconnects. *Annu. Rev. Mater. Res.*, 39:231–254, 2009.

[8] Ricardo Henriquez, Simon Cancino, Andres Espinosa, Marcos Flores, Thomas Hoffmann, German Kremer, Judit G. Lisoni, Luis Moraga, Roberto Morales, Simon Oyarzun, Marco Antonio Suarez, Alejandro Zúñiga, and Raul C. Munoz. Electron grain boundary scattering and the resistivity of nanometric metallic structures. *Phys. Rev. B*, 82:113409, 2010.

[9] Ricardo Henriquez, Marcos Flores, Luis Moraga, German Kremer, Claudio González-Fuentes, and Raul C. Munoz. Electron scattering at surfaces and grain boundaries in thin Au films. *Appl. Surf. Sci.*, 273(0):315 – 323, 2013.

[10] Tik Sun, Bo Yao, Andrew P. Warren, Katayun Barmak, Michael F. Toney, Robert E. Peale, and Kevin R. Coffey. Dominant role of grain boundary scattering in the resistivity of nanometric Cu films. *Phys. Rev. B*, 79:041402, 2009.

[11] Tik Sun, Bo Yao, Andrew P. Warren, Katayun Barmak, Michael F. Toney, Robert E. Peale, and Kevin R. Coffey. Surface and grain-boundary scattering in nanometric Cu films. *Phys. Rev. B*, 81:155454, 2010.

[12] R. L. Graham, G. B. Alers, T. Mountsier, N. Shamma, S. Dhuey, S. Cabrini, R. H. Geiss, D. T. Read, and S. Peddeti. Resistivity dominated by surface scattering in sub-50 nm Cu wires. *Appl. Phys. Lett.*, 96(4):042116, 2010.

[13] Pei-I Wang, Michael D. Frey, Morris Washington, Saroj Nayak, and Toh-Ming Lu. Resistivity of sub-50 nm copper lines epitaxially grown on Si(100) substrate. *Thin Solid Films*, 520(19):6106 – 6108, 2012.

[14] J. S. Chawla and D. Gall. Specular electron scattering at single-crystal Cu(001) surfaces. *Appl. Phys. Lett.*, 94(25):252101, 2009.

[15] J. S. Chawla, F. Zahid, H. Guo, and D. Gall. Effect of O_2 adsorption on electron scattering at Cu(001) surfaces. *Appl. Phys. Lett.*, 97(13):132106, 2010.

[16] J. S. Chawla, F. Gstrein, K. P. O'Brien, J. S. Clarke, and D. Gall. Electron scattering at surfaces and grain boundaries in Cu thin films and wires. *Phys. Rev. B*, 84:235423, 2011.

[17] Ferdows Zahid, Youqi Ke, Daniel Gall, and Hong Guo. Resistivity of thin Cu films coated with Ta, Ti, Ru, Al, and Pd barrier layers from first principles. *Phys. Rev. B*, 81:045406, 2010.

[18] Ganesh Hegde, Michael Povolotskyi, Tillmann Kubis, James Charles, and Gerhard Klimeck. An environment-dependent semi-empirical tight binding model suitable for electron transport in bulk metals, metal alloys, metallic interfaces, and metallic nanostructures. II. application—effect of quantum confinement and homogeneous strain on Cu conductance. *J. Appl. Phys.*, 115(12):123704, 2014.

[19] G.C. Solomon, C. Herrmann, T. Hansen, V. Mujica, and M.A. Ratner. Exploring local currents in molecular junctions. *Nat. Chem.*, 2:223, 2010.

[20] OPENMX software package. *www.openmx-square.org (accessed August 2016)*.

[21] J.P. Perdew, K. Burke, and M. Ernzerhof. Generalized gradient approximation made simple. *Phys. Rev. Lett.*, 77:3865–3868, 1996.

[22] I. Morrison, D.M. Bylander, and L. Kleinman. Non-local Hermitian norm-conserving Vanderbilt pseudopotenial. *Phys. Rev. B*, 47:6728–6731, 1993.

[23] T. Ozaki. Variationally optimized atomic orbitals for large-scale electronic structures. *Phys. Rev. B*, 67:155108, 2003.

[24] T. Ozaki and H. Kino. Numerical atomic basis orbitals from H to Kr. *Phys. Rev. B*, 69:195113, 2004.

[25] Hendrik J. Monkhorst and James D. Pack. Special points for Brillouin-zone integrations. *Phys. Rev. B*, 13:5188–5192, 1976.

[26] Atomistix ToolKit version 2015-1 QuantumWise A/S. *www.quantumwise.com (accessed August 2016)*.

[27] Mads Brandbyge, José-Luis Mozos, Pablo Ordejón, Jeremy Taylor, and Kurt Stokbro. Density-functional method for nonequilibrium electron transport. *Phys. Rev. B*, 65:165401, 2002.

[28] José M Soler, Emilio Artacho, Julian D Gale, Alberto Garcia, Javier Junquera, Pablo Ordejon, and Daniel Sanchez-Portal. The SIESTA method for ab initio order-N materials simulation. *J. Phys.: Condens. Matter*, 14(11):2745, 2002.

[29] R. Landauer. Spatial variation of currents and fields due to localized scatterers in metallic conduction. *IBM J. Res. Dev.*, 1(3):223–231, 1957.

[30] Supriyo Datta. *Electronic transport in mesoscopic systems*. Cambridge University Press, Cambridge CB2 8BS, United Kingdom, 1995.

[31] Mehmet Z. Baykara, Milica Todorović, Harry Mönig, Todd C. Schwendemann, Özhan Ünverdi, Lucia Rodrigo, Eric I. Altman, Rubén Pérez, and Udo D. Schwarz. Atom-specific forces and defect identification on surface-oxidized Cu(100) with combined 3D-AFM and STM measurements. *Phys. Rev. B*, 87:155414, 2013.

Chapter 4

Electronic structure tuning via surface modification in semimetallic nanowires

4.1 Abstract

Electronic structure properties of nanowires (NWs) with diameters of 1.5 nm and 3 nm based on semimetallic α-Sn are investigated by employing density functional theory and perturbative GW methods. We explore the dependence of electron affinity, band structure and band gap values with crystallographic orientation, NW cross-sectional size, and surface passivants of varying electronegativity. We consider four chemical terminations in our study: methyl (CH_3), hydrogen (H), hydroxyl (OH), and fluorine (F). Results suggest a high degree of elasticity of Sn-Sn bonds within the SnNWs' cores with no significant structural variations for nanowires with different surface passivants. Direct band gaps at Brillouin zone centers are found for most structures studied with quasiparticle corrected band gap magnitudes ranging from 0.25 eV to 3.54 eV in 1.5 nm diameter structures, indicating an exceptional range of properties for semimetal NWs below the semimetal-to-semiconductor transition. Band gap variations induced by changes in surface passivants indicate the possibility of realizing semimetal-semiconductor interfaces in NWs with constant cross-section and crystallographic orientation, allowing the design of novel dopant-free NW-based electronic devices.

4.2 Introduction

The nanopatterning of solids has been shown to induce significant variations in material properties with respect to their bulk counterparts as a result of quantum confinement effects and an increase in the impact of surface phenomena on the system as a whole due to their large surface-to-volume ratios. Tuning of a broad range of properties has been successfully demonstrated and the design of novel nanostructures exploiting chemical and structural modifications have allowed elucidation of numerous applications such as chemical sensors, [1, 2] transparent electronics, [3] and tunnel field-effect transistors (FETs) [4, 5], making exploitation of size effects a way of enhancing a material's versatility by allowing some degree of tunability of its properties through geometric effects.

The study of semiconductor nanowire (NW) structures has been increasing since Wagner and Ellis [6] first proposed the vapor-solid-liquid growth mechanism and demonstrated submicron-scale wires of semiconducting materials five decades ago. More recently, with advances in nanofabrication, NWs with diameters as low as 1 nm have been experimentally realized [7] and their measured band gaps reproduced by GW-corrected density functional theory (DFT) calculations. [8, 9] Analogous to band gap *widening* observed in semiconductors, bulk semimetals' electronic properties have been reported to transition to those of a semiconductor with the emergence of a band gap for structures with critical dimensions on the order of 10 nm. As a result of quantum confinement, band gaps with magnitudes greater than 1 eV have been predicted in α-Sn NWs with diameters of approximately 1 nm. [10]

Further control of NW band gaps has been reported in silicon NWs by passivating surface states with chemical groups of varying electronegativities reported to induce band gap variations of the same order of magnitude as quantum confinement effects. Leu *et al.* [11] report variations of the order of electronvolts in SiNW band gaps when passivated with halogens with respect to hydrogen-passivated structures, attributing reductions in band gaps to weakly interacting surface species. Nolan *et al.* [12] studied band gap variations on similar systems passivated with H, $\mathrm{NH_2}$ and OH, and correlated band gap variations of up to 1 eV to orbital hybridization between passivants and NW core, while Zhuo and Chou [13] discuss such band gap reductions in SiNWs in terms of charge redistributions and the corresponding electrostatic effects induced by surface chemistry.

In the following, we explore the effects of surface passivants with varying electronegativity on NWs based on semimetallic α-Sn. Although not stable in bulk at room temperature [14], studies show Sn's α phase can be stabilized in thin film structures [15–18], while α-Sn nanocrystals have been the focus of recent studies for applications in lithium-ion batteries. [19–21] Due to its simple crystal structure, we study α-Sn as a test system for exploring the range of properties that can be obtained from the competing effects of quantum confinement and chemical passivation in sub-5-nm structures based on bulk semimetals. We study the evolution with NW size and crystallographic orientation by considering structures with diameters of approximately 1.5 nm and 3 nm grown along low index crystallographic orientations. NW structures have been reported to exhibit electron transport properties which makes them particularly suitable for applications in electronics [22], and, in particular, α-Sn NWs have been previously proposed for the design of novel nanoelectronic devices [10]; Therefore, we take a particular interest in the effects on energy band gaps –a key quantity for such applications. We improve upon the DFT description by means of a scheme based on the GW [23] approximation which has been shown to greatly improve the description of band gaps in semiconductors. [24, 25]

4.3 Method

Nanowire structures with cross-sectional areas corresponding to cylindrical structures with diameters of approximately 1.5 nm and 3 nm are modelled from bulk α-Sn's diamond structure (space group $\mathrm{Fd\bar{3}m}$, no. 227). NWs oriented along the $[100]$, $[110]$, and $[111]$ crystallographic orientations are considered with their surface bonds saturated by bonding to different surface terminating groups. Four different monovalent groups with varying degrees of electronegativity are chosen for the study of the effects of surface passivation: methyl ($-\mathrm{CH_3}$), hydrogen ($-\mathrm{H}$), hydroxyl ($-\mathrm{OH}$), and fluorine ($-\mathrm{F}$). Due to the large surface-to-volume ratio in these nanostructures, a significant proportion of the Sn atoms which constitute the NWs directly bond to the surface passivants, accounting for 40% to 44% of the chemical composition of the system as a whole in the 1.5 nm NWs, and approximately 26% to 27% in the 3 nm NWs depending on the crystallographic orientation of a given NW.

Density functional theory (DFT) [26–28] within the usual Kohn-Sham [29] framework is employed to simulate the electronic structure of these nanostructu-

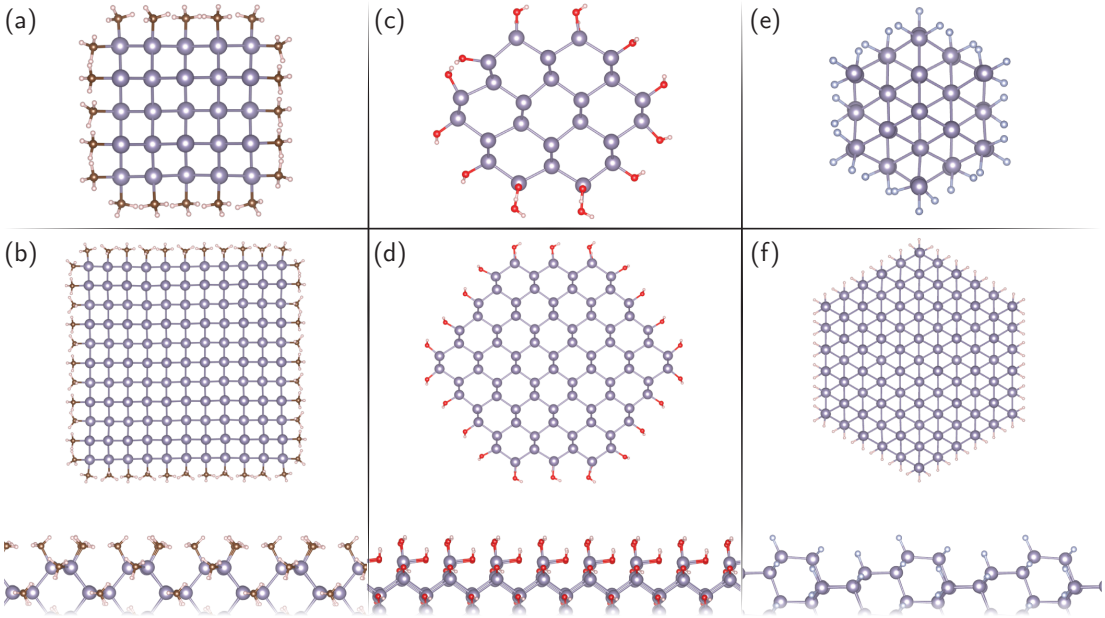

Figure 4.1: Atomistic illustrations of α-SnNW cross-sectional and side views of optimized NW structures of 1.5 nm (top row) and 3 nm (bottom row) diameters. (a),(b) $[100]$ $SnCH_3$, (c),(d) $[110]$ $SnOH$, and (e),(f) $[111]$ SnF. Sn is shown in purple, H in pink, O in red, C in brown, and F in blue.

res. We take the supercell approach for computing the properties of systems with reduced dimensionality by which at least 15 Å of vacuum is introduced along directions perpendicular to the NWs' axes in order to eliminate interactions with periodic images normal to the NWs' axes, leading to a simulation model for the NWs as infinitely long and perfectly crystalline quasi-1D systems. The Perdew-Burke-Ernzerhof (PBE) [30] formulation of the generalized gradient approximation (GGA) for the exchange and correlation functional is used in conjunction with norm-conserving pseudopotentials [31] and double-ζ-polarized basis sets of localized pseudo-atomic orbitals [32, 33]. Brillouin zone integrations are performed over a grid of k-points generated according to the Monkhorst-Pack [34] scheme with a density of approximately 25 k-points $\times$Å along a NW axis, whilst real-space quantities are discretized on a grid with corresponding energy cut-offs of 200 Ry (280 Ry) for NWs passivated with hydrogen and methyl (fluorine and hydroxyl). In this approximation, the equilibrium cell parameter and bulk modulus of α-Sn are predicted to be 6.70 Å and 38 GPa, respectively. This represents a 3% deviation from experimentally reported values of 6.49 Å in the equilibrium cell parameter [15,35], and a 30% underestimation of the bulk modulus with respect to experimentally reported values of 54 GPa [36, 37]. Atomic positions in the NWs are relaxed until forces acting on all atoms are below 10^{-2} eV/Å, and the total energy of the cell is minimized with

respect to its length along the NW axis. Figure 4.1 shows cross-sectional and side views of each NW orientation and size with varying surface terminations.

Given the well-known shortcomings of standard DFT in predicting electronic band gaps [25, 38, 39] – a key parameter for semiconductors with applications in electronics – we improve our description through a perturbative many-body approach. We perform first-order perturbative GW [23, 40, 41] quasi-particle corrections for 1.5 nm NWs to gain insight into the order of magnitude of energy band gaps induced as a result of quantum confinement. Electronic structure calculations based on plane-waves [42] and norm-conserving pseudopotentials [43] serve as starting point for computing first-order corrections within the quasiparticle (QP) approximation [44] as

$$E_{nk}^{QP} = E_{nk}^{KS} + Z_{nk}[\Sigma_{nk}(E_{nk}^{KS}) - V_{nk}^{XC}], \tag{4.1}$$

where E_{nk}^{KS} are the Kohn-Sham eigenvalues computed from the Kohn-Sham procedure, and Σ_{nk} represents the self-energy which includes exchange and correlation effects, calculated as the convolution of one-electron Green's functions and the dynamically screened Coulomb interaction W within the plasmon-pole approximation [41]; the DFT V_{nk}^{XC} is replaced by the GW correction, and the renormalization factor –which accounts for the fact that Σ_{nk} is evaluated at Kohn-Sham eigenvalues rather than at E_{nk}^{QP}– is given by

$$Z_{nk} = \left[1 - \frac{\partial \Sigma_{nk}(E_{nk}^{KS})}{\partial E}\right]^{-1}. \tag{4.2}$$

Plane-wave calculations for 1.5 nm structures have been performed with kinetic energy cutoffs of 75, 90, 110, and 140 Ry for wavefunction expansions in structures passivated with hydrogen, methyl, fluorine, and hydroxyl, respectively. Structural and electronic properties found in simulations performed with localized orbitals were reproduced with calculations relying on plane-wave basis sets. Given the reduced dimensionality of the systems under study, a technique for cutting off long range Coulomb interactions has been employed when computing GW quasi-particle corrections. [45]

Table 4.1: Optimized cell parameter in Å along each NW's periodic direction, and characteristic cross sectional dimensions of Sn cores ϕ_{Sn} in nm. ϕ_{Sn} represent the diameters of perfectly cylindrical structures with areas matching that of each NW structure. Bulk column indicates cell parameter along corresponding crystallographic directions in bulk α-Sn.

	Bulk	1.5 nm		3 nm	
	a_0 (Å)	a_0 (Å)	ϕ_{Sn} (nm)	a_0 (Å)	ϕ_{Sn} (nm)
[100]					
CH_3	6.70	7.00	1.35	6.87	2.95
H		6.61	1.37	6.77	2.97
OH		6.11	1.43	6.40	3.04
F		6.63	1.40	6.72	3.00
[110]					
CH_3	4.74	4.82	1.45	4.79	2.93
H		4.73	1.56	4.74	2.95
OH		4.71	1.58	4.74	2.96
F		4.75	1.59	4.76	2.98
[111]					
CH_3	11.60	11.74	1.54	11.69	3.00
H		11.52	1.50	11.62	2.98
OH		11.31	1.54	11.52	3.00
F		12.04	1.52	11.77	3.05

4.4 Results and Discussion

4.4.1 Nanowire structure

Optimal structural parameters are reported in table 4.1 for the combinations of the SnNW's crystallographic orientations and surface terminations studied. Small deviations in the cell parameter relative to the corresponding lattice spacing in bulk α-Sn are found for NWs passivated with atomic terminations and NWs with larger cross sections. In 1.5 nm NWs, both hydrogen- and fluorine-passivated structures exhibit lattice spacings along the NW axis within 1% of the corresponding bulk value, with the exception of the 1.5 nm [111] structures, in which an elongation of 3.8% is observed for the fluorine-passivated structure. Larger deviations relative to the corresponding bulk cell parameters are found for thinner structures and NWs passivated with molecules: cell parameters up to 4.5% larger than the corresponding bulk values are found to be induced by the larger size of the methyl molecules, whilst a combination of the high level

of malleability of Sn-Sn bonds and the electrostatic attraction induced by the dipole moment of hydroxyl molecules at the surface favors smaller cell lengths. Despite variations in computed relaxed cell lengths encountered for different surface terminations, overall the NW's total energy displays only a remarkably weak dependence on axial strain as compared with similar strain magnitudes in the bulk.

Surface terminating groups are found to bond to surface Sn atoms without introducing significant distortions to the NW's Sn atomic structure. For surface facets exposed in $[100]$- and $[111]$-oriented structures, all terminations are found to bond to the topmost surface Sn atoms in positions exterior to the Sn core. For structures oriented along $[110]$, there are sites in which hydroxyl and fluorine are found to align to the NW surface defined by the outermost Sn atoms as the structure is allowed to relax to a minimum energy configuration. This results in Sn-X ($\mathrm{X} = \mathrm{OH}, \mathrm{F}$) bonds approximately parallel to the NW axis in $[110]$-oriented structures, as can be seen in fig. 4.1(c) and 4.1(d). The small deviations in optimal cell lengths found for $[110]$ NWs of 1.5 nm and 3 nm passivated with hydroxyl groups are attributed to this structural rearrangement, as the positioning of hydroxyl groups between Sn planes counteracts dipole attraction forces –which favour shorter cell lengths– responsible for larger deviations in $[100]$- and $[111]$- oriented structures.

Due to variations in NW shape across structures with different crystallographic orientations, and in order to provide a unified measure of NW size, we report as cross-sectional dimensions in table 4.1 the Sn core diameter (ϕ_{Sn}) corresponding to perfectly cylindrical structures with cross-sectional areas matching that of each NW structure, where areas have been computed by only taking Sn atoms into account to preserve comparability across surface terminations. Cross-sectional dimensions are found to remain constant across surface terminations for a given crystallographic orientation even for 1.5 nm structures, as variations reported in table 4.1 for a given orientation and NW size correspond to differences in Sn-Sn bond lengths in directions perpendicular to the NW axis beyond the accuracy limits of our current approximation. We thus conclude that variations in relaxed cell parameters found for different surface terminations are not followed by concomitant variations in Sn-Sn bond lengths along NW cross sections.

The crystallographic orientation of the structures is found to correlate with the magnitude of maximum deviations in optimal cell parameters with respect to

bulk values. NWs oriented along $[100]$ exhibit the largest variations with molecular terminations inducing deviations of up to 4.5% and 8.8% in 1.5 nm structures, whilst structures oriented along $[110]$ have the smallest deviations with a maximum of 1.7% for passivation with methyl molecules on the 1.5 nm NWs. As the cross-section of the NWs increases, the magnitude of deviations in the relaxed lattice spacings decreases with the 3 nm NWs exhibiting structural parameters closer to those of bulk α-Sn. This variation in structural parameters is attributed to variations in the properties of exposed surface facets with different surface terminations across structures oriented along different crystallographic axes. As NW diameter increases and the surface-to-volume ratio decreases, the impact of surface phenomena on the properties of the whole structure decreases, resulting in structural parameters rapidly approaching those of bulk α-Sn.

4.4.2 Electronic structure

The electronic structure of 1.5 nm and 3 nm α-Sn NWs is found to strongly depend on crystallographic orientation and surface terminations, with surface effects being more pronounced in thinner structures. Figure 4.2 summarizes computed DFT values for band gaps and electron affinities.

The calculations reveal that both the band gap and electron affinity can be varied for a given NW cross section and orientation via surface chemistry. Varying the surface termination groups can lead to variations in the band gap energy on the same order of magnitude as induced by quantum confinement. Variations for the SnNW's electron affinities are on the order of electronvolts for surface terminations considered. For confinement dimensions below 5 nm, the potential profile confining electrons within the NWs results in a semimetal-to-semiconductor transition with the emergence of a band gap for hydrogen terminated NWs, which we take as a reference system. The potential acting on the electrons inside the SnNW is found to be strongly related to the terminating species. As the electronegativity of the surface terminating species is increased, a shift relative to the equivalent hydrogen terminated SnNW to the electronic energy levels towards lower values and significant reduction in the energy band gap values occurs. This results in the NW size at which the semimetal-to-semiconductor occurs being dependent on *both* crystallographic orientation –as well as exposed surface facets along cross-sectional directions– and on the surface termination, with DFT calculations predicting variations be-

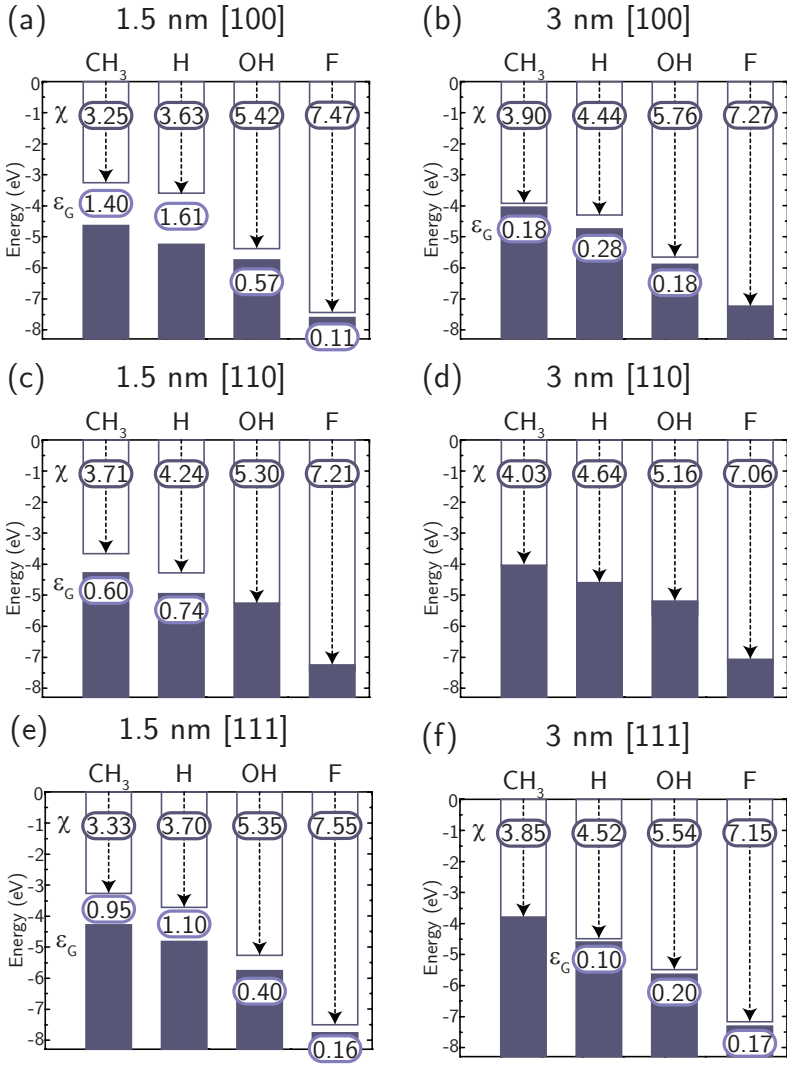

Figure 4.2: Electron affinity and band gap values for 1.5 nm and 3 nm α-Sn NWs passivated and oriented along (a),(b) [100], (c),(d) [110], and (e),(f) [111] crystallographic orientations. All reported energies are in eV. Zero of energy is set to the vacuum level.

tween semimetallic behaviour and energy band gaps up to 0.74 eV in 1.5 nm [110]-oriented structures obtained solely by varying surface passivants. Results show that for a given NW size and crystallographic orientation, the largest band gaps occur for hydrogen-passivated structures and the smallest band gaps for the highly electronegative case of fluorine, with values for structures passivated with other terminations following trends corresponding to the passivant's electronegativity. An exception to this trend is found for 3 nm [111] NWs: whilst methyl- and hydrogen-terminated structures approach semimetal behavior and exhibit band gaps below 100 meV, NWs passivated with highly electronegative species are found to exhibit larger band gaps with the fluorine-passivated struc-

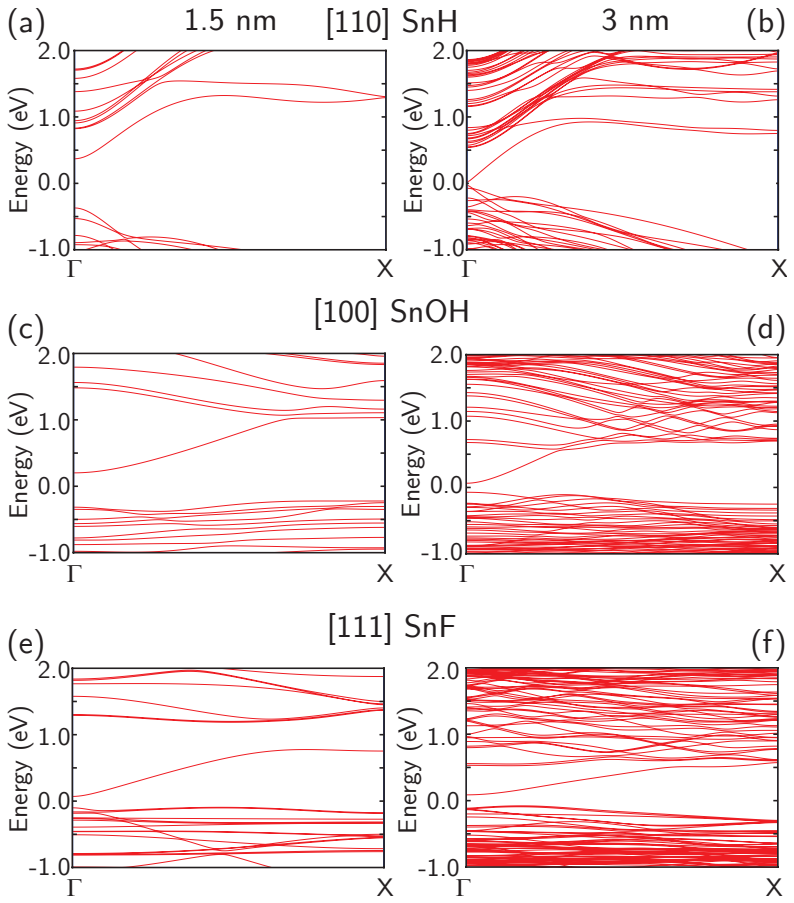

Figure 4.3: Band structures of 1.5 nm and 3 nm α-Sn NWs oriented along different orientations and passivated with varying chemical species. (a),(b) $[110]$ SnH, (c),(d) $[100]$ SnOH, and (e),(f) $[111]$ SnF. Zero of energy is set to the Fermi level.

ture even maintaining the magnitude of its band gap with respect to its 1.5 nm counterpart.

Figure 4.3 shows band structure plots for three representative SnNWs. Figure 4.3(a) and 4.3(b) depicts the electronic structure arising in the case of hydrogen-passivated $[110]$ NWs in which a direct band gap at Γ is found for both 1.5 nm and 3 nm structures, and as anticipated from the quantum confinement effect, its magnitude reduces as the cross-sectional dimensions increase and is reflected in the majority of SnNWs considered in this study. Exceptions are encountered for the cases shown in fig. 4.3(c)-(f): $[100]$ NWs passivated with hydroxyl –fig. 4.3(c) and 4.3(d)– are found to exhibit an indirect band gap for 1.5 nm NWs which transitions to a direct gap at Γ for the corresponding 3 nm structure, while the opposite situation is encountered in the band structures of hydroxyl- and fluorine-passivated $[111]$ NWs, which are predicted to exhibit

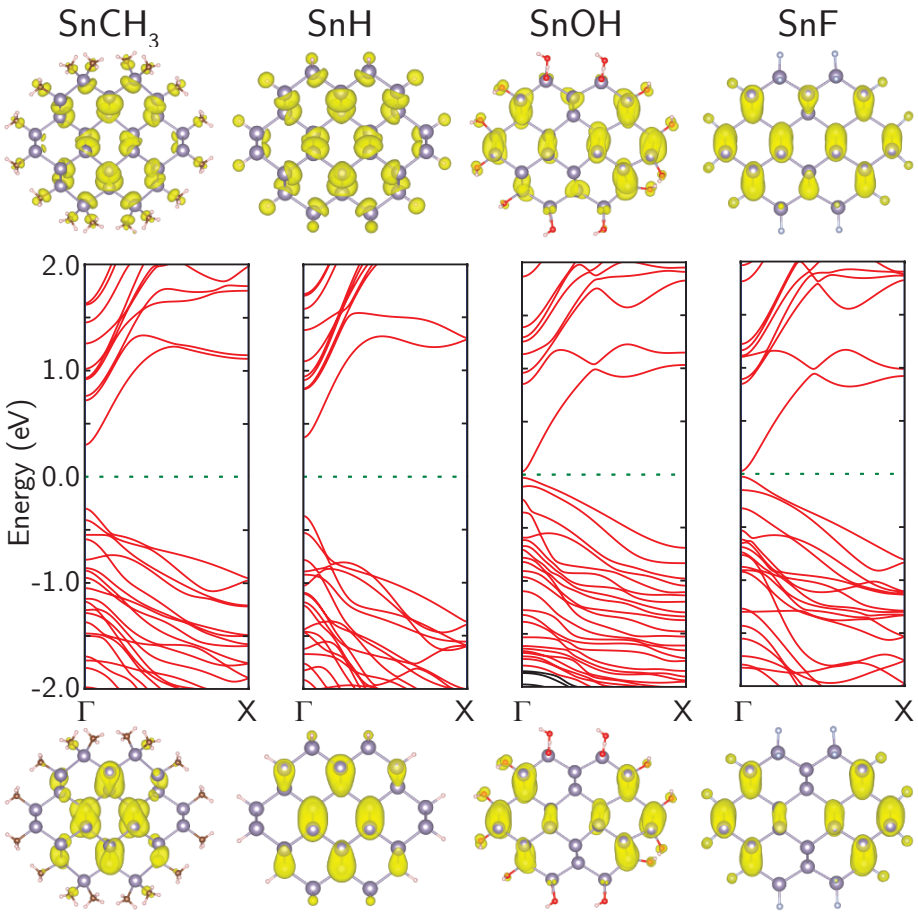

Figure 4.4: Band structures of 1.5 nm [110] α-Sn NWs passivated with varying chemical species and three-dimensionsl (3D) charge densities associated with valence band maxima (bottom) and conduction band minima (top). All charge densities taken at the same isosurface level. Zero of energy is set to the Fermi level.

a direct band gap at Γ for 1.5 nm and transition to an indirect band gap for the 3 nm SnNW as shown in fig. 4.3(e) and 4.3(f) for the case of fluorine. Another feature unique to [111] SnNWs passivated with highly electronegative terminations is a gap of approximately 0.4 eV predicted to be between the conduction band and bands at higher energies as seen in fig. 4.3(e). This same feature with a gap similar in magnitude has been observed in the band structure of 1.5 nm [111] SnNWs passivated with hydroxyl, while for less electronegative terminations, no gap is predicted within the corresponding energy range. As can be seen in fig. 4.3(f), this gap reduces with increasing NW size with values of less than 40 meV in the 3 nm structures.

Figure 4.4 shows the band structure of 1.5 nm [110]-oriented NWs for all surface terminations considered. Surface-induced variations in the potential confining

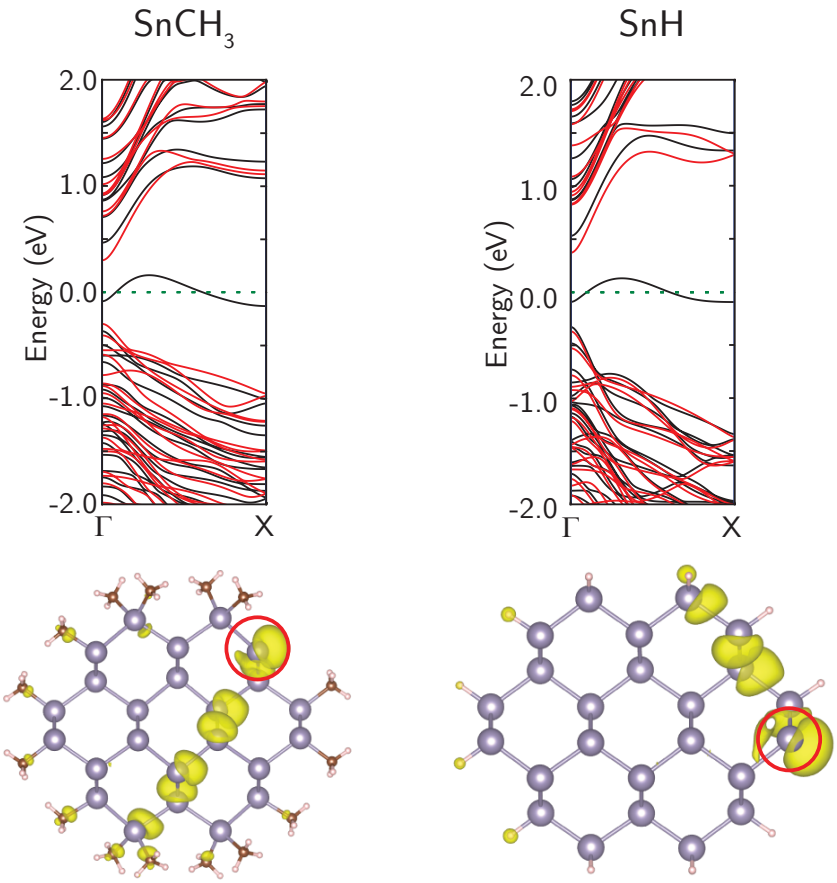

Figure 4.5: Band structures of semiconducting 1.5 nm [110] α-Sn NWs in which a passivating group has been removed from the surface (bands shown in black). Bands corresponding to completely passivated structures are shown in red for reference. At the bottom of the figure, atomistic illustrations of the NW structures in which the position of the undercoordinated Sn surface atom is indicated with a red circle are shown along with the charge densities associated with the bands crossing the Fermi level. All charge densities taken at the same isosurface level. Zero of energy is set to the Fermi level.

electrons within the NW cores are observed to interact with different bands to varying degrees with larger shifts occurring in hydroxyl- and fluorine-passivated structures. Charge densities associated with the bottom of the conduction band and the top of the valence band of each structure are portrayed at the top and bottom of fig. 4.4, respectively. The charge distributions shown are similar for both structures passivated with terminations with lower electronegativity values, while charge distributions for structures with more electronegative passivants are similar amongst themselves. Inspection of charge distributions corresponding to the first few bands away from the gap reveals similarities across terminations for bands with different indices; this indicates that modification of the confining potential induced by surface terminations can have

Table 4.2: Band gap values for 1.5 nm α-Sn NW structures as computed with DFT using pseudo-atomic orbitals (PAOs), plane waves (PWs), and PW calculations including first-order perturbative GW quasi-particle corrections.

	DFT-PAO	DFT-PW	GW
	Band gap energy ϵ_{G} (eV)		
[100]			
H	1.61	1.62	3.54
[110]			
CH_3	0.54	0.53	1.77
H	0.74	0.72	2.05
OH	0.02	0.02	0.25
F	0.03	0.01	0.70
[111]			
H	1.11	1.12	2.85

an impact on band ordering, *e.g.*, the charge distribution of the valence band edge in hydroxyl- and fluorine-passivated structures matches that of the second topmost valence band in methyl- and hydrogen-passivated NWs. In particular, none of the structures were found to present states near the Fermi level with charge densities localized at the surface indicating proper passivation of all Sn bonds. Figure 4.5 shows the band structures of semiconducting [110] NWs in which a passivant group has been removed from each structure's unit cell: an extra band crossing the Fermi level with an associated charge density localised around the undercoordinated Sn atom arises, illustrating the presence of midgap surface states in partially passivated semiconducting structures. This highlights the importance of proper surface passivation in NWs based on bulk semimetals for applications in electronic and optical devices.

In order to estimate the order of magnitude of band gaps with increased accuracy, the DFT-level description is improved by means of first-order perturbative GW quasi-particle value corrections. Corrections computed across the Brillouin zone for the conduction and valence band edges show a dependence with k-points in which the direct character exhibited by most of the structures in the study in DFT is maintained. This k-dependence indicates that an explicit GW calculation is required in order to compute the full quasi-particle band structure; in this study, we have restricted our calculations to band gap magnitudes. Table 4.2 shows computed values of band gaps estimated using DFT with pseudo-atomic orbitals (PAOs) and plane-wave (PW) basis sets, and first order perturbative GW corrected values for hydrogen-passivated SnNWs of all orien-

tations considered, and for all other surface terminations for the case of $[110]$-oriented NWs, which DFT predicts to exhibit the lowest band gap values. The band gap values predicted from approximate DFT found with both basis sets are found to be in good agreement whereas GW corrections significantly increase the magnitude of the energy band gaps. Even though non-selfconsistent GW quasiparticle corrections are expected to underestimate energy band gap values and depend on the starting DFT conditions, they have been shown to significantly improve upon DFT band gap descriptions. [24, 46]

Trends observed in DFT across different surface passivants for $[110]$-oriented structures are slightly modified after GW corrections. While structures terminated with methyl and hydrogen continue to exhibit larger band gaps than those passivated with more electronegative terminations, hydroxyl-passivated SnNWs are predicted to exhibit a smaller energy band gap than the fluorine-passivated structure. Trends observed in DFT across crystallographic orientations for hydrogen-passivated SnNWs are maintained after GW corrections with band gaps decreasing along the sequence $[100] - [111] - [110]$. Results indicate that α-Sn NWs' band gap values can be widely tuned with 1.5 nm structures exhibiting values ranging from 0.25 eV up to 3.54 eV, and variations greater than 1.5 eV achievable on single-crystalline structures by means of chemical modification. Intermediate band gap values are expected to be possible by combining more than one surface passivant in appropriate proportions, allowing a significant degree of *band gap engineering* to be achieved through surface chemistry. [11]

4.4.3 Charge and potential

The modulation of the SnNW electronic properties achieved by means of chemical passivation presented in the previous section is analyzed in terms of the potential and charge distributions across the NWs. To support this discussion, the electrostatics in the 1.5 nm and 3 nm $[110]$ NWs is considered by examining the electron difference density $\delta n(\vec{r})$, defined as the difference in charge density between self-consistent DFT and the superposition of neutral atomic densities, and the Hartree difference potential $\delta V_H(\vec{r})$ defined as

$$\nabla^2 \delta V_H[\delta n](\vec{r}) = -\frac{e^2}{4\pi\epsilon_0}\delta n(\vec{r}). \tag{4.3}$$

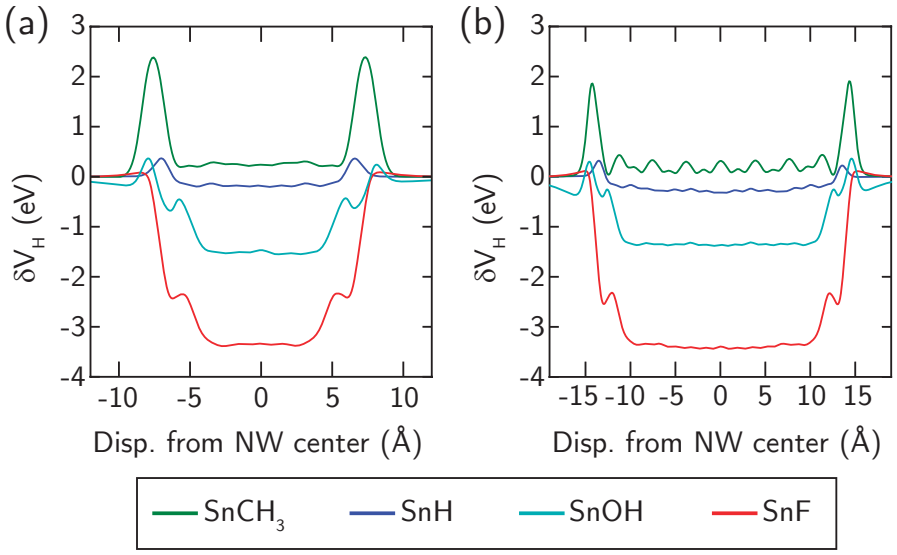

Figure 4.6: Hartree difference potential profile across (a) 1.5 nm and (b) 3 nm NW cross sections. The depth of the induced well-like profile is found to increase with passivant electronegativity. Zero of energy has been fixed to potential values in regions far from the structures.

Figure 4.6 shows the Hartree difference potential across the cross-section of [110] SnNWs with diameters of 1.5 nm and 3 nm NWs with different terminations averaged along a transverse axis. The profiles show potential-well profiles of varying depths depending on the electronegativity of the surface group with relatively shallow potential wells for the methyl- and hydrogen-terminated NWs relative to hydroxyl- and fluorine-terminated NWs; the latter surface terminations induce potential depths around an order of magnitude larger. The electrostatic potential flattens in regions near the center of the NWs with well depth comparable for the case of NWs of different diameters and orientations but with the same terminating species.

Electron difference density maps $\delta n(\vec{r})$ corresponding to these potentials are shown in fig. 4.7. As Mulliken population analyses [47] indicate, bonding to the Sn atoms withdraws charge from the NW onto the terminating groups according to their electronegativity, with the Mulliken charge on hydrogen and methyl increasing by 0.10-0.15 electron, and on hydroxyl and fluorine increasing by 0.5-0.6 electron. This is reflected in fig. 4.7 by regions of charge accumulation at the surface (green) corresponding to the atomic positions of the surface groups. Values around the Sn core indicate an overall deficit of electrons (red) with accumulation zones around bonds between atoms and especially near surface groups. In fig. 4.7(e)-4.7(h) green areas indicating accumulation

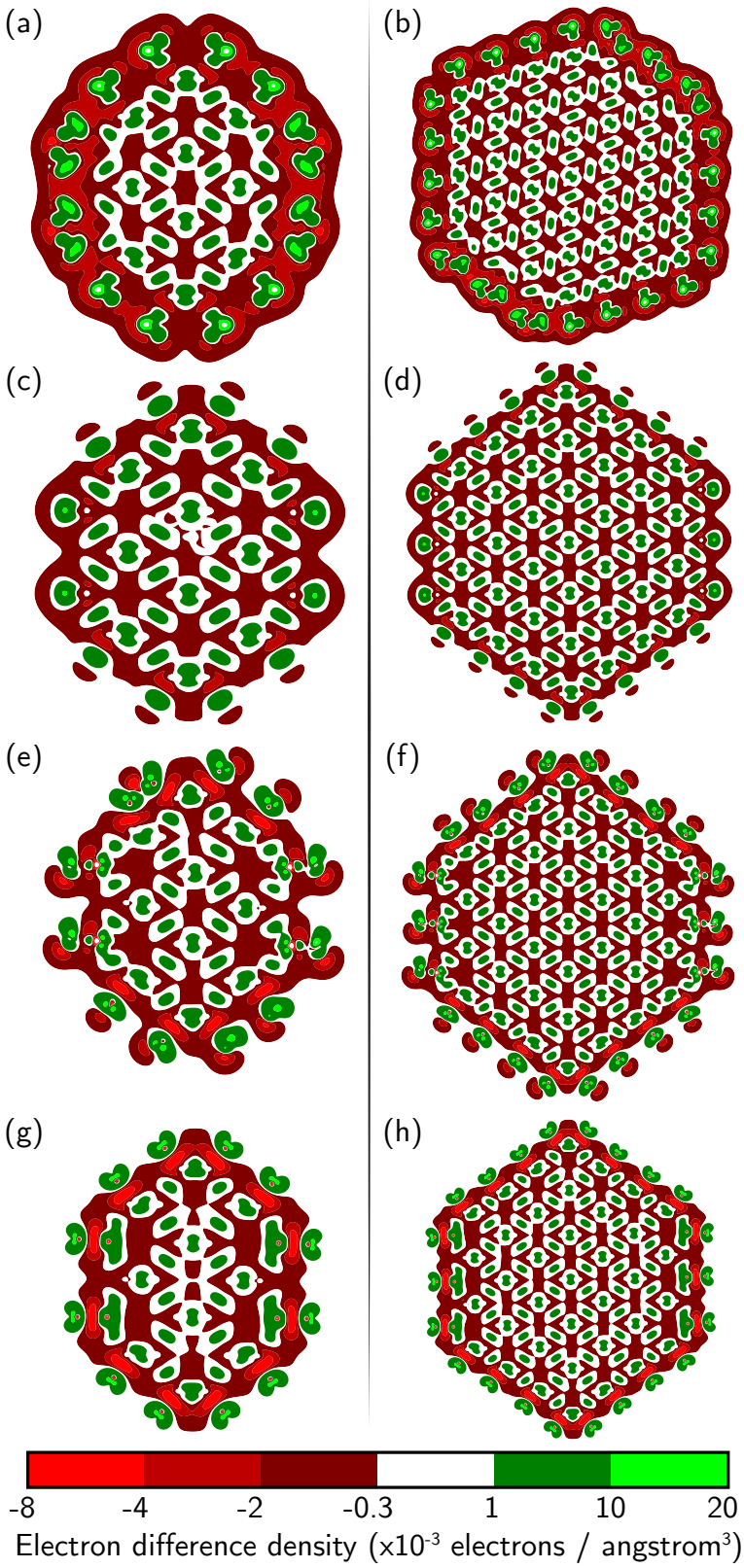

Figure 4.7: Electron difference density averaged along NW axis for 1.5 nm and 3 nm structures oriented along [110] and passivated with (a)-(b) methyl groups, (c)-(d) hydrogen atoms, (e)-(f) hydroxyl groups, and (g)-(h) fluorine atoms.

of electrons can be seen near regions of strong charge deficit at the surface and towards the center of the NWs (i.e., *inside* the Sn core); these correspond to the situation where the surface groups bond to surface Sn atoms parallel to the NW axis, as depicted in fig. 4.1(c) and 4.1(d) for hydroxyl-passivated $[110]$-oriented NW structures.

When electron withdrawal occurs at the surface of these systems, the Sn atoms' electrostatic screening results in a well-like potential profile, with the potential depth correlating to the amount of charge transfer taking place at the surface. A parallel may be drawn between these systems and the classical electrostatics problem of a charge density distributed along the surface of an infinitely long cylinder by treating electronic charge accumulation and the induced deficit in the NW core as two concentric cylindrical charge distributions. The charge distributions give rise to a potential difference between regions outside and inside both cylinders, which can be expressed as

$$\Delta\varphi = \frac{n_s}{2\pi\epsilon_0} \ln \frac{r_o}{r_i} \tag{4.4}$$

where n_s is the surface charge density, r_o is the radius of the outer cylinder, r_i the radius of the inner cylinder, and ϵ_0 is the permittivity of free space. By analogy, more electronegative passivating groups induce a larger surface charge density, thus increasing the potential difference between regions outside and inside of the NW, which results in a net lowering of the electronic states' energy and a concomitant increase in electron affinity. As discussed previously, $\Delta\varphi$ remains approximately constant across NWs with the same surface termination, which points to induced surface charge densities which do not depend on the properties of the different surface facets exposed in NWs with different crystallographic orientations, but rather on the passivant-to-surface-Sn ratio which is approximately constant for all structures of a given diameter.

Given the charge distribution inside the NW cores and their small cross-sections –of the order of the diameter of a benzene ring for the smaller NWs–, we may analyze the effect of modifying surface electronegativity by terminating groups on NW band gaps in terms of molecular electronics arguments first proposed by Aviram and Ratner [48]. By establishing a parallel between molecules and NWs, and between substituent Hammett constants and passivant electronegativities [49], the observed trend of band gap reduction with increasing surface termination electronegativity is as follows: the charge distribution induced by

highly electronegative surface groups results in a NW core deficient in electrons, increasing the SnNW's electron affinity in the core, and thus lowering the energy of its conduction band –as with the lowest unoccupied molecular orbital (LUMO) in molecular rectifiers.

By extending the analogy with molecular electronics and exploiting the dependence of NW energy band gaps with surface terminations, the properties of a rectifying junction designed by abruptly switching surface groups from fluorine to hydrogen along the length of an infinitely long 1.5 nm diameter $[110]$-oriented NW have been studied [50] [see chapter 5].

4.5 Conclusion

Electronic and structural properties of highly idealized crystalline α-Sn NWs with diameters of approximately 1.5 nm and 3 nm oriented along $[100]$, $[110]$, and $[111]$ directions with surface bonding saturated by chemical groups of varying electronegativity are reported. Structurally, the NWs exhibit a remarkably weak dependence in total energy with respect to the lattice spacings along the NW axes. Surface terminations were not found to induce significant surface reconstructions or modify bond lengths in directions perpendicular to the NWs' axes, although bonding schemes were found to vary somewhat with different terminating species. The calculations show a high degree of control over the NWs' band gap and electron affinity can be achieved by varying the degree of charge transfer between NW core and surface groups by selecting the electronegativity of the latter. Charge transfer at the surface results in well-like potential profiles which increase in depth with increasing electronegativity of the surface groups, lowering the energy of electronic states inside the NW core, increasing the system's electron affinity, and reducing band gap values in most cases. Quasiparticle corrections within a GW framework were performed to explore the range of band gap variations showing that sub-5-nm Sn structures can range from remaining semimetallic to widegap semiconductors via surface chemical modification. Surface groups allow counteracting quantum confinement effects and provide further control of electronic properties, allowing significant variations of energy band gap values along the length of structurally homogeneous SnNW cores via variation of surface coverages. Given the suitability of NW systems' electron transport properties for the design of nanoelectronics components [22] and the broad range of band gaps found for SnNWs, we expect

semimetallic systems in the sub-5-nm size range to be strong candidates for the design of next-generation charge-based components such as rectifiers and field-effect transistors.

4.6 Acknowledgments

This work was funded by Science Foundation Ireland through a Principal Investigator award Grant No. 13/IA/1956. ASS was finantially supported by an Irish Research Council graduate fellowship. We acknowledge additional support from QuantumWise. Atomistic visualizations were rendered using VESTA [51].

References

[1] L Liao, Z Zhang, B Yan, Z Zheng, Q L Bao, T Wu, C M Li, Z X Shen, J X Zhang, H Gong, J C Li, and T Yu. Multifunctional CuO nanowire devices: p-type field effect transistors and co gas sensors. *Nanotechnology*, 20(8):085203, 2009.

[2] DaeIl Kim, Yong-Kwan Kim, Sung Chan Park, Jeong Sook Ha, Junghwan Huh, Junhong Na, and Gyu-Tae Kim. Photoconductance of aligned SnO2 nanowire field effect transistors. *Appl. Phys. Lett.*, 95(4), 2009.

[3] Eric N. Dattoli, Qing Wan, Wei Guo, Yanbin Chen, Xiaoqing Pan, and Wei Lu. Fully transparent thin-film transistor devices based on SnO2 nanowires. *Nano Lett.*, 7(8):2463–2469, 2007.

[4] Q. T. Zhao, S. Richter, C. Schulte-Braucks, L. Knoll, S. Blaeser, G. V. Luong, S. Trellenkamp, A. Schäfer, A. Tiedemann, J. M. Hartmann, K. Bourdelle, and S. Mantl. Strained Si and SiGe nanowire tunnel FETs for logic and analog applications. *IEEE J. Electron Devices Soc.*, 3(3):103–114, 2015.

[5] F. Conzatti, M. G. Pala, D. Esseni, E. Bano, and L. Selmi. Strain-induced performance improvements in InAs nanowire tunnel FETs. *IEEE Trans. Electron Devices*, 59(8):2085–2092, 2012.

[6] R. S. Wagner and W. C. Ellis. Vapor-solid-liquid mechanism of single crystal growth. *Appl. Phys. Lett.*, 4(5):89–90, 1964.

[7] D. D. D. Ma, C. S. Lee, F. C. K. Au, S. Y. Tong, and S. T. Lee. Small-diameter silicon nanowire surfaces. *Science*, 299(5614):1874–1877, 2003.

[8] A. J. Read, R. J. Needs, K. J. Nash, L. T. Canham, P. D. J. Calcott, and A. Qteish. First-principles calculations of the electronic properties of silicon quantum wires. *Phys. Rev. Lett.*, 69:1232–1235, 1992.

[9] Xinyuan Zhao, C. M. Wei, L. Yang, and M. Y. Chou. Quantum confinement and electronic properties of silicon nanowires. *Phys. Rev. Lett.*, 92:236805, 2004.

[10] Lida Ansari, Giorgos Fagas, Jean-Pierre Colinge, and James C. Greer. A proposed confinement modulated gap nanowire transistor based on a metal (tin). *Nano Lett.*, 12(5):2222–2227, 2012.

[11] Paul W. Leu, Bin Shan, and Kyeongjae Cho. Surface chemical control of the electronic structure of silicon nanowires: Density functional calculations. *Phys. Rev. B*, 73:195320, 2006.

[12] Michael Nolan, Sean O'Callaghan, Giorgos Fagas, James C. Greer, and Thomas Frauenheim. Silicon nanowire band gap modification. *Nano Lett.*, 7(1):34–38, 2007.

[13] Keenan Zhuo and Mei-Yin Chou. Surface passivation and orientation dependence in the electronic properties of silicon nanowires. *J. Phys.: Condens. Matter*, 25(14):145501, 2013.

[14] William Paul. Band structure of the intermetallic semiconductors from pressure experiments. *J. Appl. Phys.*, 32(10):2082–2094, 1961.

[15] R.F.C. Farrow, D.S. Robertson, G.M. Williams, A.G. Cullis, G.R. Jones, I.M. Young, and P.N.J. Dennis. The growth of metastable, heteroepitaxial films of α-Sn by metal beam epitaxy. *J. Cryst. Growth*, 54(3):507 – 518, 1981.

[16] H. Höchst and I. Hernández-Calderón. Angular resolved photoemission of InSb(001) and heteroepitaxial films of α-Sn(001). *Surf. Sci.*, 126(1):25 – 31, 1983.

[17] P. John, T. Miller, and T.-C. Chiang. Core-level photoemission studies of the α -Sn/InSb(100) heterostructure system. *Phys. Rev. B*, 39:3223–3229, 1989.

[18] Kazuyuki Ueda, Hiroshi Nakayama, Makoto Sekine, and Hiroshi Fujita. Auger valence electron spectroscopy of a structural phase transformation in metastable alpha-Sn grown on InSb (001). *Vacuum*, 42(8):547 – 553, 1991.

[19] Hyung Soon Im, Yong Jae Cho, Young Rok Lim, Chan Su Jung, Dong Myung Jang, Jeunghee Park, Fazel Shojaei, and Hong Seok Kang.

Phase evolution of tin nanocrystals in lithium ion batteries. *ACS Nano*, 7(12):11103–11111, 2013.

[20] Sebastian Küfner, Jürgen Furthmüller, Lars Matthes, Martin Fitzner, and Friedhelm Bechstedt. Structural and electronic properties of α-tin nanocrystals from first principles. *Phys. Rev. B*, 87:235307, 2013.

[21] N. Oehl, L. Hardenberg, M. Knipper, J. Kolny-Olesiak, J. Parisi, and T. Plaggenborg. Critical size for the β- to α-transformation in tin nanoparticles after lithium insertion and extraction. *CrystEngComm*, 17:3695–3700, 2015.

[22] J. Appenzeller, J. Knoch, M. T. Bjork, H. Riel, H. Schmid, and W. Riess. Toward nanowire electronics. *IEEE Trans. Electron Devices*, 55(11):2827–2845, 2008.

[23] Lars Hedin. New method for calculating the one-particle Green's function with application to the electron-gas problem. *Phys. Rev.*, 139:A796–A823, 1965.

[24] M. van Schilfgaarde, Takao Kotani, and S. Faleev. Quasiparticle self-consistent GW theory. *Phys. Rev. Lett.*, 96:226402, 2006.

[25] Myrta Grüning, Andrea Marini, and Angel Rubio. Density functionals from many-body perturbation theory: The band gap for semiconductors and insulators. *J. Chem. Phys.*, 124(15), 2006.

[26] Reiner M. Dreizler and Eberhard K.U. Gross. *Density functional theory: An approach to the quantum many-body problem*. Springer, Berlin, Germany, 1990.

[27] José M Soler, Emilio Artacho, Julian D Gale, Alberto Garcia, Javier Junquera, Pablo Ordejon, and Daniel Sanchez-Portal. The SIESTA method for ab initio order-N materials simulation. *J. Phys.: Condens. Matter*, 14(11):2745, 2002.

[28] Atomistix ToolKit version 2015-1 QuantumWise A/S. *www.quantumwise.com (accessed August 2016)*.

[29] W. Kohn and L. J. Sham. Self-consistent equations including exchange and correlation effects. *Phys. Rev.*, 140:A1133–A1138, 1965.

[30] J.P. Perdew, K. Burke, and M. Ernzerhof. Generalized gradient approximation made simple. *Phys. Rev. Lett.*, 77:3865–3868, 1996.

[31] I. Morrison, D.M. Bylander, and L. Kleinman. Non-local Hermitian norm-conserving Vanderbilt pseudopotenial. *Phys. Rev. B*, 47:6728–6731, 1993.

[32] T. Ozaki. Variationally optimized atomic orbitals for large-scale electronic structures. *Phys. Rev. B*, 67:155108, 2003.

[33] T. Ozaki and H. Kino. Numerical atomic basis orbitals from H to Kr. *Phys. Rev. B*, 69:195113, 2004.

[34] Hendrik J. Monkhorst and James D. Pack. Special points for Brillouin-zone integrations. *Phys. Rev. B*, 13:5188–5192, 1976.

[35] J. Thewlis and A. R. Davey. Thermal expansion of grey tin. *Nature*, 174:1011, 1954.

[36] C. J. Buchenauer, M. Cardona, and F. H. Pollak. Raman scattering in gray tin. *Phys. Rev. B*, 3:1243–1244, 1971.

[37] Hiroaki Kamioka. Temperature variations of elastic moduli up to eutectic temperature in tin-bismuth alloys. *Jpn. J. Appl. Phys.*, 22(12R):1805, 1983.

[38] John P. Perdew, Robert G. Parr, Mel Levy, and Jose L. Balduz. Density-functional theory for fractional particle number: Derivative discontinuities of the energy. *Phys. Rev. Lett.*, 49:1691–1694, 1982.

[39] John P. Perdew and Mel Levy. Physical content of the exact Kohn-Sham orbital energies: Band gaps and derivative discontinuities. *Phys. Rev. Lett.*, 51:1884–1887, 1983.

[40] Andrea Marini, Conor Hogan, Myrta Grüning, and Daniele Varsano. YAMBO: An ab initio tool for excited state calculations. *Comput. Phys. Commun.*, 180(8):1392 – 1403, 2009.

[41] F. Aryasetiawan and O. Gunnarsson. The GW method. *Rep. Prog. Phys.*, 61(3):237, 1998.

[42] Paolo Giannozzi, Stefano Baroni, Nicola Bonini, Matteo Calandra, Roberto Car, Carlo Cavazzoni, Davide Ceresoli, Guido L Chiarotti, Matteo Cococcioni, Ismaila Dabo, Andrea Dal Corso, Stefano de Gironcoli, Stefano Fabris, Guido Fratesi, Ralph Gebauer, Uwe Gerstmann, Christos Gougoussis, Anton Kokalj, Michele Lazzeri, Layla Martin-Samos, Nicola Marzari, Francesco Mauri, Riccardo Mazzarello, Stefano Paolini, Alfredo Pasquarello, Lorenzo Paulatto, Carlo Sbraccia, Sandro Scandolo, Gabriele Sclau-

zero, Ari P Seitsonen, Alexander Smogunov, Paolo Umari, and Renata M Wentzcovitch. QUANTUMESPRESSO: a modular and open-source software project for quantum simulations of materials. *J. Phys.: Condens. Matter*, 21(39):395502, 2009.

[43] N. Troullier and José Luís Martins. Efficient pseudopotentials for plane-wave calculations. *Phys. Rev. B*, 43:1993–2006, 1991.

[44] Mark S. Hybertsen and Steven G. Louie. Electron correlation in semiconductors and insulators: Band gaps and quasiparticle energies. *Phys. Rev. B*, 34:5390–5413, 1986.

[45] Carlo A. Rozzi, Daniele Varsano, Andrea Marini, Eberhard K. U. Gross, and Angel Rubio. Exact coulomb cutoff technique for supercell calculations. *Phys. Rev. B*, 73:205119, 2006.

[46] Mark van Schilfgaarde, Takao Kotani, and Sergey V. Faleev. Adequacy of approximations in GW theory. *Phys. Rev. B*, 74:245125, 2006.

[47] R. S. Mulliken. Electronic population analysis on LCAO–MO molecular wave functions. *J. Chem. Phys.*, 23(10):1833–1840, 1955.

[48] Arieh Aviram and Mark A. Ratner. Molecular rectifiers. *Chem. Phys. Lett.*, 29(2):277 – 283, 1974.

[49] Lei Liu, Yao Fu, Rui Liu, Rui-Qiong Li, and Qing-Xiang Guo. Hammett equation and generalized Pauling's electronegativity equation. *J. Chem. Inf. Comput. Sci.*, 44(2):652–657, 2004.

[50] Alfonso Sanchez-Soares and James C. Greer. A semimetal nanowire rectifier: Balancing quantum confinement and surface electronegativity. *Nano Lett.*, 16(12):7639–7644, 2016.

[51] Koichi Momma and Fujio Izumi. *VESTA3* for three-dimensional visualization of crystal, volumetric and morphology data. *J. Appl. Crystallogr.*, 44(6):1272–1276, 2011.

Chapter 5

A semimetal nanowire rectifier: balancing quantum confinement and surface electronegativity

5.1 Abstract

For semimetal nanowires with diameters on the order of ten nanometer, a semimetal-to-semiconductor transition is observed due to quantum confinement effects. Quantum confinement in a semimetal lifts the degeneracy of the conduction and valence bands in a 'zero' gap semimetal, or shifts energy levels with a 'negative' overlap to form conduction and valence bands. For semimetal nanowires with diameters less than 10 nanometer, the band gap energy can be significantly larger than the thermal energy at room temperature resulting in a new class of semiconductors suitable for nanoelectronics. As a nanowire's

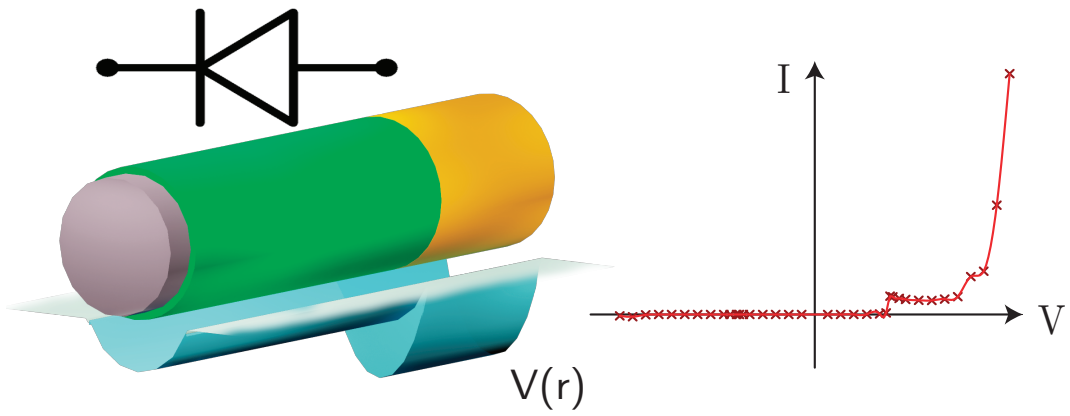

diameter is reduced, its surface-to-volume ratio increases rapidly leading to an increased impact of surface chemistry on its electronic structure. Energy level shifts to states in the vicinity of the Fermi energy with varying surface electronegativity are shown to be comparable in magnitude to quantum confinement effects arising in nanowire's with diameters of a few nanometer; these two effects can counteract one another leading to semimetallic behavior at nanowire cross sections at which confinement effects would otherwise dominate. Abruptly changing the surface terminating species along the length of a nanowire can lead to an abrupt change in the surface electronegativity. This can result in the formation of a semimetal-semiconductor junction within a *mono*material nanowire without impurity doping nor requiring the formation of a heterojunction. Using density functional theory in tandem with a Green's function approach to determine electronic structure and charge transport, respectively, current rectification is calculated for such a junction. Current rectification ratios of the order of $10^3 - 10^5$ are predicted at applied biases as low as 300 mV. It is concluded that rectification can be achieved at essentially molecular length scales with conventional biasing, while rivaling the performance of macroscopic semiconductor diodes.

Molecular electronics aims to produce diode, transistor, or logic functions in single molecules or small molecular assemblies. Diode behavior is the most fundamental of these as rectifying junctions can be arranged and combined with electrostatic gating to provide a transistor or switching function, and hence the realization of all Boolean operations, as well as signal amplification, modulation, and other basic operations that enable electronic circuits. Molecular diodes have been demonstrated with increasing success and rectification ratios (I_{ON}/I_{OFF}) greater than 200 have been recently reported using electrochemical methods [1]. Overall, operating voltages with molecular and chemical methods tend to be relatively high (> 1 V) and rectification ratios low (< 10) rendering single molecular diodes mostly unsuitable for nanoelectronics. As well, reproducible molecular placement and electrode bonding remains a challenge for single molecule electronics.

In the following, a strategy is presented which realizes a Schottky junction in a *mono*material nanowire using ideas derived from molecular electronics in that chemistry is used to locally modify electron affinity in order to control current flow [2]. Applying this approach, surface terminating groups of differing electronegativity are introduced and shown to create semimetallic and semiconducting regions in α-tin nanowires (SnNWs). The semimetal α-tin (α-Sn)

is used as an exemplar to explore quantum confinement versus surface electronegativity through use of a combination of density functional theory (DFT) [3] for electronic structure and a Green's function method [4] for studying charge transport across the junction. α-Sn nanowires are selected as they display advantageous properties for nanoelectronics in terms of the band gaps that can be achieved at small nanowire diameters [5], and relative to other semimetal it is straightforward to passivate the nanowire's surface without the introduction of defect states within a quantum confinement induced band gap.

Although the bulk α-phase or diamond crystal structure of Sn is not stable at room temperature [6], it can be stabilized in thin films [7–10]. For a hydrogen terminated SnNW with a diameter of 5 nm, the semimetal-to-semiconductor transition is expected to yield a band gap greater than 100 meV and the value increases rapidly to the order of an electronvolt with decreasing diameter [5]. Note that the calculations reported by Ansari *et al.* [5] are performed using DFT within the local density approximation (LDA), such that the reported nanowire diameters are a lower limit for the band gaps. Due to deficiencies in approximations employed in the LDA or generalized gradient approximation (GGA) for the exchange-correlation functional used in DFT calculations, the quantum confinement induced band gaps are significantly underpredicted as shown by GW [11]-corrected calculations for SnNWs [12] [see chapter 4]. The GW approximation yields values much closer to experimental band gap energies than DFT using LDA or GGA [13]. Figure 5.1(a) shows the band gap variation with NW diameter for SnNWs with different surface terminations as computed with standard GGA functionals; fig. 5.1(b) shows the estimated band gaps as a function of diameter after including the GW corrections for the 1.5 nm and 2 nm NWs. The meta-GGA method [14] is calibrated using the GW band gaps for the smaller diameter SnNWs and applied to calculation of the band gaps for 3 nm SnNWs. These GW and meta-GGA calculated values are expected to be a more accurate reflection of the predicted band gaps than the DFT-GGA band gaps.

It is seen in fig. 5.1 that DFT-GGA calculations predict hydrogen terminated $[110]$ SnNWs to have a significant band gap relative to the thermal energy $\mathrm{k_B T}$ for NW diameters less than 4 nm, whereas the hydroyxl and flourine terminated SnNWs remain semimetallic essentially for all diameters. However, when the band gaps are corrected using GW and meta-GGA estimates, it is seen that the semimetal-to-semiconductor transition for the hydrogen terminated SnNWs occurs for much larger diameters than predicted by DFT-GGA calculations. The

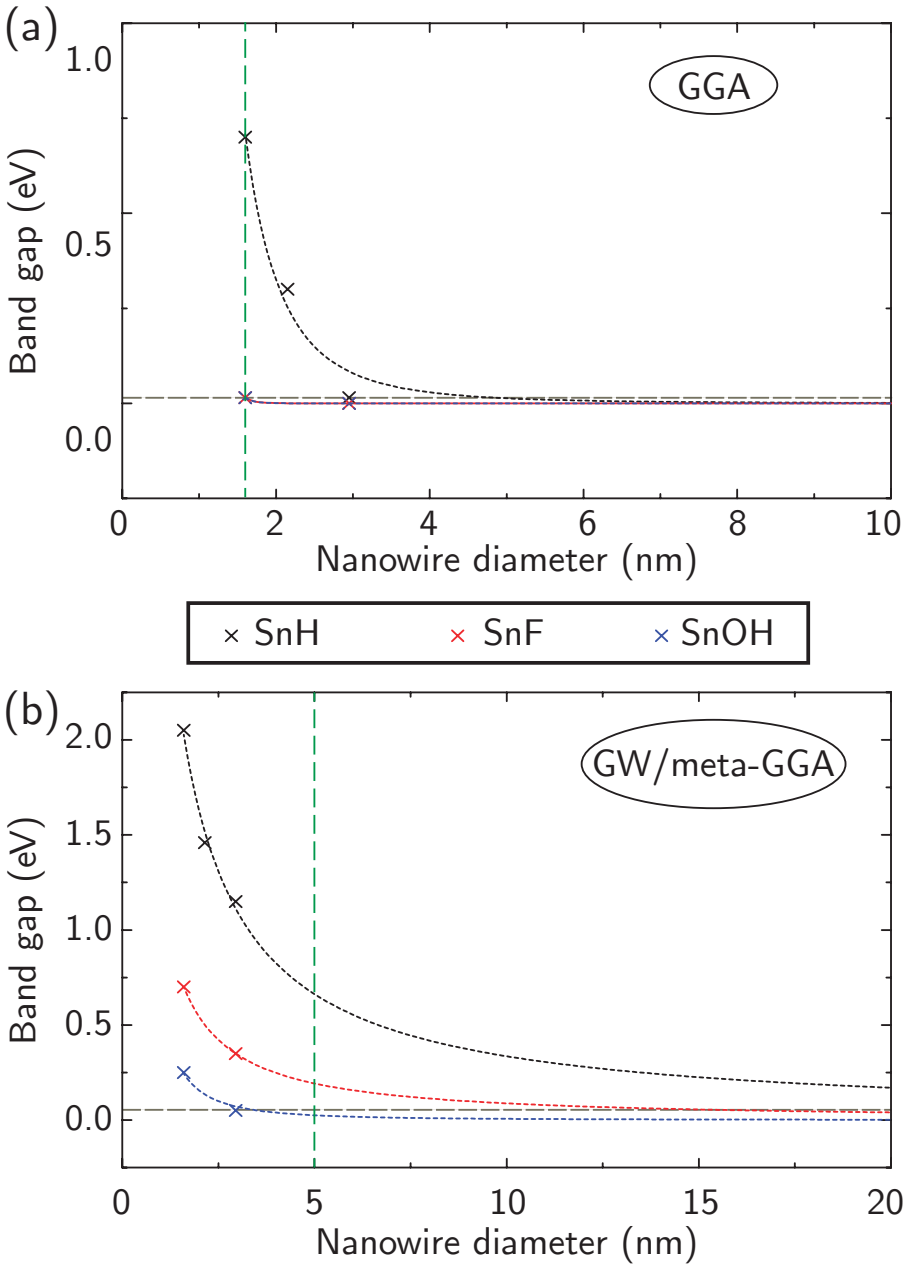

Figure 5.1: Evolution of band gap energies in $[110]$ α-Sn nanowires with diameter from simulations based on DFT with (a) standard GGA functionals and (b) corrected using a scheme involving meta-GGA functionals and many-body perturbation theory. The crossing of each curve with the horizontal dashed line indicates the minimum diameter at which semimetallic behavior is expected. Vertical dashed lines indicate diameters at which band offsets between hydrogen- and fluorine-terminated structures (GGA) and hydrogen- and hydroxyl-terminated structures (corrected) match.

fluorine terminated SnNWs become appreciably semiconducting at diameters less than 10 nm, whereas the hydroxyl terminated SnNWs are predicted to be semimetallic for all diameters > 3 nm. Below the semimetal-to-semconductor transition, the SnNWs are intrinsic semiconductors implying the Fermi level lies midgap. If a junction is formed between semimetallic and semiconducting regions, the Fermi levels must align implying a band offset between the two regions of $E_g/2$, where E_g is the band gap of the semiconducting region. Near the junction, there is band bending due to the charge transfer required to align the Fermi levels, which can result in a raising or lowering of the junction barrier. However, the band offsets between the two regions not dominated by band bending is given by $E_g/2$.

Electron and hole transport is treated using DFT-GGA. This allows the use of smaller SnNW of diameter 1.5 nm to demonstrate rectification while mimicking the electronic structure of $\approx$ 5 nm SnNWs as predicted by GW and meta-GGA methods. This choice is motivated as the reduced electrostatic screening occurring in intrinsic semiconductors requires simulation of a semiconducting region of 20 nm length or larger to ensure that application of an external electric field across the junction does not artificially constrain the resulting electrostatic potential due to the electrode boundary conditions. Simulation of smaller SnNWs using the DFT-GGA approximation allows for band offsets as predicted by the meta-GGA for 5 nm SnNWs to be achieved with the 1.5 nm SnNWs and simultaneously reduce the high computational cost of the quantum transport calculations. As indicated by the vertical dashed lines in fig. 5.1, the band gap for the hydrogen terminated SnNWs from the DFT-GGA calculations at 1.5 nm corresponds, approximately, to predicted band gap for a 5 nm hydrogen terminated SnNW as predicted by meta-GGA. The DFT-GGA calculations result in both fluorine and hydroxyl terminated SnNWs at 1.5 nm being semimetallic. From the meta-GGA calculations, the hydroxyl terminated SnNW at 5 nm is semimetallic whereas the fluorine terminated SnNW is predicted to have a band gap of $\approx$ 200 meV. The simulation of hydroxyl terminated SnNWs requires a higher degree of convergence with respect to the fineness of the real-space grid and the size of the basis set employed for expanding wavefunctions, resulting in a much higher computational cost. Hence to demonstrate the effect of forming a junction by altering the surface electronegativity in a realistic description of the electronic structure of 5 nm SnNW, a similar band offset is engineered in a 1.5 nm SnNW by altering the surface chemistry between hydrogen (semiconducting) and fluorine (semimetallic) regions within a DFT-GGA approximation. This approach

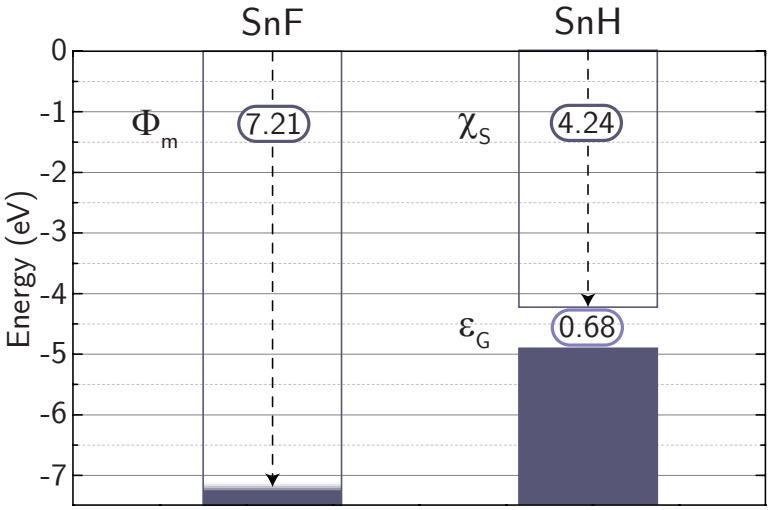

Figure 5.2: Computed work function (Φ_m), electron affinity (χ_s), and band gap (ε_G) for 1.5 nm diameter $[110]$ α-Sn NWs passivated with fluorine and hydrogen within DFT-GGA. The larger electronegativity of fluorine is found to counteract the quantum-confinement induced bandgap observed for hydrogen terminated NWs.

engineers a similar potential barrier in the 1.5 nm SnNW using DFT-GGA, while capturing the junction physics of the larger 5 nm hydrogen/hydroxyl terminated SnNWs while retaining a tractable computational demand.

It is well understood that surface chemistry can result in significant variation of band gap energies in semiconductor thin films and nanowires for critical dimensions less than 10 nm. In silicon nanowires, increasing the electron affinity of surface terminating groups results in a red shift to the band gap energies [15, 16]. Just as surface chemistry can compensate against the effects of quantum confinement in semiconductor NWs, increasing the electronegativity of surface terminating groups or atoms bonding to a semimetal NW compensates against the quantum confinement induced band gap at small NW diameters. However, the smaller band gaps induced by the confinement effect in semimetals NWs relative to semiconductor NWs are shown to allow the surface chemistry to vary the electronic character of the NWs from semimetallic to semiconducting. In the following, an α-Sn nanowire with hydrogen termination is chosen as a reference system against which the electron affinity and band gap shift of a fluorine-passivated NW are compared.

Using fluorine as passivating groups, a nearly semimetallic NW is achieved with an energy gap of $\varepsilon_g \sim k_B T$ for the case of α-Sn NWs oriented along the $[110]$ crystallographic direction and with a diameter of $\approx$ 1.5 nm. As the quantum

confinement effects decrease for increasing NW diameter, the fluorine terminated SnNWs are predicted to remain semimetallic at room temperature for diameters $>$ 1.5 nm within DFT-GGA. The competing effect of quantum confinement versus surface termination can be understood in relation to surface dipoles induced by charge transfer at the surface. For large electron affinities, the terminating atoms or molecular groups draw charge out of the NW core and the resulting surface negative charge can, in a first approximation, be thought of as a charge density distributed along the surface of a cylinder. The image potentials in the semimetal nanowire are of opposing polarity and may be treated as a surface charge density on the surface of an inner concentric cylinder. In a macroscopic continuum model for charged concentric cylinders, the charge distributions would give rise to a potential difference between regions outside and inside both cylinders which can be expressed as

$$\Delta\varphi = \frac{n_s}{2\pi\epsilon_0} \ln \frac{r_o}{r_i}, \tag{5.1}$$

where n_s is the surface charge density, r_o is the radius of the outer cylinder, r_i the radius of the inner cylinder, and ϵ_0 is the permittivity of free space. For two concentric charged cylinders, Gauss' law reveals there is no electric field within the region enclosed by both cylinders; the net effect of the surface charge distribution is to produce a constant potential shift within the region enclosed by both cylinders relative to their exterior. This heuristic picture based on macroscopic electrostatics provides insight into the same outcome for the nanowires. The result of increasing the magnitude of the surface dipoles is also to increase the potential difference between the exterior and interior of the NW. A larger electronegativity of the terminating species increases the magnitude of the surface dipoles leading to an increase in the electrostatic potential between the core of the nanowire relative to vacuum, or otherwise the region encapsulating the NW. This potential difference results in an increase in the NW's ionization potential. Conversely, the quantum confinement effect works to increase the energy of an electron confined within the NW, and thus a partial cancellation occurs between the two effects with both effects offsetting one another if the surface electronegativity is sufficiently large. The electronic structure of the SnNWs is computed with DFT [17, 18] using the PBE [19] formulation of the GGA. Double-ζ-polarized basis sets consisting of localized pseudo-atomic orbitals (PAOs) [20, 21] are used in conjunction with norm-conserving pseudopotentials [22]. Electronic structure of 1.5 nm diameter $[110]$ α-Sn NWs are

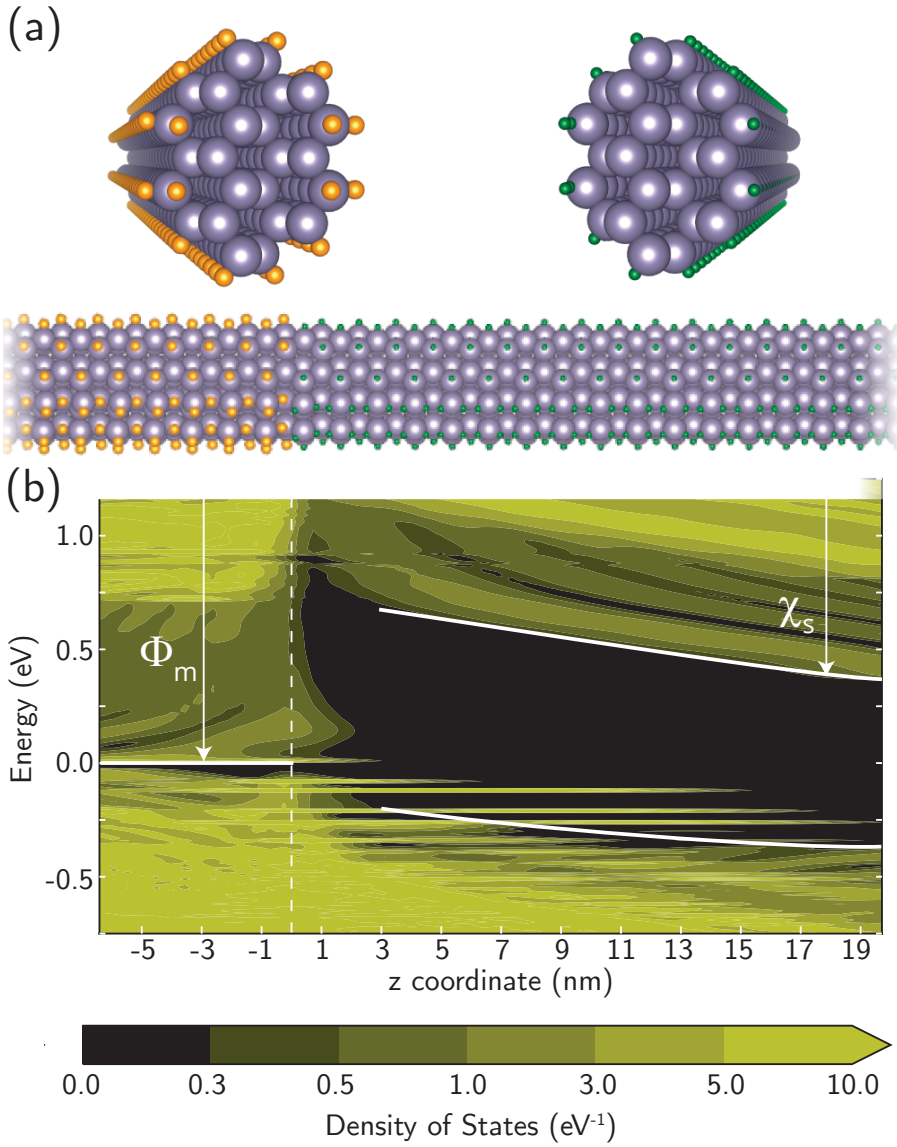

Figure 5.3: A semimetal-semiconductor junction is realized by abruptly switching surface terminations from fluorine (left) to hydrogen (right) along the length of a $[110]$ α-Sn NW of 1.5 nm diameter. The plot shows the calculated local density of states (LDoS) across the junction, in which the work function of the semimetallic region (Φ_m) and electron affinity of the semiconducting region (χ_s) are indicated as predicted by DFT-GGA.

calculated with hydrogen and fluorine surface terminations. The resulting band gap energies and electron affinities are presented in fig. 5.2. For the hydrogen terminated SnNW, the energy band gap and electron affinity are found to be 0.68 eV and 4.24 eV, respectively. Upon replacing the surface terminating species by fluorine, the electron affinity increases dramatically to 7.21 eV and the band gap reduces to a mere 30 meV. The larger electronegativity of the fluorine atoms results in a larger charge transfer at the NW surface relative to the

hydrogen termination. That the larger surface dipoles offset the quantum confinement potential is confirmed by the DFT calculations and is consistent with the qualitative electrostatic model described in eq. (5.1). The 30 meV band gap is of the order of $\mathrm{k_B T}$ at room temperature and hence a significant population in the conduction band by thermally excited electrons results in semimetallic behavior.

The nanowire geometry used for studying the electronic structure and electronic transport for a junction formed by varying the surface terminations is obtained by minimizing the total electronic energy with respect to atomic positions (geometry relaxation) on a region extending 5 nm either side of the junction until computed forces are below 5×10^{-2} eV/ Å. Figure 5.3(a) shows the relaxed nanowire structure. The junction is formed by altering the surface terminations with the left hand side of the SnNW's surface terminated by fluorine atoms and the right hand side is terminated by hydrogen atoms. The largest structural rearrangements in the NW relative to the starting structure are associated directly with the surface termination groups. There is comparably little distortion to the NW core atoms. In the region with hydrogen terminations, the NW is semiconducting whereas in the region terminated by fluorine atoms the local density of states (LDoS) reveals semimetallic behavior. Hence where the two regions defined by the differing surface terminations meet, a semimetal-semiconductor junction is formed as shown in fig. 5.3(b) with the junction LDoS reflecting a semimetal-semiconductor nature. The vertical dashed line indicates a notional *metallurgical junction* defined as the plane across which the surface terminating atoms are changed from fluorine to hydrogen. Although shown as abrupt, diodes with graded junction profiles on the order of a nanometer are known to be able to provide strongly rectifying behavior. The electronic structure of the junction given by the LDoS clearly shows the characteristics of a Schottky junction with the conduction and valence bands bending upward in energy near the junction due to the mismatch between the electron affinities in each region, and consistent with charge transfer to the semimetallic side of the junction. On the other hand, the junction differs from common engineering of Schottky diodes in that the semiconducting region induced by the hydrogen termination is intrinsic, hence the Fermi level aligns to mid-gap in the semiconductor side at regions significantly distant from the junction. In this sense, the band bending resembles a metal/*n*-type semiconductor junction. Due to the intrinsic character of the semiconducting side, the upward band bending of the conduction and valence band edges directly at the junction leads to the Fermi level alig-

ning closer to the valence band edge near the metallurgical junction. In this sense, the Fermi level alignment at the junction resembles a metal/*p*-type semiconductor junction. This difference leads to unconventional electron transport characteristics. A second characteristic of the junction is the presence of evanescent states or metal-induced gap states (MIGS) [23] below the Fermi level and extending up to approximately 20 nm away from the semimetallic region and into the semiconducting region. Due to the Fermi level alignment near the valence band edge, the MIGS directly impact the current voltage (I-V) characteristics across the junction as reflected by the charge transport calculations. Similar MIG states have been observed in calculations for an aluminum-silicon NW junction [24]. In their study a short silicon nanowire is connected between two metal electrodes leading to the formation of two junctions, *i.e.*, leading to penetration of the MIGS into the NW from two metallic regions.

The alignment of the bands at the interface results in a Schottky barrier (usually denoted as Φ_B) of approximately 0.9 eV. The relatively large band gap of the semiconducting region results in an extremely low population at room temperature of conduction band electrons. Likewise, the population in the semimetallic region of electrons with energies in the tail of the thermal distribution and at the top of the Schottky barrier is extremely small. These two conditions effectively rule out any significant electron flow between the semimetal and the semiconducting region's conduction band for typical applied voltages.

To investigate the electronic current across the junction as an external voltage is applied, the nonequilibrium Green's function (NEGF) formalism is used [4, 25]. Figure 5.4(a) shows the LDoS with a forward bias of 0.75 V which corresponds to a positive voltage applied to the semimetallic region relative to the semiconducting region. For this voltage polarity, the electronic states in the semiconducting region shift towards higher energies relative to the electron energies in the semimetallic region. The built-in electric field arising from the charge redistribution required to equilibrate the junction at zero bias is offset by the application of a positive voltage across the junction. The conduction mechanism for forward bias arises from electron tunneling from the valence band into the semimetallic region. For sufficiently large voltages, the MIGS near in energy to the semimetal quasi-Fermi level mix with the semiconducting region's valence band states when the device becomes strongly *ON* as depicted in fig. 5.4(a). This behavior is reflected in the energy-resolved current as also shown in fig. 5.4(a) where a peak is observed near the Fermi level where the MIGS overlap with the valence band in the semiconducting region. This mechanism is distinct to the

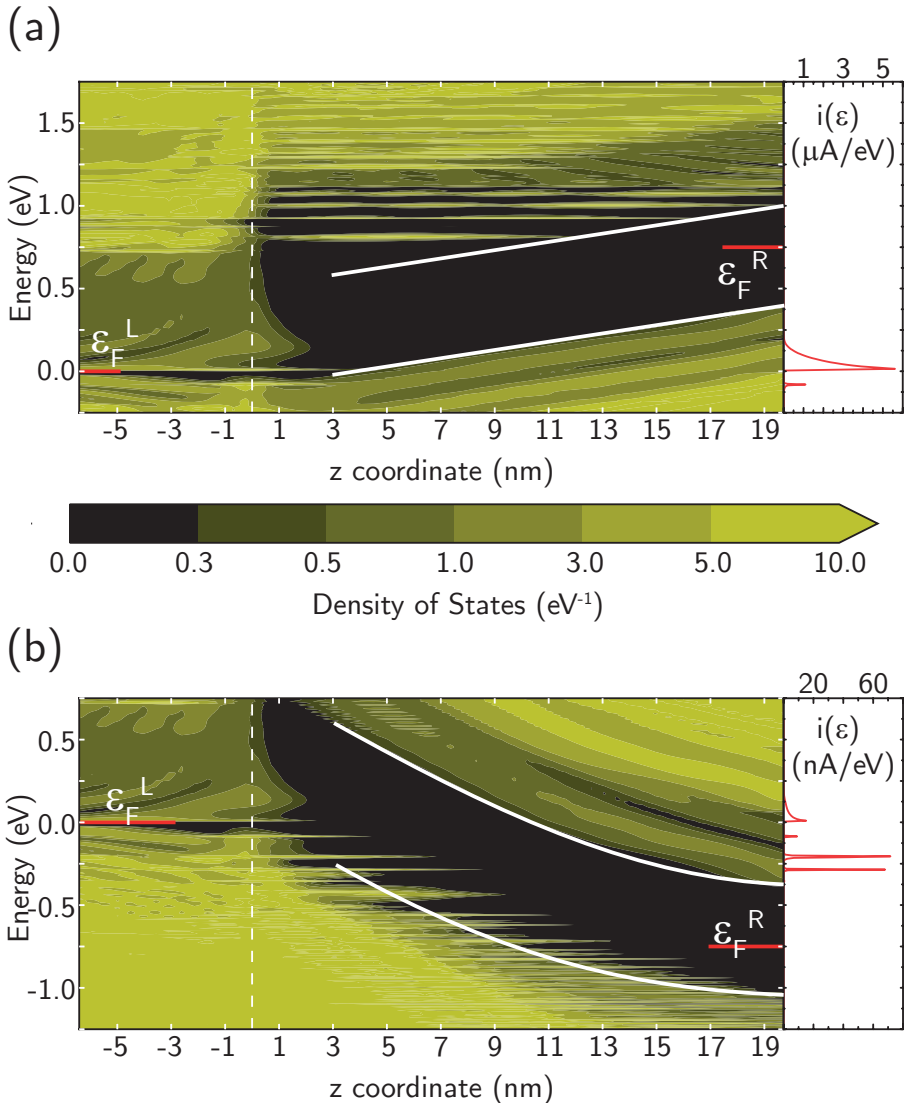

Figure 5.4: Local density of states (LDoS) and energy-resolved current for (a) Forward bias of +0.75 V. Note the quantization of states in the conduction band as a result of a triangular potential well-like profile near the junction; and (b) Reverse bias of -0.75 V. Red segments on each side of the LDoS plots indicate the quasi-Fermi level alignments in the semimetallic and semiconducting electrodes, ε_F^L and ε_F^R, respectively. Note the differences in vertical scales, particularly between the energy-resolved currents in (a) and (b).

usual Schottky diode formed with an *n*-type semiconductor which for forward bias conditions electrons readily tunnel from the doped semiconductor's conduction band to the metal as an applied voltage reduces the Schottky barrier.

Reversing the voltage polarity across the junction results in the electronic structure depicted in fig. 5.4(b). The semiconducting region becomes increasingly depleted of electrons with increasing reverse bias leading to an increase in band bending near the junction. In this case the quasi-Fermi level in the semicon-

ducting region ε_F^R is lower relative to quasi-Fermi level ε_F^L in the semimetallic region. As shown by the energy resolved current at the right in fig. 5.4(b), electron transport occurs through band-to-band tunneling (BTBT) whereby electrons from the semimetallic region *tunnel* through the junction barrier and into the semiconducting region's conduction band. The largest contributions to the energy resolved current are seen to correspond to MIGS extending into the band gap within the voltage bias window. The MIGS reduce the distance required for BTBT in the structure.

Figure 5.5(a) presents the calculated IV characteristic for the forward and reverse bias cases as self-consistently calculated within the NEGF formalism at a temperature of $\mathrm{T} = 300\mathrm{K}$. The asymmetry in the electron transport with the polarity of the applied voltage results in a two terminal rectifier or diode. Reverse bias leads to very low current limited by BTBT. In the forward direction, the increasing electric field across the junction increases coupling between the valence band edge in the semiconducting region and states near the quasi-Fermi level in the semimetallic region allowing a large current to flow for applied voltages $V_a >$ 0.6 V. The semi-log plot fig. 5.5(c) shows variations in the current density across the device when a voltage is applied in the forward (green) and reverse (red) directions: the largest rectification ratio (10^5) occurs at $|V_a|$ = 0.3 V and reduces with increasing applied bias as current in the reverse direction (tunnelling current) increases at a faster rate than in the forward direction with increasing voltage magnitude; while reverse current density increases three orders of magnitude in the -0.6 V $< V_a <$ -0.3 V range, forward current density remains on the order of 10^{-3} $\mathrm{A}/\mu\mathrm{m}^2$ in the corresponding forward bias range. Computed current density under forward bias is of the same order of magnitude as recently reported values for silver-silicon interfaces simulated employing a similar approach, where a doping concentration of 10^{18} $\mathrm{e}^-/\mathrm{cm}^3$ has been applied to the semiconductor side of that interface [26].

Notable in fig. 5.5(a) is a structure above approximately V_a =0.3 V extending to approximately V_a= 0.6 V. To explore this structure in the IV characteristic, transport across the junction at temperature $\mathrm{T} = 0\mathrm{K}$ was calculated and the plot in fig. 5.5(b) presents the difference between the currents obtained at room temperature and absolute zero. There are two predominant regions where the currents differ significantly: in the range $0.3V < V_a < 0.6V$ corresponding to the low current *step-like* structure in the IV characteristic and for $V_a > 0.6V$ where the diode is strongly *ON*. In fig. 5.3(b), the equilibrium (zero applied voltage) electronic structure for the junction is shown. At approximately $V_a = 0.3$ V, a

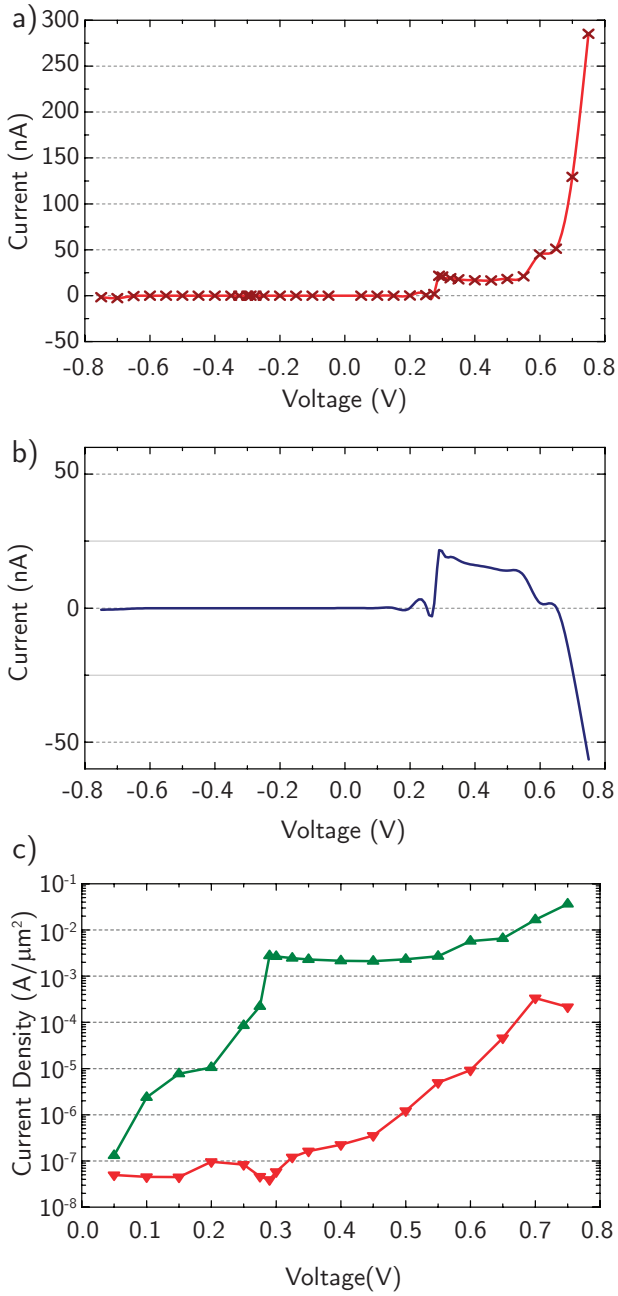

Figure 5.5: (a) Current-voltage characteristics of the junction at a temperature of 300K, (b) Difference between current-voltage characteristics at 300K and 0, and (c) semi-log plot of current density under forward bias (green) and reverse bias (red).

flat band condition is achieved in the semiconducting region when the valence band edge aligns to the semimetal quasi-Fermi level. At T=300K, electrons in the semimetal region are readily excited above the Fermi level providing partially filled states below ε_F^L into which the electrons from the semiconducting region's valence band maximum (VBM) can tunnel. The VBM provides an ideal conduction channel with transmission proportional to a one-dimensional den-

sity of states ($\propto 1/\sqrt{\epsilon}$) as reflected in the IV characteristic. At $\mathrm{T} = 0\mathrm{K}$, there is no thermal excitation of electrons in the semimetallic region and all states below the quasi-Fermi level are blocked resulting in lower currents at low temperatures as these states become only partially filled when thermally excited – Figure 5.5(b)(i).

At higher applied voltages, as depicted in fig. 5.4(a), the states above the quasi-Fermi level ε_F^L in the semimetallic region align to states in the semiconducting region's valence band. Electrons can then tunnel from the valence band in the semiconducting region into states which are unoccupied at T=0K. For T=300K, states above the quasi-Fermi level are partially blocked due to their thermal occupations. Hence tunneling into states with energies slightly higher than ε_F^L becomes reduced at higher temperatures. Therefore the overall current is smaller at T=300K relative to T=0 K for applied biases $V_a > 0.6V$– Figure 5.5(b)(ii). This property again reflects that the current transport mechanism for the surface modified semimetal junction in the present implementation is not identical to that of conventional Schottky diode designs due to the differing band alignments.

These results demonstrate that Schottky barriers can be formed in a *mono*material nanowire by exploiting the effects of quantum confinement and the impact of surface dipoles created by chemical terminating species of differing electronegativity. These two effects are of similar orders of magnitude in small cross section nanowires and can be manipulated to allow for semiconducting and semimetallic regions within a single nanowire or thin film. As highlighted, the effects predicted here from DFT calculations for small cross section nanowires are expected to occur for larger systems due to the band gap underestimation common in these electronic structure methods. The competing effects of quantum confinement and surface chemistry allow for the possibility to form a semimetal-semiconductor junction akin to Schottky barriers formed in metal-semiconductor junctions in larger dimension devices. The semiconducting region formed in a SnNW by quantum confinement in an ideal case (*i.e.* a highly crystalline, undoped semimetal) results in an intrinsic material and hence the band alignments are different to conventional Schottky barrier diodes. However, the rectifying properties of the surface modified semimetal diode are comparable to the properties of conventional macroscopic diodes, yet are achievable at molecular length scales and without the requirement for introducing doping in the nanostructures. These effects can be achieved in elemental semimetals such as Sn, Bi and As. Similarly, semimetallic alloys or small band

gap semiconductors can be engineered to have similar properties. A notable example is the tin germanium alloy which is predicted to become semimetallic with 25% to 30% Sn content. Although this composition is thermodynamically unstable in bulk, work is underway to increase the Sn content in tin germanium alloys when fabricated as nanostructures. [27] For sufficiently large alloy compositions, the extreme requirements for controlling dopant concentrations of 1 in 10^3 atoms or less is not relevant. Small fluctuations in alloy composition do not have as significant an effect for typical alloy composition ranges. To engineer a specific Schottky barrier height for a surface modified NW junction requires an understanding and balancing of the quantum confinement versus surface chemistry while taking into account the choice of material, diameter, crystal orientation, strain, and if appropriate, alloy composition.

5.2 Acknowledgements

This work was funded by Science Foundation Ireland through a Principal Investigator award Grant No. 13/IA/1956. ASS was supported by an Irish Research Council graduate fellowship. We acknowledge additional support from QuantumWise. Atomistic visualizations were rendered using VESTA [28]. The authors declare no competing financial interests.

References

[1] Brian Capozzi, Jianlong Xia, Olgun Adak, Emma J. Dell, Zhen-Fei Liu, Jeffrey C. Taylor, Jeffrey B. Neaton, Luis M. Campos, and Latha Venkataraman. Single-molecule diodes with high rectification ratios through environmental control. *Nat. Nanotechnol.*, 10:522–527, 2015.

[2] Arieh Aviram and Mark A. Ratner. Molecular rectifiers. *Chem. Phys. Lett.*, 29(2):277 – 283, 1974.

[3] Reiner M. Dreizler and Eberhard K.U. Gross. *Density functional theory: An approach to the quantum many-body problem*. Springer, Berlin, Germany, 1990.

[4] Mads Brandbyge, José-Luis Mozos, Pablo Ordejón, Jeremy Taylor, and Kurt Stokbro. Density-functional method for nonequilibrium electron transport. *Phys. Rev. B*, 65:165401, 2002.

[5] Lida Ansari, Giorgos Fagas, Jean-Pierre Colinge, and James C. Greer. A proposed confinement modulated gap nanowire transistor based on a metal (tin). *Nano Lett.*, 12(5):2222–2227, 2012.

[6] William Paul. Band structure of the intermetallic semiconductors from pressure experiments. *J. Appl. Phys.*, 32(10):2082–2094, 1961.

[7] R.F.C. Farrow, D.S. Robertson, G.M. Williams, A.G. Cullis, G.R. Jones, I.M. Young, and P.N.J. Dennis. The growth of metastable, heteroepitaxial films of α-Sn by metal beam epitaxy. *J. Cryst. Growth*, 54(3):507 – 518, 1981.

[8] H. Höchst and I. Hernández-Calderón. Angular resolved photoemission of InSb(001) and heteroepitaxial films of α-Sn(001). *Surf. Sci.*, 126(1):25 – 31, 1983.

[9] P. John, T. Miller, and T.-C. Chiang. Core-level photoemission studies of the α -Sn/InSb(100) heterostructure system. *Phys. Rev. B*, 39:3223–3229, 1989.

[10] B. H. Cheong and K. J. Chang. First-principles study of the structural properties of Sn under pressure. *Phys. Rev. B*, 44:4103–4108, 1991.

[11] Lars Hedin. New method for calculating the one-particle Green's function with application to the electron-gas problem. *Phys. Rev.*, 139:A796–A823, 1965.

[12] Alfonso Sanchez-Soares, Conor O'Donnell, and James C. Greer. Electronic structure tuning via surface modification in semimetallic nanowires. *Phys. Rev. B*, 94:235442, 2016.

[13] M. van Schilfgaarde, Takao Kotani, and S. Faleev. Quasiparticle self-consistent GW theory. *Phys. Rev. Lett.*, 96:226402, 2006.

[14] Fabien Tran and Peter Blaha. Accurate band gaps of semiconductors and insulators with a semilocal exchange-correlation potential. *Phys. Rev. Lett.*, 102:226401, 2009.

[15] Paul W. Leu, Bin Shan, and Kyeongjae Cho. Surface chemical control of the electronic structure of silicon nanowires: Density functional calculations. *Phys. Rev. B*, 73:195320, 2006.

[16] Michael Nolan, Sean O'Callaghan, Giorgos Fagas, James C. Greer, and Thomas Frauenheim. Silicon nanowire band gap modification. *Nano Lett.*, 7(1):34–38, 2007.

[17] José M Soler, Emilio Artacho, Julian D Gale, Alberto Garcia, Javier Junquera, Pablo Ordejon, and Daniel Sanchez-Portal. The SIESTA method for ab initio order-N materials simulation. *J. Phys.: Condens. Matter*, 14(11):2745, 2002.

[18] Atomistix ToolKit version 2015-1 QuantumWise A/S. *www.quantumwise.com (accessed August 2016)*.

[19] J.P. Perdew, K. Burke, and M. Ernzerhof. Generalized gradient approximation made simple. *Phys. Rev. Lett.*, 77:3865–3868, 1996.

[20] T. Ozaki. Variationally optimized atomic orbitals for large-scale electronic structures. *Phys. Rev. B*, 67:155108, 2003.

[21] T. Ozaki and H. Kino. Numerical atomic basis orbitals from H to Kr. *Phys. Rev. B*, 69:195113, 2004.

[22] I. Morrison, D.M. Bylander, and L. Kleinman. Non-local Hermitian norm-conserving Vanderbilt pseudopotenial. *Phys. Rev. B*, 47:6728–6731, 1993.

[23] John Bardeen. Surface states and rectification at a metal semi-conductor contact. *Phys. Rev.*, 71:717–727, 1947.

[24] Uzi Landman, Robert N. Barnett, Andrew G. Scherbakov, and Phaedon Avouris. Metal-semiconductor nanocontacts: Silicon nanowires. *Phys. Rev. Lett.*, 85:1958–1961, 2000.

[25] Supriyo Datta. Nanoscale device modeling: the Green's function method. *Superlattices Microstruct.*, 28(4):253 – 278, 2000.

[26] D. Stradi, U. Martinez, A. Blom, M. Brandbyge, and K. Stokbro. General atomistic approach for modeling metal-semiconductor interfaces using density functional theory and nonequilibrium Green's function. *Phys. Rev. B*, 93:155302, 2016.

[27] Michael S. Seifner, Felix Biegger, Alois Lugstein, Johannes Bernardi, and Sven Barth. Microwave-assisted $\mathrm{Ge_{1-x}Sn_x}$ nanowire synthesis: Precursor species and growth regimes. *Chem. Mater.*, 27(17):6125–6130, 2015.

[28] Koichi Momma and Fujio Izumi. *VESTA3* for three-dimensional visualization of crystal, volumetric and morphology data. *J. Appl. Crystallogr.*, 44(6):1272–1276, 2011.

Chapter 6

Conclusions

In this thesis we have presented theoretical studies exploring two of the present challenges associated with continuing downscaling of integrated circuit (IC) components designs currently employed in nanoelectronics: miniaturisation of transistors –the building blocks of logic gates– beyond the limits of planar CMOS designs, and concomitant scaling of the interconnect networks which link them together.

In chapters 2 and 3 we explored the electron transport properties of highly idealised single-crystal sub-10-nm Cu structures in order to assess their electronic transport properties and suitability for use in interconnect networks. At these dimensions the close proximity of surfaces in cross sectional directions means their chemical and structural details play a critical role in determining the electronic structure througout the nanostructures; the potential confining electrons into the Cu lines is severely influenced by the properties of sidewall surfaces resulting in transport properties which are strongly anisotropic (*i.e.* vary with crystallographic orientation) and dependent on structural and chemical interfacial parameters. In chapter 3 we compared the properties of sub-3-nm Cu nanowires (NWs) grown in vacuum without any surface passivation against those of structures passivated with essentially a 2D oxide wrapped around their surfaces; while surface oxidation was found to strongly suppress conduction paths along the surface which account for the largest contributions across the cross section of unpassivated NWs, orientation-dependent trends hold across both structure sets with $[110]$-oriented NWs exhibiting the largest transmission and those grown along $[111]$ the lowest in good agreement with other theoretical studies on unpassivated Cu NWs which report similar dependence with

orientation in structures with different cross-sectional shapes, aspect ratios, and areas up to 100 nm^2 [1–3].

The study on Cu thin films presented in chapter 2 further highlights the impact of local surface environments on electron transport along metallic nanostructures. Structures with two experimentally reported surface reconstructions with similar oxygen coverages corresponding to highly prepared thin film samples with exposed (100) and (110) facets were studied; in addition to orientation dependence of electron transport properties similar to that found in NWs, film conductance was found to strongly depend on the structural and chemical details of the surface environment for a fixed film thickness and transport orientation. Although passivation by surface oxides does not represent the situation encountered for Cu interconnect lines in ICs, the importance of engineering interfaces at the sidewalls of sub-10-nm interconnect lines which maximise conductivity is made evident.

A recent study by Hegde *et al.* [3] theoretically explored the lower limits of Cu lines resistivities concluding that structures achievable with present damascene fabrication methods would not be able to fulfil the ITRS projected resistivity requirements for lines with characteristic cross sectional dimensions below 10 nm, even with generous assumptions such as neglecting inelastic scattering events (*i.e.*, electron-phonon scattering), assuming bulk-like intrinsic mean-free-paths and no surface passivation. Under such assumptions they report that inclusion of experimentally reported *bamboo*-like grain domains (*i.e.*, grain domains of roughly the same size as the line's width) into their model dramatically increases the line resistivity by a factor of up to 20. Theoretical simulations of *bamboo*-like Cu lines with linewidths ranging from 2 nm to 10 and tantalum surface coverages based on DFTB methods, as well as experimental studies on Cu lines with 10-20 nm characteristic cross-sectional dimensions and the aforementioned grain size distribution agree that grain boundary scattering and scattering off sidewalls (*interface* scattering) dominate resistivity at these dimensions, concluding that improvement in line resistivity should focus on minimising the impact of grain and surfaces [4, 5].

The fact that resistivity in ultra-thin lines is dominated by electron scattering off interfaces means material-specific *bulk resistivity* contributions become less important as linewidth scales down. This has lead to recent experimental studies comparing the electrical and reliability performance of Cu lines with that of other metals conclude that sub-10-nm structures based on metals with larger bulk

resistivities and higher melting points can deliver competitive line resistances while exhibiting improved reliability in terms of *electromigration* [6]. Inclusion of realistic grain boundary and liner interfaces into atomistic computational simulations requires much larger computational effort when compared to pristine single-crystalline structures, and thus require the use of semi-empirical methods such as density-functional tight binding (DFTB) –employed and benchmarked against *ab-initio* density functional theory in chapter 2–, tight binding [7], and extended-Hückel methods [8]. Development of higher-level theoretical models which allow predicting the resistivity of sub-20-nm metallic lines by applying the results and insight obtained through atomistic simulations of electron scattering properties of interfaces and grains boundaries will provide valuable guidelines for the fabrication of interconnect lines suitable for next-generation ICs.

Building on the concept of exploiting the confinement-modulatable electronic character of semimetal nanostructures for designing rectifying interfaces –and ultimately logic gates–, we explored the dependence of the semimetal-semiconductor transition in α-Sn NWs with varying chemical species as surface passivants in chapter 4. We have found that the cross sectional dimensions at which the transition in electronic character occurs can be tuned by essentially modifying the potential inside the NW structures through variations in surface chemistry. Cross sectional potential profile variations resulting from the interplay between semimetal NW cores with different structural parameters (*i.e.*, orientation and exposed surface facets) and passivation of surface bonds with chemical groups of varying electronegativity impacts the shape and depth of the potential well confining electrons inside the NW, which in turn can modify the ordering in energy and separation between energy levels, including the magnitude of the electronic band gap and thus impacting the dimensions at which the semimetal-to-semiconductor transition occurs. We report that in addition to the possibility of designing rectifying interfaces by modulating cross sectional dimensions, variations in surface chemistry can induce effects of the same order of magnitude allowing further control of the electronic structure character in semimetal NWs. Appropriate choice of structural parameters and passivating species allows counteraction of quantum confinement induced band gaps enabling the design of sub-10-nm rectifying junctions without the need to vary the structural parameters or chemical composition of the NW core, as demonstrated in chapter 5.

Recently an important milestone in this direction has been reported with the first experimental realisation of a rectifying monomaterial junction which ope-

rates at room temperature [9]. In their work, a semimetal-semiconductor junction is fabricated by varying the thickness along the length of a single bismuth thin film sample and thus achieving a monomaterial device with semimetallic region (*thicker* than a threshold dimension) and a semiconducting region (*thinner* than a threshold dimension) which exhibits current rectification characteristics even at room temperature, demonstrating that quantum confinement effects can be harnessed in sub-10-nm structures based on semimetals in order to mimic the operation of macroscopic electronic components. The path from these theoretical and proof-of-concept experimental demonstrations towards commercially viable interfaces and devices will require engineering and material science efforts by exploration of the range of properties which can be obtained from semimetals and semimetallic alloys such as SnGe, as discussed in chapter 5. By combining the effects of varying cross-sectional sizes, surface coverages, strain, and alloy compositions the engineering of monomaterial devices has the potential to become a competitive technology in the near future.

With the impending end of traditional (*i.e., More Moore*) IC component scaling due to increasing technical difficulties, costs, and fundamental limits associated with continuing miniaturisation of current production designs, the search for suitable alternatives which rival the performance of present technology is currently one of the most important issues in the field of nanoelectronics. While a number of alternatives for logic devices are currently under investigation, structural advantages offered by nanowire-based transistors make them one of the most viable choices for near-future technologies allowing designs with smaller cross sections, shorter channel lengths, and higher packing densities via 3D integration whilst maintaining electronic charge as state-variable and the potential to use materials which are familiar to the semiconductor industry provides important advantages in terms of integrability with existing processes.

The findings presented in this thesis show that Nobel laureate Herbert Kroemer's coined phrase *the interface is the device* holds true now more than ever [10]. With device dimensions reducing to merely a few thousand atoms, the focus is shifted away from the properties of materials as interfaces play an increasingly important role and their effects cannot be either neglected nor decoupled from the behaviour of any of the device regions or from contact effects [11, 12]. In interconnect networks, the bulk conductivity of the employed material becomes less critical as cross sectional areas scale down and interface properties become key in optimising electrical performance; whilst in active device design we have expanded on novel ways of implementing monomaterial

rectifying interfaces in semimetal nanostructures through exploitation of surface chemistry and geometry effects for the design of sub-10-nm diodes and transistors without the need to introduce heterojunctions along transport directions or the inclusion of dopants, which represent fabrication challenges at small dimensions. It is therefore essential that next-generation devices are designed by careful engineering of all interfaces involved in their operation. The development of theoretical models for efficient and accurate exploration of materials and interface properties in synergy with advances in experimental and fabrication methods will enable the realisation of solutions which rival present technologies.

References

[1] Ganesh Hegde, Michael Povolotskyi, Tillmann Kubis, Timothy Boykin, and Gerhard Klimeck. An environment-dependent semi-empirical tight binding model suitable for electron transport in bulk metals, metal alloys, metallic interfaces, and metallic nanostructures. I. model and validation. *J. Appl. Phys.*, 115(12):123703, 2014.

[2] Ganesh Hegde, Michael Povolotskyi, Tillmann Kubis, James Charles, and Gerhard Klimeck. An environment-dependent semi-empirical tight binding model suitable for electron transport in bulk metals, metal alloys, metallic interfaces, and metallic nanostructures. II. application—effect of quantum confinement and homogeneous strain on Cu conductance. *J. Appl. Phys.*, 115(12):123704, 2014.

[3] Ganesh Hegde, R. Chris Bowen, and Mark S. Rodder. Lower limits of line resistance in nanocrystalline back end of line Cu interconnects. *Appl. Phys. Lett.*, 109(19):193106, 2016.

[4] Jeanette M. Roberts, Ananth P. Kaushik, and James S. Clarke. Resistivity of sub-30 nm copper lines. In *2015 IEEE International Interconnect Technology Conference and 2015 IEEE Materials for Advanced Metallization Conference (IITC/MAM)*. Institute of Electrical and Electronics Engineers (IEEE), 2015.

[5] A. Pyzyna, R. Bruce, M. Lofaro, H. Tsai, C. Witt, L. Gignac, M. Brink, M. Guillorn, G. Fritz, H. Miyazoe, D. Klaus, E. Joseph, K. P. Rodbell, C. Lavoie, and D.-G. Park. Resistivity of copper interconnects beyond the 7 nm node. In *2015 Symposium on VLSI Technology (VLSI Technology)*. Institute of Electrical and Electronics Engineers (IEEE), 2015.

[6] J. S. Chawla, S. H. Sung, S. A. Bojarski, C. T. Carver, M. Chandhok, R. V. Chebiam, J. S. Clarke, M. Harmes, C. J. Jezewski, M. J. Kobrinski, B. J.

Krist, M. Mayeh, R. Turkot, and H. J. Yoo. Resistance and electromigration performance of 6 nm wires. In *2016 IEEE International Interconnect Technology Conference / Advanced Metallization Conference (IITC/AMC)*. Institute of Electrical and Electronics Engineers (IEEE), 2016.

[7] J. C. Slater and G. F. Koster. Simplified LCAO method for the periodic potential problem. *Phys. Rev.*, 94:1498–1524, 1954.

[8] Roald Hoffmann. An extended Hückel theory. I. hydrocarbons. *J. Chem. Phys.*, 39(6):1397, 1963.

[9] Farzan Gity, Lida Ansari, Martin Lanius, Peter Schüffelgen, Gregor Mussler, Detlev Grützmacher, and James C. Greer. Reinventing solid state electronics: Harnessing quantum confinement in bismuth thin films. *arXiv:1609.05332*, 2016.

[10] Herbert Kroemer. Quasi-electric fields and band offsets: teaching electrons new tricks. *Nobel Lecture*, 2000.

[11] Anders Blom and Kurt Stokbro. Atomistic modeling of semiconductor interfaces. *J. Comput. Electron.*, 12(4):623–637, 2013.

[12] J. Appenzeller, J. Knoch, M. T. Bjork, H. Riel, H. Schmid, and W. Riess. Toward nanowire electronics. *IEEE Trans. Electron Devices*, 55(11):2827–2845, 2008.

Appendix A

Bulk properties of studied materials

In this appendix we present a brief introduction to the materials in which we have based the nanostructures studied throughout this thesis: copper and α-tin. We shall briefly discuss some their most relevant structural and electronic properties when in their bulk forms, their applications, and motivate their use in the studies presented in previous chapters.

A.1 Copper

Copper is a chemical element of group 11 in the periodic table. As such, it is considered a transition metal and is characterised by an electronic configuration with one s-orbital electron on top of a filled d-electron subshell. At normal temperature and pressure conditions ($\mathrm{T} = 20^{\circ}\mathrm{C}$, $\mathrm{P} = 1$ atm) it is a crystalline solid exhibiting a face-centered cubic (fcc) structure, as shown in fig. A.1. Named after the island of Cyprus, where much copper was mined in Roman times, copper is found as a pure metal in nature and has been in use for around ten thousand years. It was the first metal to be smelted from its ore, to be cast into shape in molds, and a main component of the first purposefully created metallic alloy: bronze [1].

Copper is a highly ductile metal exhibiting high electrical and thermal conductivities, with silver being the only pure metal with higher conductivities at room temperature. It is the most widely used electrical conductor being present in

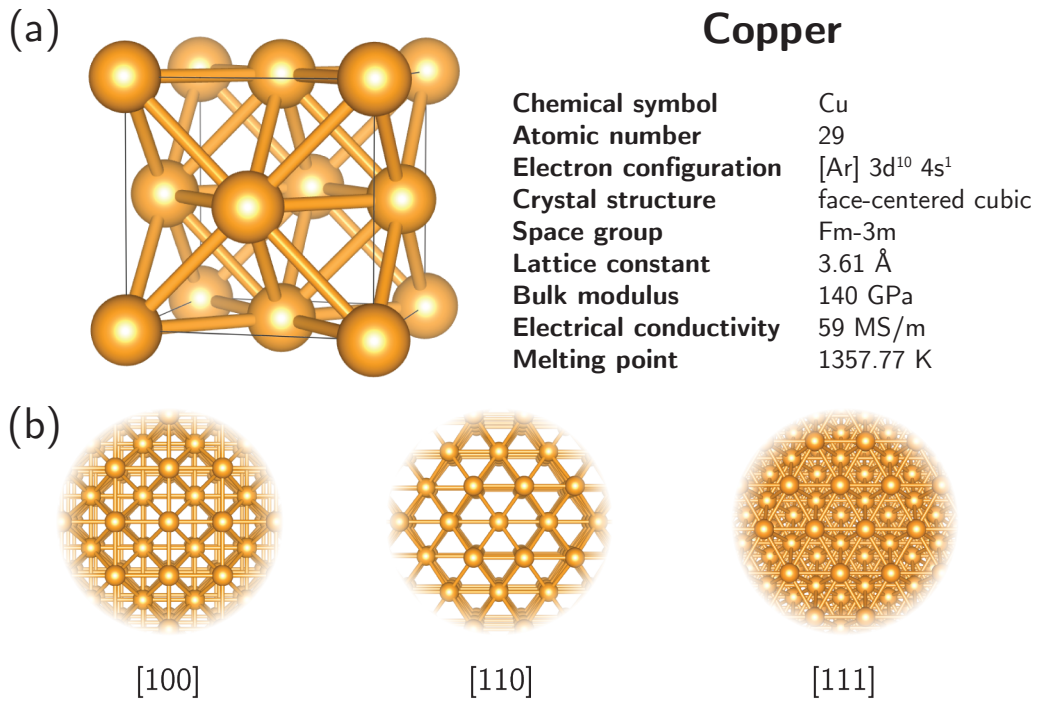

Figure A.1: Atomistic Illustrations of the crystal structure of fcc copper: (a) a conventional unit cell and (b) views from the [100], [110], and [111] crystallographic directions of its corresponding primitive cell.

virtually all electrical applications from power generation to telecommunications and electronic circuitry. In particular, the semiconductor industry has been employing copper for interconnect networks within integrated circuits for almost 20 years, and is thus our material of choice for studying the conductivity of nanoscale conductors. Figure A.1(a) shows an illustration of copper's fcc structure, after which we have modelled the structures presented in chapters 2 and 3 and studied electron transport in confined systems oriented along the crystallographic directions shown in fig. A.1(b).

Figure A.2 shows the electronic band structure and the Fermi surface of fcc copper. As characteristic for metals, the band structure exhibits half-filled bands crossing the Fermi level. The Fermi surface in fig. A.2(b) provides a visual representation of the density of states at the Fermi level in reciprocal space. Its most prominent feature is its vanishing density of states along $\Gamma \rightarrow L$ paths –associated with $\langle 111 \rangle$ crystallographic directions– which is related to the fact that the electronic band structure shows no bands crossing the Fermi level along $\Gamma \rightarrow L$, as seen in fig. A.1(a). For an in-depth discussion on the electronic structure and Fermi surface of bulk copper, see ref. [2].

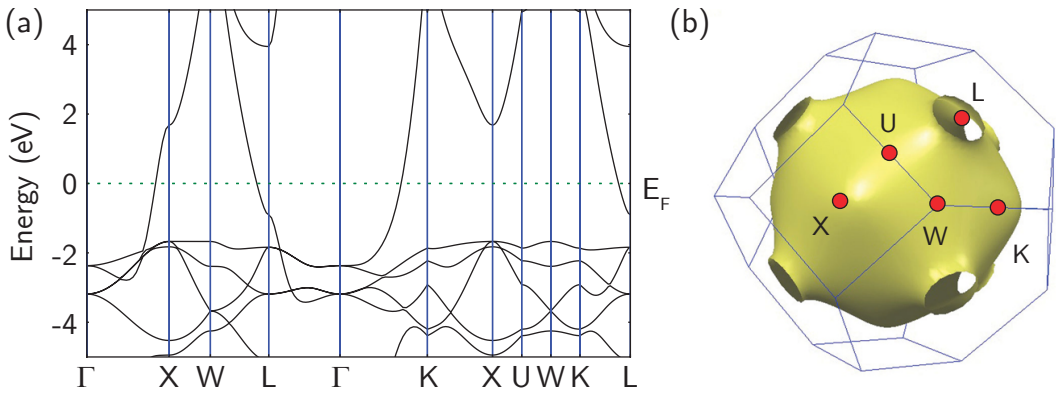

Figure A.2: (a) Electronic band structure and (b) Fermi surface of crystalline copper. The Fermi surface is represented inside the Brillouin zone, and the red dots indicate high symmetry points along which the electronic band structure is plotted. The zero of energy in (a) has been taken to be the Fermi level $\mathrm{E_F}$. Fermi surface illustration reproduced from [3].

A.2 Tin (α)

Tin is a chemical element of group 14 in the periodic table. It is considered a post-transition metal and is characterised by an electronic configuration with two s-orbital and two p-orbital electrons in its last shell, same as other elements in the same group such as silicon or germanium. It has two main allotropes: β-tin, a silvery white malleable metal, and α-tin, a brittle gray semimetal which is only stable at temperatures below $13.2^{\circ}\mathrm{C}$ in bulk form. It has been in use for around five thousand years and was alloyed with copper to produce bronze long before pure tin was itself isolated [4]. Tin is a superconductor at temperatures below 3.72 K [5] and was one of the first superconductors to be studied; one of the characteristic features of superconductors –the Meissner effect– was first discovered in superconducting tin crystals [6].

Presently, tin is widely used in combination with other materials in food preservation, soldering, in alloys such as pewter and bronze, and in semiconductor processing, where it has been employed as a dopant in order to improve device performance for the last few years. Although not stable in bulk at room temperature, tin's α phase can be stabilised in nanostructures [7–10] and has been the subject of recent studies for applications in nanoelectronics and lithium-ion batteries [11–14]. α-tin's semimetallic character is modified into semiconducting when nanopatterned below a certain threshold dimension of the order of a few nanometer, in a similar fashion to observed *band gap widening* in semiconductor nanostructures [15]. Recent studies have explored exploitation of this

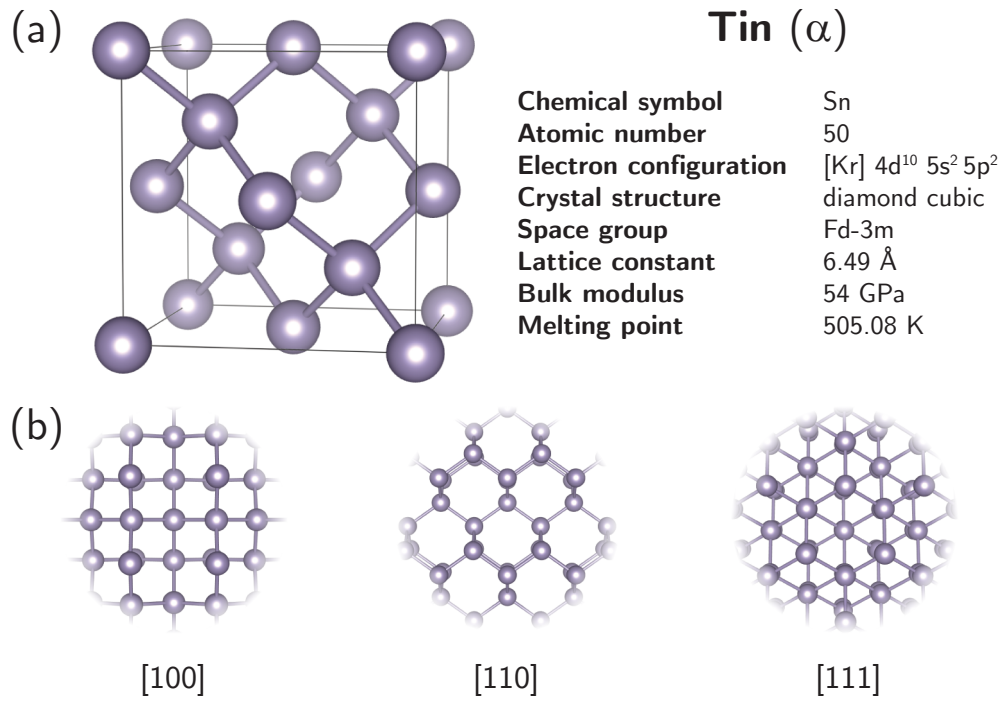

Figure A.3: Atomistic Illustrations of the crystal structure of α-tin: (a) a conventional unit cell and (b) views from the $[100]$, $[110]$, and $[111]$ crystallographic directions of its corresponding primitive cell.

property of semimetals for the design of nanoscale electronic devices [11, 16]. α-tin comprises a structurally and chemically simple semimetal which makes it particularly suitable for theoretical atomistic studies of the semimetal-to-semiconductor transition and its applications in nanotechnology.

Figure A.3(a) illustrates α-tin's diamond cubic structure, while fig. A.3(b) shows views along the $[100]$, $[110]$, and $[111]$ crystallographic directions in which we have based the the structures studied in chapters 4 and 5. α-tin's electronic band structure, shown in fig. A.4(a), exhibits well-defined valence and conduction bands similarly to semiconductors such as silicon or germanium although both bands are degenerate at the Fermi level at Γ; α-tin is thus considered a *zero-band gap* semimetal. Its low density of states in the vicinity of the Fermi level translates into a material which, like metals, conducts electricity, but exhibits a much lower conductivity. For an in-depth discussion on the electronic structure of bulk α- and β-tin, see ref. [17].

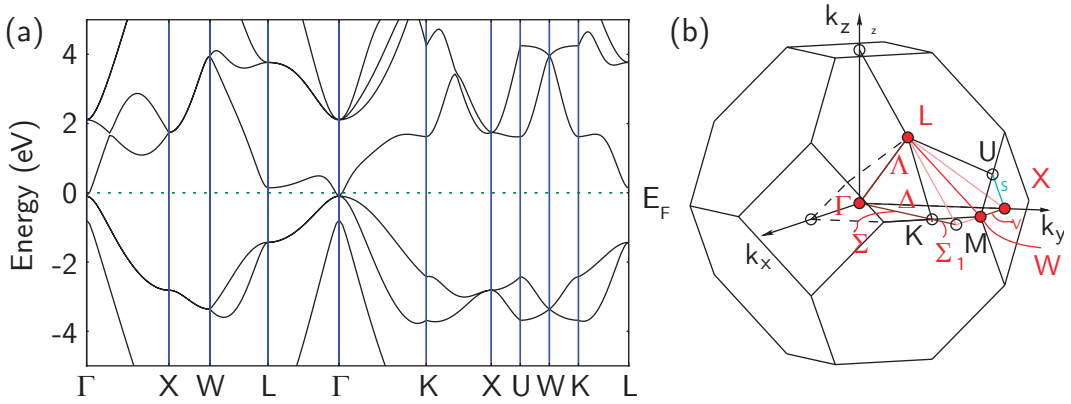

Figure A.4: (a) Electronic band structure and (b) first Brillouin zone of crystalline α-tin. The high-symmetry points along which the band structure is plotted are indicated in the Brillouin zone. The zero of energy in (a) has been taken to be the Fermi level $\mathrm{E_F}$.

References

[1] Copper. *https://en.wikipedia.org/wiki/Copper and references therein (Accessed December 2016)*.

[2] Benjamin Segall. Fermi surface and energy bands of copper. *Phys. Rev.*, 125:109–122, 1962.

[3] Emergent behavior in quantum matter. *https://www.learner.org/courses/physics/unit/text.html?unit=8&secNum=2 (Accessed December 2016)*.

[4] Tin. *https://en.wikipedia.org/wiki/Tin and references therein (Accessed December 2016)*.

[5] W.J. De Haas, J. De Boer, and G.J. Van den Berg. The electrical resistance of cadmium, thallium and tin at low temperatures. *Physica*, 2(1-12):453–459, 1935.

[6] W. Meissner and R. Ochsenfeld. Ein neuer effekt bei eintritt der supraleitfähigkeit (*A new effect on superconductivity*). *Naturwissenschaften*, 21(44):787–788, 1933.

[7] R.F.C. Farrow, D.S. Robertson, G.M. Williams, A.G. Cullis, G.R. Jones, I.M. Young, and P.N.J. Dennis. The growth of metastable, heteroepitaxial films of α-Sn by metal beam epitaxy. *J. Cryst. Growth*, 54(3):507 – 518, 1981.

[8] H. Höchst and I. Hernández-Calderón. Angular resolved photoemission of InSb(001) and heteroepitaxial films of α-Sn(001). *Surf. Sci.*, 126(1):25 – 31, 1983.

[9] P. John, T. Miller, and T.-C. Chiang. Core-level photoemission studies of the α -Sn/InSb(100) heterostructure system. *Phys. Rev. B*, 39:3223–3229, 1989.

[10] Kazuyuki Ueda, Hiroshi Nakayama, Makoto Sekine, and Hiroshi Fujita. Auger valence electron spectroscopy of a structural phase transformation in metastable alpha-Sn grown on InSb (001). *Vacuum*, 42(8):547 – 553, 1991.

[11] Lida Ansari, Giorgos Fagas, Jean-Pierre Colinge, and James C. Greer. A proposed confinement modulated gap nanowire transistor based on a metal (tin). *Nano Lett.*, 12(5):2222–2227, 2012.

[12] Hyung Soon Im, Yong Jae Cho, Young Rok Lim, Chan Su Jung, Dong Myung Jang, Jeunghee Park, Fazel Shojaei, and Hong Seok Kang. Phase evolution of tin nanocrystals in lithium ion batteries. *ACS Nano*, 7(12):11103–11111, 2013.

[13] Sebastian Küfner, Jürgen Furthmüller, Lars Matthes, Martin Fitzner, and Friedhelm Bechstedt. Structural and electronic properties of α-tin nanocrystals from first principles. *Phys. Rev. B*, 87:235307, 2013.

[14] N. Oehl, L. Hardenberg, M. Knipper, J. Kolny-Olesiak, J. Parisi, and T. Plaggenborg. Critical size for the β- to α-transformation in tin nanoparticles after lithium insertion and extraction. *CrystEngComm*, 17:3695–3700, 2015.

[15] Jean-Pierre Colinge and James C. Greer. *Nanowire Transistors: Physics of devices and materials in one dimension*. Cambridge University Press, Cambridge CB2 8BS, United Kingdom, 2016.

[16] Farzan Gity, Lida Ansari, Martin Lanius, Peter Schüffelgen, Gregor Mussler, Detlev Grützmacher, and James C. Greer. Reinventing solid state electronics: Harnessing quantum confinement in bismuth thin films. *arXiv:1609.05332*, 2016.

[17] Fleur Legrain and Sergei Manzhos. Understanding the difference in cohesive energies between alpha and beta tin in DFT calculations. *AIP Adv.*, 6(4):045116, 2016.

Appendix B

Electronic structure and electronic transport methods: a brief overview

We present here a brief overview outlining the theoretical framework in which the work presented in this thesis has been carried out. In the following sections we present the methods employed for computing the electronic structure and electron transport properties of the systems studied in previous chapters. This appendix is not intended to be a comprehensive review on the theory and implementations, but rather a quick guide (i) pointing out the most relevant approximations so the reader can get a quick sense of the theoretical framework in which to interpret the presented results, as well as (ii) providing references in which detailed information can be consulted.

B.1 Electronic structure methods

B.1.1 Density functional theory

Density functional theory (DFT) constitutes one of the greatest achievements of physics during the twentieth century. Its success derives from its ability of make qualitative and quantitative predictions about many of the properties of matter *ab-initio* (*i.e.*, without experimental input). This allows accessing properties which are difficult to measure experimentally, modelling materials that have

not yet been grown due to experimental difficulties or for which high-quality samples are not available, and offering insight into experimental results. For a comprehensive review on the theory, see refs. [1–4].

Based on the theorems of Hohenberg and Kohn [5] which establish a unique correspondence between the ground-state electronic density of a system and its external potential, DFT allows casting the complicated many-body problem of an arbitrary number of interacting electrons in terms of a variational electronic density. Once obtained, the ground-state electronic density $n_0(\mathbf{r})$ completely determines all properties of the ground-state of the many-electron system and allows calculating the expectation value of any observable. Following Martin's notation [3], the Hamiltonian of a non-relativistic system constituted by an arbitrary number of interacting electrons and nuclei can be written as:

$$\hat{H} = \hat{T} + \hat{V}_{ext} + \hat{V}_{int} + \hat{T}_{nuc} + E_{II}, \tag{B.1}$$

where $\hat{T}$ is the kinetic operator for electrons, $\hat{V}_{ext}$ the attractive electrostatic potential acting on electrons due to the nuclei, $\hat{V}_{int}$ the repulsive electron-electron electrostatic interaction, $\hat{T}_{nuc}$ the kinetic operator of the nuclei, and E_{II} the repulsive nucleus-nucleus interaction. By separating electronic and nuclear degrees of freedom as per the Born-Oppenheimer approximation [6], we may write the electronic total energy as a functional of the electronic density $n(\mathbf{r})$ which only depends on the nuclear degrees of freedom parametrically as

$$\begin{aligned} E[n] = \langle \psi[n] | \, \hat{H} \, | \psi[n] \rangle \equiv \langle \hat{H} \rangle = \langle \hat{T} + \hat{V}_{ext} + \hat{V}_{int} \rangle = \\ = \langle \hat{T} + \hat{V}_{int} \rangle + \langle \hat{V}_{ext} \rangle = F_{HK}[n] + \langle \hat{V}_{ext} \rangle \, , \end{aligned} \tag{B.2}$$

where we have neglected the term inversely proportional of the nuclear masses $\hat{T}_{nuc} \propto M_I^{-1}$, and the nuclear-nuclear electrostatic interaction E_{II} as its contribution is constant for a given set of nuclear coordinates and only relevant for geometry optimisation calculations. The functional F_{HK} is *universal* (*i.e.*, it is the same for all systems of interacting electrons such as atoms, molecules, and solids) in the sense that it does not depend on interactions with the nuclei, which are contained in $\hat{V}_{ext}$. Unfortunately, calculating $\langle \hat{V}_{ext} \rangle$ is one of the main difficulties in DFT as the quantum-mechanical nature of electrons means one cannot simply calculate a space integral involving the electronic charge den-

sity, as would be the case with a classical charge distribution. Over time, this *exact* theory has been extended to include many cases of interest such as spin-polarised systems, finite temperature ensembles, electric fields and polarisation, and has even been extended to include a system's response to an external perturbation in its time-dependent formalism [7].

While the DFT formalism comprises an exact and attractive approach, it does not provide an explicit formulation. The *ansatz* of Kohn and Sham [8], which provides a practical way of computing a system's properties by introducing an auxiliary *non-interacting* system of electrons, is largely responsible for the present widespread use of DFT as it provides an explicit set of equations for practical usage. In their work, they propose an independent-particle approach by which the total density is given by a set of independent wave functions or *orbitals* $|\phi_i\rangle$:

$$n(\mathbf{r}) = \sum_i |\phi_i|^2, \tag{B.3}$$

where i runs over all occupied states. In the Kohn-Sham (KS) formalism we may write the electronic ground-state energy functional, in atomic units, as

$$E_{KS}[n] = \underbrace{-\frac{1}{2}\sum_i \langle\phi_i|\nabla^2|\phi_i\rangle}_{T_{KS}[n]} + \underbrace{\frac{1}{2}\int d\mathbf{r}d\mathbf{r}'\frac{n(\mathbf{r})n(\mathbf{r}')}{|\mathbf{r}-\mathbf{r}'|}}_{E_{Hartree}[n]} + \int d\mathbf{r}V_{ext}(\mathbf{r})n(\mathbf{r}) + E_{xc}[n], \tag{B.4}$$

where T_{KS} gives the independent-particle kinetic energy, $E_{Hartree}[n]$ the classical electrostatic interaction energy of the electronic charge distribution interacting with itself, and all of the many-body, exchange and correlation effects are swept under the last term

$$E_{xc}[n] = (\langle\hat{T}\rangle - T_{KS}[n]) + (\langle\hat{V}_{int}\rangle - E_{Hartree}[n]), \tag{B.5}$$

which is defined as the difference of the kinetic and internal interaction energies between the true interacting system and the KS auxiliary system. By applying a variational principle to E_{KS} and imposing some physical constraints, one arrives at the Kohn-Sham equations

$$\begin{aligned}
&\hat{H}_{KS}\left|\phi_i\right\rangle = \epsilon_i\left|\phi_i\right\rangle \\
&\hat{H}_{KS} = -\frac{1}{2}\nabla^2 + \hat{V}_{KS} \\
&\hat{V}_{KS} = \hat{V}_{ext} + \underbrace{\frac{\delta E_{Hartree}}{\delta n(\mathbf{r})}}_{\hat{V}_{Hartree}} + \underbrace{\frac{\delta E_{xc}}{\delta n(\mathbf{r})}}_{\hat{V}_{xc}},
\end{aligned} \tag{B.6}$$

which have the form of independent-particle equations with an *effective* potential that must be solved self-consistently with the resulting density. Since there is no known exact functional for $E_{xc}[n]$, in practice the accuracy of the method is limited by the chosen approximation for this *exchange-correlation functional*. Perdew and collaborators developed a sequence of approximations called *Jacob's ladder*, where each *rung* builds on the experience of lower levels and yields improved accuracy by incorporating more complicated ingredients into the functional [9]. Throughout this thesis we have mainly employed the Perdew-Burke-Erzenhof (PBE) [10] formulation of the generalised gradient approximation (GGA) by which the $E_{xc}[n]$ contribution at each point in space is derived from the homogeneous electron gas (HEG) results and depends on the value of the density and the magnitude of its gradient. In chapter 5, we have additionally employed the more complex meta-GGA form of Tran and Blaha [11], which also incorporates the kinetic energy density of the KS orbitals into the functional.

Of particular relevance is a fundamental limitation of the KS theory by which eigenvalues resulting from eq. (B.6) do *not* yield correct energy differences between the highest occupied and lowest unoccupied states due to a discontinuity of the functional derivative of the exchange-correlation functional with respect to the number of electrons in the system [12–14]. We have hence improved our description of computed band gaps in semiconducting nanostructures in chapters 4 and 5 by means of a perturbative many-body approach within the GW approximation [see appendix B.1.2].

The results presented in this thesis have been obtained through computational studies carried out with the OPENMX [15] and QUANTUMWISE [16] software packages, which implement Kohn-Sham DFT in the context of pseudopotential theory [17] and employ localised pseudo-atomic orbitals [18] basis sets for expanding KS orbitals. In chapters 4 and 5 we additionally present studies car-

ried out with the QUANTUMESPRESSO [19] software package, which employs plane-waves as a basis set for expanding KS orbitals. More details on the implementations can be found in refs. [18,20–24]. For a recent assessment on the accuracy and reproducibility of DFT calculations which includes the implementations used in this work see ref. [25].

B.1.2 Quasiparticles and the GW approximation

In spite of the success of Kohn-Sham DFT (KS-DFT) as a ground-state theory, it is unable to describe phenomena that involves excited states. In particular, its failure to accurately predic electronic band gaps has been recognised since its early stages [12,26]. The so called *band gap problem* [27] has been widely studied over the past decades and a rigorous theoretical framework for exploring excited-state properties based on many-body Green's functions has been developed. For a comprehensive review of the theory and its application to electron systems see refs. [28–30].

An electronic system's response to a perturbation which drives it away from its ground state is not correctly described by the independent-particle picture of KS-DFT. In particular, it does not capture the physics involved in processes in which electrons are added or removed from the system, such as those probed when measuring optical or electrical band gaps. The presence of an extra electron (or *hole*) modifies the electronic structure of the system in a way which is better described by the concept of *quasiparticles* derived from the Fermi liquid theory [31–34]. These quasiparticle states are excitations of the interacting system corresponding to the creation or annihilation or electrons and allow a formalism which retains the picture of one-particle energy levels following

$$\underbrace{[-\frac{1}{2}\nabla^2(\mathbf{r}) + V_{Hartree}(\mathbf{r})]}_{H_0(\mathbf{r})}\Psi_i(\mathbf{r},\omega) + \int d\mathbf{r}\Sigma(\mathbf{r},\mathbf{r}';\omega)\Psi_i(\mathbf{r},\omega) = E_i(\omega)\Psi_i(\mathbf{r},\omega), \tag{B.7}$$

where $\hat{H}_0$ is the Hamiltonian corresponding to the non-interacting system – which does not contain any exchange-correlation effects–, Ψ_i are the quasiparticle wavefunctions and E_i their corresponding energy levels, and $\hat{\Sigma}$ is the non-local, energy dependent, non-Hermitian self-energy operator which incorporates all exchange and correlation effects. Equation (B.7) may be solved

using a Green's function approach [28, 35] as

$$[\omega - H_0(\mathbf{r})]G(\mathbf{r},\mathbf{r}';\omega) - \int d\mathbf{r}''\Sigma(\mathbf{r},\mathbf{r}'';\omega)G(\mathbf{r}'',\mathbf{r}';\omega) = \delta(\mathbf{r}-\mathbf{r}') \tag{B.8}$$

with the Green's function G constructed as

$$G(\mathbf{r},\mathbf{r}';\omega) = \sum_i \frac{\Psi_i(\mathbf{r},\omega)\Psi_i^\dagger(\mathbf{r}',\omega)}{\omega - E_i(\omega)}, \tag{B.9}$$

which when Fourier transformed into the time domain can be written as [34]:

$$iG(\mathbf{r},\mathbf{r}';t,t') = \langle N|T[\hat{\zeta}(\mathbf{r},t)\hat{\zeta}^\dagger((\mathbf{r}',t'))]|N\rangle\,, \tag{B.10}$$

where $|N\rangle$ is the exact N-electron ground state, $\hat{\zeta}(\mathbf{r})$ is a field operator which annihilates an electron at $(\mathbf{r},t)$, and T is the time-ordering operator. Therefore G may be interpreted for $t > t'$ ($t' > t$) as the probability amplitude that an electron (hole) added at $(\mathbf{r},t)$ will propagate to $(\mathbf{r}',t')$ [28]. The Green's function formalism is thus able to correctly describe processes involving excited states through a *single-quasiparticle* excitation spectrum.

We may hence improve our DFT description of electronic band gaps by means of a perturbative approach starting from Kohn-Sham eigenvalues and wavefunctions. By approximating the quasiparticle wavefunctions Ψ_i by KS orbitals ϕ_i we have that

$$\begin{aligned} \text{Perturbative } GW\text{: } & \langle\phi_i|[\hat{H}_0 + \hat{\Sigma}]|\phi_i\rangle \simeq E_i \\ \text{Kohn-Sham DFT: } & \langle\phi_i|[\hat{H}_0 + \hat{V}_{xc}]|\phi_i\rangle = \epsilon_i, \end{aligned} \tag{B.11}$$

where $\hat{V}_{xc}$ and ϵ_i are the KS-DFT exchange-correlation potential and eigenvalues, respectively. We may then calculate corrections to KS eigenvalues as

$$\Delta E_i = E_i - \epsilon_i = \langle\phi_i|[\hat{\Sigma}(E_i) - \hat{V}_{xc}]|\phi_i\rangle\,, \tag{B.12}$$

where we have made explicit the dependence of Σ on the quasiparticle energies E_i, which are unknown. By performing a Taylor expansion we may approximate $\Sigma(E_i)$ as

$$\Sigma(E_i) = \Sigma(\epsilon_i) + (E_i - \epsilon_i)\frac{\partial \Sigma(\epsilon_i)}{\partial E} + \dots \tag{B.13}$$

so we finally arrive at

$$\begin{aligned} E_i &= \epsilon_i + Z_i \langle \phi_i | [\hat{\Sigma}(\epsilon_i) - \hat{V}_{xc}] | \phi_i \rangle \\ Z_i &= \left[1 - \frac{\partial \Sigma(\epsilon_i)}{\partial E} \right]^{-1}, \end{aligned} \tag{B.14}$$

where Z_i is known as the renormalisation factor. From this last expression we can compute the quasiparticle eigenvalues using KS-DFT results once we calculate the self-energy Σ. The relation between G and Σ is provided by Hedin's set of integro-differential equations [35]. In the GW approximation we have that

$$\Sigma = iGW, \tag{B.15}$$

where G is the Green's function and W is a dynamically screened electrostatic interaction. Performing further approximations we may write Σ in terms of a non-interacting Green's function G_0 constructed from KS orbitals and eigenvalues, and a screened interaction calculated within the random-phase approximation [36–38]. We then have that

$$\begin{aligned} \Sigma(1,2) &= iG_0(1,2)W_0(1,2) \\ W_0(1,2) &= \int d3\varepsilon^{-1}(1,3)v(3,2) \\ \varepsilon(1,2) &= \delta(1,2) - \int d3v(1,3)\chi_0(3,2) \\ \chi_0(1,2) &= -iG_0(1,2)G_0(2,1), \end{aligned} \tag{B.16}$$

where we have employed a compact notation in which $1 \equiv (\mathbf{r}_1, \mathbf{t}_1)$, v is the bare Coulomb electrostatic interaction, χ_0 the response function and ε the dielectric matrix, which is typically approximated by a single-pole function within the *plasmon-pole* approximation [39]. With eqs. (B.14) and (B.16) we may correct the KS eigenvalues employing a *single-shot* (*i.e.*, non self-consistent) perturbative approach which has been successfully applied to many semiconducting sys-

tems yielding band gap values in much closer agreement with experiment than KS-DFT with standard exchange-correlation functionals. For a discussion on the adequacy of the approximations outlined here and case studies comparing obtained band gap values obtained within this approximation to experiments, see refs. [40, 41]. The results presented in chapters 4 and 5 as calculated employing the GW approximation follow this formalism and have been computed using the YAMBO software package [42]; details on the implementation can be found in refs. [43, 44].

B.1.3 Density functional tight binding

In chapters 2 and 3 we have presented electronic structure results computed using density functional tight binding (DFTB) for the larger studied structures. DFTB's combination of concepts derived from density functional theory (DFT) and tight-binding (TB) makes for a formalism which features increased computational efficiency when compared to DFT, and improved reliability and transferability when compared to TB, making it a useful alternative to DFT for calculations of large systems and in general situations where the computational cost of DFT becomes prohibitive such as molecular dynamics studies on long timescales and structure search studies [45–49]. In this section we will largely follow the simple and pedagogical derivation by Koskinen and Mäkinen [50], for a comprehensive review on the theory see refs. [51–55].

DFTB is not an *ab-initio* method as it is parametrised using DFT, although it is rooted in first principles deeper than any other TB flavours, and most of its parameters have a theoretically solid basis. Its formalism basically consists in turning DFT into a working tight-binding scheme where parametrisations are computed based on first-principles and stored in *Slater-Koster tables* [56] for later use, hence minimising the computational effort required on runtime at the cost of compromising transferability. As is the case with any TB formalism, the fundamental starting point of DFTB is *tightly bound* electrons and is thus ideally suited for covalent systems such as hydrocarbons [45, 57], although it has been found to perform surprisingly well in describing metallic systems [58–60].

Starting from the Kohn-Sham DFT expression for the total electronic energy in eq. (B.4) we may write the total energy of the system as

$$E[n] = T_{KS}[n] + E_{Hartree}[n] + \int d\mathbf{r} V_{ext}(\mathbf{r}) n(\mathbf{r}) + E_{xc}[n] + E_{II}, \tag{B.17}$$

where we have included the nuclear-nuclear repulsive energy E_{II}, which is constant for a given set of nuclear positions. We now start approximating by considering a system with a reference density $n_{ref}(\mathbf{r})$ composed of atomic-like densities such that it neighbours the true minimising density $n_{min}(\mathbf{r}) = n_{ref}(\mathbf{r}) + \delta n(\mathbf{r})$. Expanding $E[n_{min}]$ around n_{ref} up to second order fluctuations in δn we arrive at

$$\begin{aligned} E[n_{min}] \approx \sum_i \langle \phi_i | \hat{h}_0[n_{ref}] | \phi_i \rangle + \frac{1}{2} \int d\mathbf{r} d\mathbf{r}' \left(\frac{\delta^2 E_{xc}[n_{ref}]}{\delta n(\mathbf{r}) \delta n(\mathbf{r}')} + \frac{1}{|\mathbf{r} - \mathbf{r}'|} \right) \delta n(\mathbf{r}) \delta n(\mathbf{r}') \\ - \frac{1}{2} \int d\mathbf{r} d\mathbf{r}' \frac{n_{ref}(\mathbf{r}) n_{ref}(\mathbf{r}')}{|\mathbf{r} - \mathbf{r}'|} + E_{xc}[n_{ref}] - \int d\mathbf{r} V_{xc}[n_{ref}](\mathbf{r}) n_{ref}(\mathbf{r}) + E_{II} \end{aligned} \tag{B.18}$$

where the linear terms in δn vanish and the third term corrects for a double counting of the Hartree energy present in $\hat{h}_0$ [46]. Grouping the terms in the last equation we have that

$$E[n_{min}] \approx E_{BS}[n_{ref}] + E_{Coul}[n_{ref}, \delta n] + E_{rep}[n_{ref}] \tag{B.19}$$

where the first term is called the *band-structure* term in the literature, the second term contains electrostatic interactions and some exchange-correlation contributions, and the last term is called the *repulsive* term as it contains ion-ion interactions:

$$\begin{aligned} E_{BS}[n_{ref}] =& \sum_i \langle \psi_i | \overbrace{\hat{T}_{elec} + \hat{V}_{ext} + 2\hat{V}_{Hartree} + \hat{V}_{xc}}^{\hat{h}_0[n_{ref}]} | \psi_i \rangle \\ E_{Coul}[n_{ref}, \delta n] =& \frac{1}{2} \int d\mathbf{r} d\mathbf{r}' \left(\frac{\delta^2 E_{xc}[n_{ref}]}{\delta n(\mathbf{r}) \delta n(\mathbf{r}')} + \frac{1}{|\mathbf{r} - \mathbf{r}'|} \right) \delta n(\mathbf{r}) \delta n(\mathbf{r}') \\ E_{rep}[n_{ref}] =& -\frac{1}{2} \int d\mathbf{r} d\mathbf{r}' \frac{n_{ref}(\mathbf{r}) n_{ref}(\mathbf{r}')}{|\mathbf{r} - \mathbf{r}'|} + E_{xc}[n_{ref}] \\ & - \int d\mathbf{r} V_{xc}[n_{ref}](\mathbf{r}) n_{ref}(\mathbf{r}) + E_{II}. \end{aligned} \tag{B.20}$$

At this point we note that DFTB treats charge transfer between atoms perturbatively instead of neglecting it as per the usual TB approach. Charge transfer within DFTB is self-consistently described through E_{Coul}, as all other terms depend only on the reference density n_{ref}. This self-consistent charge (SCC) type of DFTB is usually called SCC-DFTB in the literature.

By assuming n_{ref} to be spherically symmetric around atoms we may divide the integrals in E_{rep} into sums over pairs of atoms, finally arriving at

$$E_{rep} = \sum_{I<J} V_{rep}^{IJ}(R_{IJ}), \tag{B.21}$$

where I, J run over atomic sites, and E_{rep} depends only on the distance between pairs of atoms R_{IJ}. Adopting manners from DFT, we lump together the complicated exchange-correlation physics under E_{rep} and fit this term to DFT calculations, making it DFTB's practical equivalent to the exchange-correlation energy in DFT. We note that E_{rep} contains on-site as well as pair-wise contributions, but these depend only on n_{ref} and shift the total energy by a constant.

Expanding density fluctuations as a sum of atomic contributions $\delta n = \sum_I \Delta q_I \delta n_I$, the charge fluctuation term can be cast in a simpler form

$$E_{Coul} \approx \frac{1}{2}\sum_{I,J} \gamma_{IJ}(R_{IJ})\Delta q_I \Delta q_J \tag{B.22}$$
$$\gamma_{IJ} = \begin{cases} U_I, & I = J \\ \frac{\text{erf}(C_{IJ}R_{IJ})}{R_{IJ}}, & I \neq J \end{cases}$$

where U_I is related to the chemical hardness of atom I, and C_{IJ} can be easily calculated from U_I and U_J [50]. Finally, we arrive at an expression for the total energy with a transparent TB form

$$E = \sum_i \langle \phi_i | \hat{h}_0 | \phi_i \rangle + \frac{1}{2}\sum_{I,J} \gamma_{IJ}(R_{IJ})\Delta q_I \Delta q_J + E_{rep}. \tag{B.23}$$

Expanding KS orbitals within an LCAO approach by employing a suitable set of localised atomic orbitals centered about nuclear positions $\mathbf{R_I}$

$$\phi_i(\mathbf{r}) = \sum_\alpha c_{\alpha i}\varphi_\alpha(\mathbf{r} - \mathbf{R}_I) \tag{B.24}$$

and expanding E_{BS}, we arrive at

$$E = \sum_i \sum_{\alpha\beta} c^*_{\alpha i} c_{\beta i} h_0^{\alpha\beta} + \frac{1}{2}\sum_{I,J} \gamma_{IJ}(R_{IJ})\Delta q_I \Delta q_J + \sum_{I<J} V_{rep}^{IJ}(R_{IJ}) \qquad \text{(B.25)}$$
$$h_0^{\alpha\beta} = \langle \varphi_\alpha | \hat{h}_0 | \varphi_\beta \rangle$$

Finally, by applying Mulliken charge analysis [61] for estimating charge fluctuations, expanding in terms of eq. (B.24) and applying the variational principle, we arrive at the Kohn-Sham equations-equivalent in DFTB:

$$\sum_\alpha c_{\alpha i} \left(h_{\alpha\beta} - \lambda_i S_{\alpha\beta}\right) = 0 \qquad \text{(B.26)}$$
$$h_{\alpha\beta} = h_0^{\alpha\beta} + \frac{1}{2} S_{\alpha\beta} \sum_\eta (\gamma_{I\eta} + \gamma_{J\eta})\Delta q_\eta; \qquad \alpha \in I, \beta \in J$$

where λ_i are undetermined Lagrange multipliers and $S_{\alpha\beta} = \langle \varphi_\alpha | \varphi_\beta \rangle$ is the overlap between orbitals α and β. As in KS-DFT, eqs. (B.26) must be solved self consistently: from a given initial guess for $\{q_I\}$ one obtains $h_{\alpha\beta}$, then $\{c_{\alpha i}\}$ and finally a new $\{q_I\}$, until self-consistency is reached. Typically DFTB requires considerably less iterations than DFT, albeit both approaches share similar convergence problems.

The reduction in computational effort in DFTB arises from the fact that all terms which depend only on the reference density n_{ref} are read from pre-calculated Slater-Koster (SK) tables, and only charge fluctuations are treated explicitly. The limited transferability of DFTB springs from its perturbative treatment of charge transfer between atoms, and thus tabulated matrix elements and repulsive potential must be calculated by employing *pseudoatoms* which mimic a similar chemical environment to that intended to study with DFTB.

In chapter 2 we compared the accuracy of DFTB with two different parameter sets against DFT for electronic transport calculations. In addition to publicly available SK tables [62], we have also benchmarked the performance of SK tables explicitly generated for nanoscale Cu structures following the procedure outlined in ref. [63]. We conclude that the error encountered with respect to DFT for both parameter sets is similar, although the latter parameter set was found to perform slightly better [see chapter 2]. DFTB calculations presented in

chapters 2 and 3 have been performed using the QUANTUMWISE [16] software package. For more details on the implementation see ref. [46].

B.2 Electronic transport methods: the non-equilibrium Green's function formalism

The Non-Equilibrium Green's Function (NEGF) and Landauer formalisms enable the quantum mechanical description of electronic transport through a finite piece of material (commonly referred to as the *central region*) which is electrically connected to semi-infinite electron reservoirs (*leads* or *electrodes*) are considered to be at equilibrium. For a comprehensive review of the theory see refs. [30, 64–66].

As per standard Green's function theory, we can describe the propagation of particles through an explicitly treated finite piece of material (central region) via the following two-time correlation functions:

$$\begin{aligned} G^n(\mathbf{k},\mathbf{k}';t,t') &= \langle a^\dagger_{\mathbf{k}'}(t')a_{\mathbf{k}}(t)\rangle \\ G^p(\mathbf{k},\mathbf{k}';t,t') &= \langle a_{\mathbf{k}}(t)a^\dagger_{\mathbf{k}'}(t')\rangle\,, \end{aligned} \tag{B.27}$$

which, in a similar fashion to eq. (B.10), describe the propagation of an electron ($\hat{G}^n$) or a hole ($\hat{G}^p$) from $|\mathbf{k},t\rangle$ to $|\mathbf{k}',t'\rangle$ through creation and annihilation operators $\hat{a}$ and $\hat{a}^\dagger$. $\hat{G}^n$ and $\hat{G}^p$ contain information on the occupied and unoccupied states in the central region, respectively, as modified by interactions with the electron reservoirs, which are assumed unchanged by interactions with the central region and kept at constant chemical potentials and temperatures. We define the spectral function of the system as

$$\hat{A} \equiv \hat{G}^n + \hat{G}^p = i[\hat{G}^R - \hat{G}^A] \tag{B.28}$$

which contains information on all electronic states within the central region and can be written in terms of the *retarded* and *advanced* functions $\hat{G}^{R,A}$, which constitute a description of the propagation in terms of *outgoing* and *incoming* waves, respectively. Akin to the treatment discussed in appendix B.1.2, the in-

teractions of the central region with the electron reservoirs (electrodes) are included in this description through energy dependent, non-Hermitian self-energy operators. These operators are responsible not only for modifying the eigenvalues and eigenstates of the isolated central region's Hamiltonian $\hat{H}_C$, but they also introduce an imaginary part to it characterised by the anti-hermitian part of the self-energy:

$$\hat{\Gamma} = i[\hat{\Sigma}^R - \hat{\Sigma}^A] \tag{B.29}$$

which ultimately describes the coupling with the contacts and the rate at which coherent trajectories terminate by either escaping into leads or scattering into a different state. Each electrode contributes to the self-energy and thus the quantities used when calculating electron dynamics should be the sum of all contributions. For a particular lead q:

$$\hat{\Sigma}_q^R = \hat{\tau}\hat{g}_q^R\hat{\tau}^\dagger = \left[\hat{\Sigma}_q^A\right]^\dagger \tag{B.30}$$

$$\hat{g}_q^R = [E_q\hat{I} - \hat{H}_q]^{-1}, \tag{B.31}$$

where $\hat{\tau}$ is a matrix which describes the coupling between states in the lead and states in the central region, $\hat{g}_q^R$ is the retarded Green's function of the electrode and $\hat{H}_q$ its Hamiltonian function. Self-energy operators describe not only the role of the leads; other interactions that introduce scattering into the system can be introduced in a similar way. The corresponding expressions will of course depend on the nature of the interaction.

This approach allows the quantum-mechanical description of steady-state non-equilibrium electronic transport through the central region as per its interactions with electron reservoirs or leads, which are kept at equilibrium at constant chemical potentials and temperatures. Within this formalism, we can write the current flowing between lead p and the central region as

$$I_p = \int i_p(E)dE \tag{B.32}$$

$$i_p(E) = \frac{e}{h}\,\mathrm{Tr}\,[\hat{\Sigma}_p^{in}\hat{G}^p - \hat{\Sigma}_p^{out}\hat{G}^n],$$

where we have introduced the $\hat{\Sigma}^{in}$ and $\hat{\Sigma}^{out}$ representations of the self-energy

$$\begin{aligned} \hat{\Sigma}_p^{in} &= f_p(E)\hat{\Gamma}_p(E) \\ \hat{\Sigma}_p^{out} &= (1 - f_p(E))\hat{\Gamma}_p(E) \\ \hat{\Gamma}_p &= \hat{\Sigma}_p^{in} + \hat{\Sigma}_p^{out}, \end{aligned} \tag{B.33}$$

where f_p is the Fermi-Dirac distribution describing occupations in lead p, and depends on its chemical potential and temperature (μ_p, T_p). Equation (B.32) allows for a rather intuitive interpretation of i_p in terms of both terms inside the trace: at a given energy, the current density is proportional to the inflow rate of electrons from lead p multiplied by the density of unoccupied states in the central region, minus the outflow rate to lead p multiplied by the density of occupied states in the central region. Calculating the expressions for the current flow between two leads p and q, and relating it to the Landauer formalism [64] we arrive at

$$\begin{aligned} I_{pq} &= \int i_{pq}(E)dE \\ i_{pq}(E) &= \frac{e}{h}\,\mathrm{Tr}\,[\hat{\Gamma}_p\hat{G}^R\hat{\Gamma}_q\hat{G}^A](f_p - f_q) = \frac{e}{h}T_{pq}(E)(f_p(E) - f_q(E)), \end{aligned} \tag{B.34}$$

where the *transmission function* T_{pq} contains information about the rate at which electrons transmit between electrodes p and q, and depends implicitly on the occupations in the electrodes. Throughout this thesis we have employed this formalism describing electronic transport between two leads within a coherent elastic framework, as self-energy operators describing inelastic or phase-breaking processes such as electron-phonon interactions or Büttiker probes have not been included in our treatment [67]. For a discussion on the applicability of these approximation to transport in semiconducting nanowires, see ref. [68]. In chapters 2 and 3 we have additionally employed the *linear response* approximation for the conductance of metallic nanostructures

$$G = \frac{e^2}{h}T_{pq}(E_F), \tag{B.35}$$

which is exact in the limit of zero temperature or for systems whose transmis-

sion function is constant within the applied bias window, and E_F is the Fermi level of the central region at equilibrium (*i.e.*, zero applied bias).

All electronic transport results presented throughout this work have been computed within this formalism for the case of two electrodes (usually labelled *Left* and *Right*, or L and R) using the QUANTUMWISE [16] software package and employing DFT or DFTB methods for treating the electronic structure, as specified. For more details on the implementation see ref. [69].

B.2.1 Transmission pathways

A local current formalism which allows calculating local transmission coefficients between pairs of atoms within the theoretical framework outlined above is described in ref. [70]. In chapters 2 and 3 we have employed this method in order to explore the cross-sectional distribution of the current density in Cu nanostructures.

The time-independent Hamiltonian function of a *central region* can be written in a basis set of atom-centered orbitals, such as LCAO-DFT or DFTB, as

$$H = \sum_{\alpha} \epsilon_{\alpha} c_{\alpha}^{*} c_{\alpha} + \sum_{\alpha \neq \beta} V_{\alpha\beta} c_{\alpha}^{*} c_{\beta}, \tag{B.36}$$

where α and β run over said atom-centered orbitals, and ϵ_{α} is the energy of an electron in orbital α. The current flow between atoms $I \neq J$ located within the central region can be written as

$$\begin{aligned} I_{IJ} &= \frac{e}{h} \int dE K_{IJ}(E) \\ K_{IJ}(E) &= i \sum_{\alpha \in I} \sum_{\beta \in J} \left(V_{\alpha\beta} G^{n}_{\beta\alpha} - V_{\beta\alpha} G^{p}_{\alpha\beta} \right), \end{aligned} \tag{B.37}$$

where α and β run over orbitals centered about I and J, respectively. Taking into account the following relations and the definition of the spectral density of the leads:

$$\begin{aligned} G^R &= [EI - H_C - \Sigma^R]^{-1} \\ G^A &= [G^R]^\dagger \\ G^n &= G^R \Sigma^{in} G^A \\ \Sigma^{in} &= f_L \Gamma^L + f_R \Gamma^R \\ \Gamma^p_{\alpha\beta} &= 2\pi \sum_\gamma V_{\alpha\gamma} V_{\gamma\beta} \delta(E - \epsilon_\gamma), \end{aligned} \tag{B.38}$$

we arrive at

$$\begin{aligned} K_{IJ}(E) = i \sum_{\alpha\in I} \sum_{\beta\in J} \sum_{\gamma,\delta} \Big[& f_L \left(V_{\alpha\beta} G^R_{\beta\gamma} \Gamma^L_{\gamma\delta} G^A_{\delta\alpha} - V_{\beta\alpha} G^R_{\alpha\delta} \Gamma^L_{\delta\gamma} G^A_{\gamma\beta} \right) \\ & - f_R \left(V_{\beta\alpha} G^R_{\alpha\delta} \Gamma^R_{\delta\gamma} G^A_{\gamma\beta} - V_{\alpha\beta} G^R_{\beta\gamma} \Gamma^R_{\gamma\delta} G^A_{\delta\alpha} \right) \Big], \end{aligned} \tag{B.39}$$

which is the expression employed in the implementation used throughout this work [16] and gives the local coefficients transmission coefficient between pairs of atoms, and its magnitude and sign correspond to the size and colour of the 'dots' in figs. 2.7 and 3.5.

References

[1] Robert G. Parr and Weitao Yang. *Density functional theory of atoms and molecules*. Oxford University Press, Oxford OX2 6DP, United Kingdom, 1989.

[2] Reiner M. Dreizler and Eberhard K.U. Gross. *Density functional theory: An approach to the quantum many-body problem*. Springer, Berlin, Germany, 1990.

[3] Richard M. Martin. *Electronic structure*. Cambridge University Press, Cambridge CB2 8BS, United Kingdom, 2008.

[4] R. O. Jones. Density functional theory: Its origins, rise to prominence, and future. *Rev. Mod. Phys.*, 87(3):897–923, 2015.

[5] P. Hohenberg and W. Kohn. Inhomogeneous electron gas. *Phys. Rev.*, 136(3B):B864–B871, 1964.

[6] M. Born and R. Oppenheimer. Zur quantentheorie der molekeln. *Annalen der Physik*, 389(20):457–484, 1927.

[7] Erich Runge and E. K. U. Gross. Density-functional theory for time-dependent systems. *Phys. Rev. Lett.*, 52(12):997–1000, 1984.

[8] W. Kohn and L. J. Sham. Self-consistent equations including exchange and correlation effects. *Phys. Rev.*, 140:A1133–A1138, 1965.

[9] John P. Perdew. Jacob's ladder of density functional approximations for the exchange-correlation energy. In *AIP Conference Proceedings*, volume 577. AIP Publishing, 2001.

[10] J.P. Perdew, K. Burke, and M. Ernzerhof. Generalized gradient approximation made simple. *Phys. Rev. Lett.*, 77:3865–3868, 1996.

[11] Fabien Tran and Peter Blaha. Accurate band gaps of semiconductors and insulators with a semilocal exchange-correlation potential. *Phys. Rev. Lett.*, 102:226401, 2009.

[12] John P. Perdew and Mel Levy. Physical content of the exact Kohn-Sham orbital energies: Band gaps and derivative discontinuities. *Phys. Rev. Lett.*, 51:1884–1887, 1983.

[13] L. J. Sham and M. Schlüter. Density-functional theory of the energy gap. *Phys. Rev. Lett.*, 51(20):1888–1891, 1983.

[14] L. J. Sham and M. Schlüter. Density-functional theory of the band gap. *Phys. Rev. B*, 32(6):3883–3889, 1985.

[15] OPENMX software package. *www.openmx-square.org (accessed August 2016)*.

[16] Atomistix ToolKit version 2015-1 QuantumWise A/S. *www.quantumwise.com (accessed August 2016)*.

[17] I. Morrison, D.M. Bylander, and L. Kleinman. Non-local Hermitian norm-conserving Vanderbilt pseudopotenial. *Phys. Rev. B*, 47:6728–6731, 1993.

[18] T. Ozaki and H. Kino. Numerical atomic basis orbitals from H to Kr. *Phys. Rev. B*, 69:195113, 2004.

[19] QUANTUMESPRESSO. *http://www.quantum-espresso.org/ (Accessed December 2016)*.

[20] N. Troullier and José Luís Martins. Efficient pseudopotentials for plane-wave calculations. *Phys. Rev. B*, 43:1993–2006, 1991.

[21] José M Soler, Emilio Artacho, Julian D Gale, Alberto Garcia, Javier Junquera, Pablo Ordejon, and Daniel Sanchez-Portal. The SIESTA method for ab initio order-N materials simulation. *J. Phys.: Condens. Matter*, 14(11):2745, 2002.

[22] T. Ozaki. Variationally optimized atomic orbitals for large-scale electronic structures. *Phys. Rev. B*, 67:155108, 2003.

[23] Paolo Giannozzi, Stefano Baroni, Nicola Bonini, Matteo Calandra, Roberto Car, Carlo Cavazzoni, Davide Ceresoli, Guido L Chiarotti, Matteo Cococcioni, Ismaila Dabo, Andrea Dal Corso, Stefano de Gironcoli, Stefano Fabris, Guido Fratesi, Ralph Gebauer, Uwe Gerstmann, Christos Gougous-

sis, Anton Kokalj, Michele Lazzeri, Layla Martin-Samos, Nicola Marzari, Francesco Mauri, Riccardo Mazzarello, Stefano Paolini, Alfredo Pasquarello, Lorenzo Paulatto, Carlo Sbraccia, Sandro Scandolo, Gabriele Sclauzero, Ari P Seitsonen, Alexander Smogunov, Paolo Umari, and Renata M Wentzcovitch. QUANTUMESPRESSO: a modular and open-source software project for quantum simulations of materials. *J. Phys.: Condens. Matter*, 21(39):395502, 2009.

[24] Andrea Dal Corso. Pseudopotentials periodic table: From H to Pu. *Comput. Mater. Sci.*, 95:337–350, 2014.

[25] Kurt Lejaeghere, Gustav Bihlmayer, Torbjörn Björkman, Peter Blaha, Stefan Blügel, Volker Blum, Damien Caliste, Ivano E. Castelli, Stewart J. Clark, Andrea Dal Corso, Stefano de Gironcoli, Thierry Deutsch, John Kay Dewhurst, Igor Di Marco, Claudia Draxl, Marcin Dułak, Olle Eriksson, José A. Flores-Livas, Kevin F. Garrity, Luigi Genovese, Paolo Giannozzi, Matteo Giantomassi, Stefan Goedecker, Xavier Gonze, Oscar Grånäs, E. K. U. Gross, Andris Gulans, François Gygi, D. R. Hamann, Phil J. Hasnip, N. A. W. Holzwarth, Diana Iuşan, Dominik B. Jochym, François Jollet, Daniel Jones, Georg Kresse, Klaus Koepernik, Emine Küçükbenli, Yaroslav O. Kvashnin, Inka L. M. Locht, Sven Lubeck, Martijn Marsman, Nicola Marzari, Ulrike Nitzsche, Lars Nordström, Taisuke Ozaki, Lorenzo Paulatto, Chris J. Pickard, Ward Poelmans, Matt I. J. Probert, Keith Refson, Manuel Richter, Gian-Marco Rignanese, Santanu Saha, Matthias Scheffler, Martin Schlipf, Karlheinz Schwarz, Sangeeta Sharma, Francesca Tavazza, Patrik Thunström, Alexandre Tkatchenko, Marc Torrent, David Vanderbilt, Michiel J. van Setten, Veronique Van Speybroeck, John M. Wills, Jonathan R. Yates, Guo-Xu Zhang, and Stefaan Cottenier. Reproducibility in density functional theory calculations of solids. *Science*, 351(6280), 2016.

[26] John P. Perdew, Robert G. Parr, Mel Levy, and Jose L. Balduz. Density-functional theory for fractional particle number: Derivative discontinuities of the energy. *Phys. Rev. Lett.*, 49:1691–1694, 1982.

[27] John P. Perdew. Density functional theory and the band gap problem. *Int. J. Quantum Chem.*, 28(S19):497–523, 1985.

[28] F. Aryasetiawan and O. Gunnarsson. The GW method. *Rep. Prog. Phys.*, 61(3):237, 1998.

[29] Giovanni Onida, Lucia Reining, and Angel Rubio. Electronic excitations: density-functional versus many-body Green's-function approaches. *Rev. Mod. Phys.*, 74:601–659, 2002.

[30] Henrik Bruus and Karsten Flensberg. *Many-body quantum theory in condensed matter physics: An introduction*. Oxford University Press, Oxford OX2 6DP, United Kingdom, 2004.

[31] L.D. Landau. The theory of a Fermi liquid. *Sov. Phys. JETP*, 3:920, 1956.

[32] L.D. Landau. Oscillations in a Fermi liquid. *Sov. Phys. JETP*, 5:101, 1956.

[33] L.D. Landau. On the theory of the Fermi liquid. *Sov. Phys. JETP*, 8:70, 1959.

[34] Lars Hedin and Stig Lundqvist. Effects of electron-electron and electron-phonon interactions on the one-electron states of solids. In *Solid State Physics*, pages 1–181. Elsevier BV, New York, 1970.

[35] Lars Hedin. New method for calculating the one-particle Green's function with application to the electron-gas problem. *Phys. Rev.*, 139:A796–A823, 1965.

[36] David Bohm and David Pines. A collective description of electron interactions. I. magnetic interactions. *Phys. Rev.*, 82:625–634, 1951.

[37] David Pines and David Bohm. A collective description of electron interactions: II. collective vs individual particle aspects of the interactions. *Phys. Rev.*, 85:338–353, 1952.

[38] David Bohm and David Pines. A collective description of electron interactions: III. coulomb interactions in a degenerate electron gas. *Phys. Rev.*, 92:609–625, 1953.

[39] Paul Larson, Marc Dvorak, and Zhigang Wu. Role of the plasmon-pole model in the GW approximation. *Phys. Rev. B*, 88:125205, 2013.

[40] M. van Schilfgaarde, Takao Kotani, and S. Faleev. Quasiparticle self-consistent GW theory. *Phys. Rev. Lett.*, 96:226402, 2006.

[41] Mark van Schilfgaarde, Takao Kotani, and Sergey V. Faleev. Adequacy of approximations in GW theory. *Phys. Rev. B*, 74:245125, 2006.

[42] YAMBO. *http://www.yambo-code.org/ (accessed August 2016)*.

[43] Andrea Marini, Conor Hogan, Myrta Grüning, and Daniele Varsano. YAMBO: An ab initio tool for excited state calculations. *Comput. Phys. Commun.*, 180(8):1392 – 1403, 2009.

[44] Carlo A. Rozzi, Daniele Varsano, Andrea Marini, Eberhard K. U. Gross, and Angel Rubio. Exact coulomb cutoff technique for supercell calculations. *Phys. Rev. B*, 73:205119, 2006.

[45] D. Porezag, Th. Frauenheim, Th. Köhler, G. Seifert, and R. Kaschner. Construction of tight-binding-like potentials on the basis of density-functional theory: Application to carbon. *Phys. Rev. B*, 51:12947–12957, 1995.

[46] M. Elstner, D. Porezag, G. Jungnickel, J. Elsner, M. Haugk, Th. Frauenheim, S. Suhai, and G. Seifert. Self-consistent-charge density-functional tight-binding method for simulations of complex materials properties. *Phys. Rev. B*, 58(11):7260–7268, 1998.

[47] Th. Frauenheim, G. Seifert, M. Elsterner, Z. Hajnal, G. Jungnickel, D. Porezag, S. Suhai, and R. Scholz. A self-consistent charge density-functional based tight-binding method for predictive materials simulations in physics, chemistry and biology. *Phys. Status Solidi B*, 217(1):41–62, 2000.

[48] Koblar A. Jackson, Mihai Horoi, Indira Chaudhuri, Thomas Frauenheim, and Alexandre A. Shvartsburg. Unraveling the shape transformation in silicon clusters. *Phys. Rev. Lett.*, 93:013401, 2004.

[49] Pekka Koskinen, Hannu Häkkinen, Bernd Huber, Bernd von Issendorff, and Michael Moseler. Liquid-liquid phase coexistence in gold clusters: 2D or not 2D?. *Phys. Rev. Lett.*, 98:015701, 2007.

[50] Pekka Koskinen and Ville Mäkinen. Density-functional tight-binding for beginners. *Comput. Mater. Sci.*, 47(1):237–253, 2009.

[51] Thomas Frauenheim, Gotthard Seifert, Marcus Elstner, Thomas Niehaus, Christof Köhler, Marc Amkreutz, Michael Sternberg, Zoltán Hajnal, Aldo Di Carlo, and Sándor Suhai. Atomistic simulations of complex materials: ground-state and excited-state properties. *J. Phys.: Condens. Matter*, 14(11):3015, 2002.

[52] G. Seifert. Tight-binding density functional theory: an approximate Kohn-Sham DFT scheme. *J. Phys. Chem. A*, 111(26):5609–5613, 2007.

[53] Nikolaj Otte, Mirjam Scholten, and Walter Thiel. Looking at self-consistent-charge density functional tight binding from a semiempirical perspective. *J. Phys. Chem. A*, 111(26):5751–5755, 2007.

[54] M. Elstner. SCC-DFTB: What is the proper degree of self-consistency?. *The Journal of Physical Chemistry A*, 111(26):5614–5621, 2007.

[55] Gotthard Seifert and Jan-Ole Joswig. Density-functional tight binding—an approximate density-functional theory method. *Wiley Interdiscip. Rev.: Comput. Mol. Sci.*, 2(3):456–465, 2012.

[56] J. C. Slater and G. F. Koster. Simplified LCAO method for the periodic potential problem. *Phys. Rev.*, 94:1498–1524, 1954.

[57] Sami Malola, Hannu Häkkinen, and Pekka Koskinen. Raman spectra of single-walled carbon nanotubes with vacancies. *Phys. Rev. B*, 77:155412, 2008.

[58] Christof Köhler, Gotthard Seifert, and Thomas Frauenheim. Density functional based calculations for $\mathrm{Fe_n}$ ($n \leqslant 32$). *Chem. Phys.*, 309(1):23–31, 2005.

[59] P Koskinen, H Häkkinen, G Seifert, S Sanna, Th Frauenheim, and M Moseler. Density-functional based tight-binding study of small gold clusters. *New J. Phys.*, 8:9–9, 2006.

[60] Alfonso Sanchez-Soares, Sarah L. T. Jones, John J. Plombon, Ananth P. Kaushik, Roger E. Nagle, James S. Clarke, and James C. Greer. Effect of strain, thickness, and local surface environment on electron transport properties of oxygen-terminated copper thin films. *Phys. Rev. B*, 94:155404, 2016.

[61] R. S. Mulliken. Electronic population analysis on LCAO–MO molecular wave functions. *J. Chem. Phys.*, 23(10):1833–1840, 1955.

[62] dftb.org. *http://www.dftb.org (accessed August 2016)*.

[63] Mohammad Wahiduzzaman, Augusto F. Oliveira, Pier Philipsen, Lyuben Zhechkov, Erik van Lenthe, Henryk A. Witek, and Thomas Heine. DFTB parameters for the periodic table: Part 1, electronic structure. *J. Chem. Theory Comput.*, 9(9):4006–4017, 2013.

[64] R. Landauer. Spatial variation of currents and fields due to localized scatterers in metallic conduction. *IBM J. Res. Dev.*, 1(3):223–231, 1957.

[65] Supriyo Datta. *Electronic transport in mesoscopic systems*. Cambridge University Press, Cambridge CB2 8BS, United Kingdom, 1995.

[66] Supriyo Datta. Nanoscale device modeling: the Green's function method. *Superlattices Microstruct.*, 28(4):253 – 278, 2000.

[67] M. Büttiker. Four-terminal phase-coherent conductance. *Phys. Rev. Lett.*, 57:1761–1764, 1986.

[68] J. Appenzeller, J. Knoch, M. T. Bjork, H. Riel, H. Schmid, and W. Riess. Toward nanowire electronics. *IEEE Trans. Electron Devices*, 55(11):2827–2845, 2008.

[69] Mads Brandbyge, José-Luis Mozos, Pablo Ordejón, Jeremy Taylor, and Kurt Stokbro. Density-functional method for nonequilibrium electron transport. *Phys. Rev. B*, 65:165401, 2002.

[70] G.C. Solomon, C. Herrmann, T. Hansen, V. Mujica, and M.A. Ratner. Exploring local currents in molecular junctions. *Nat. Chem.*, 2:223, 2010.

Appendix C

Hollow optimization procedure

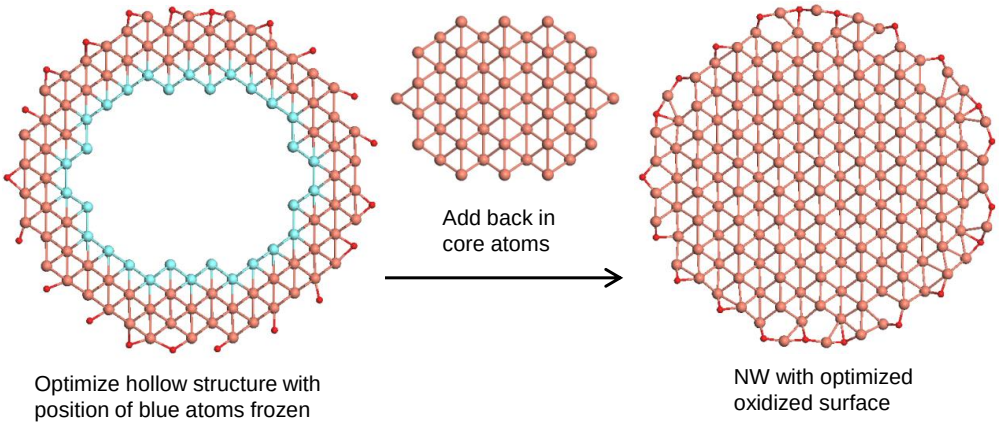

Figure C.1: Hollow optimization scheme for the [110]-O NW. The center of the NW (core) is removed and the blue colored atoms are frozen to their bulk position. The geometry of the surface is optimized and the core is added back in to obtain a surface-optimized structure which may be used in subsequent calculations to compute properties such as electron transmission.

The 3 nm [111] CuNW structure has a larger unit cell and therefore many more atoms than equivalent [100] and [110] oriented NWs. The structure is too large to be optimized using *ab initio* density functional theory (DFT) on a reasonable time scale and in any case, such a calculation is prohibited by high memory requirements. The 3 nm oxidized [100] and [110] NW structures have been fully optimized using DFT and the atoms in the core of these NWs have been observed to move only slightly compared to bulk copper positions (shown in Fig. C.2 (c) for the [110] NW). Therefore, we propose to optimize the surface of the oxidized [111] NW structure *without* the core region. The hollow optimization procedure is illustrated for the oxidized [110] NW in Fig.

C.1 and consists of the following steps:

1. Atoms five or more atomic layers away from the NW surface are removed to create the hollow structure
2. The coordinates of the innermost atoms of the hollow structure, colored blue in Fig. C.1, are kept fixed while the rest of the atomic positions are optimized until forces acting on them are below a specified threshold
3. The core region is added back in to obtain a NW structure with an optimized oxidized surface which can be used to calculate electronic properties, including electron transmission

Before applying the hollow optimization procedure to the [111] NW and obtaining the results reported in chapter 3, we assessed the reliability of the approach for the [110] oriented NW for which comparison can be made to a fully optimized structure. Fig. C.2 (c) superimposes the hollow optimized structure on the fully optimized structure and it can be clearly seen that at the NW core the structures are almost identical. The surfaces of these NWs are also remarkable similar, with a small deviation in geometry seen only at the bottom of the image. Therefore, the hollow optimization procedure provides an optimized geometry in reasonable agreement with the fully optimized NW.

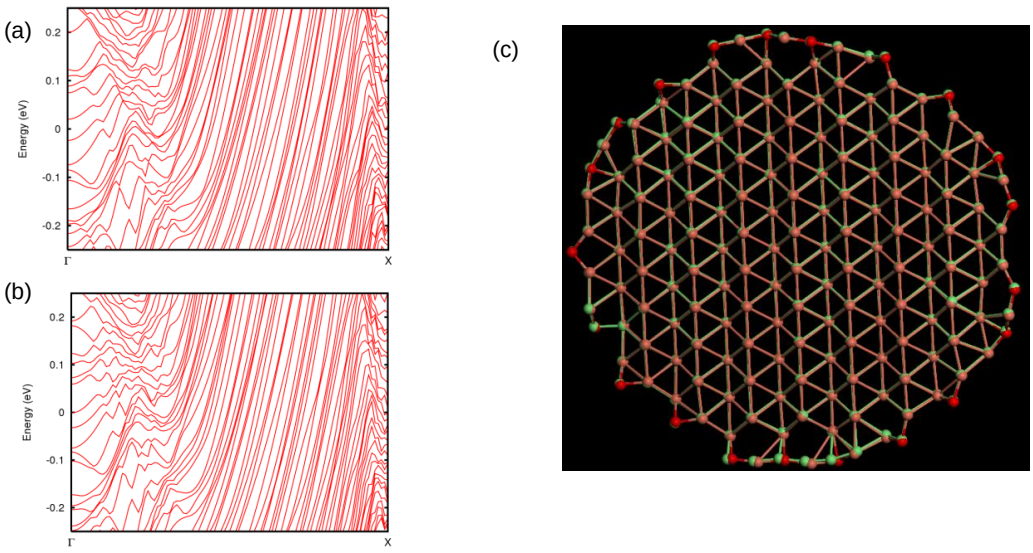

Figure C.2: (a) and (b) show the similarity in the band structures for the hollow optimized and fully optimized oxidized [110] NWs, respectively. In (c) the hollow optimized structure (pink and red atoms) is superimposed on the fully optimized structure (green atoms). There is a remarkable similarity in the surfaces of the NWs.

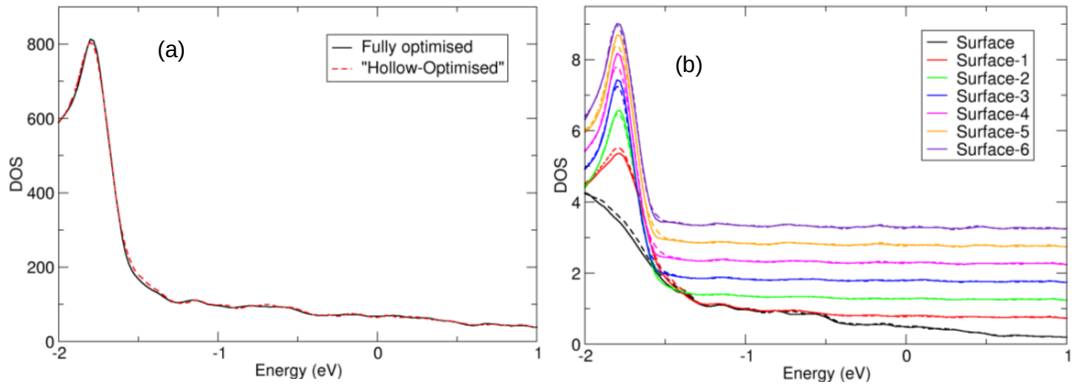

Figure C.3: The total DOS for the fully optimized and hollow optimized [110] oxidized NW are shown in (a). The changes in LDOS from the surface (Surface) to the center (Surface-6) of the fully optimized (full line) and hollow optimized (dashed line) are given in (b). The DOS and LDOs are comparable for our purposes between the two structures.

While it has been established that the hollow optimized NW compares well with the fully optimized NW in terms of geometry, we are ultimately interested in the electronic structure. The band structures around the Fermi energy of the hollow optimized and fully optimized NWs are shown in Fig. C.2 (a) and (b), respectively. As might be anticipated from the similarity of the geometries, the band structures of these NWs are also very similar. The total density of states (DOS) is shown in Fig. C.3 (a) and once again the results are very similar for the hollow optimized and fully optimized NWs. We additionally calculate the LDOS for different layers of atoms in each NW, shown in Fig. C.3 (b), starting at the surface ("Surface" in Fig. C.3 (b)) and moving away from the surface layer by layer until the NW center ("Surface-6" in C.3 (b)) is reached. Very good agreement is found between the fully optimized and hollow optimized NW layer DOS and LDOS.

Finally, we calculate the electron transmission for the hollow optimized and fully optimized NW geometries. As shown in Fig. C.4 (note the scale), we find good agreement in the electron transmission results, with deviation in the electon transmission in the range of interest ($\pm$ 50 meV around the Fermi energy) below 10% between the hollow optimized and fully optimized NW results. Such a change in electron transmission is comparable to the expected deviation from using density functional tight binding as compared to DFT to calculate electron transmission, and does not affect the overall conclusions of this work.

In summary, the hollow optimization procedure enables the surface of the NW to be optimized in the absence of a core region, which is defined such that the

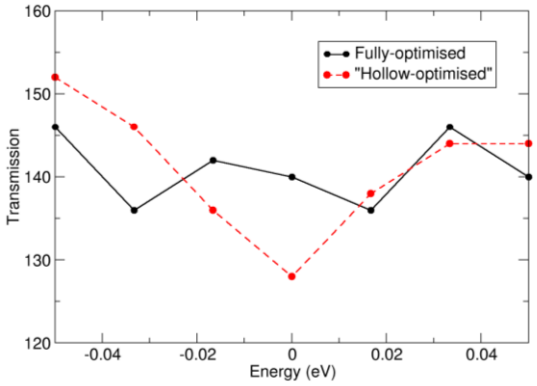

Figure C.4: The transmission coefficients computed with DFTB for the hollow optimized and fully optimized oxidized [110] NWs close to the Fermi energy (0 eV) deviate by less than typical differences between DFT and DFTB values.

atomic positions of the core atoms would only move very slightly from the bulk geometry if optimized. We apply this scheme to the [110] oxidized NW and compare the resulting structure to an equivalent fully optimized structure, taking consideration of geometry, band structure, density of states and electron transmission. Good agreement is found across these measures and we determine the deviation in the electron transmission to be under 10%. Thus, it is reasonable to optimize the 3 nm surface oxidized [111] NW geometry using this approach.